Nanolithographic Fabrication and Heterogeneous Reaction Studies of Two-Dimensional Platinum Model Catalyst Systems

by

Anthony Marshall Contreras

B.S. (California State University, Sacramento)

A dissertation submitted in partial satisfaction of the

requirements for the degree of

Doctor of Philosophy

in

Chemistry

in the

GRADUATE DIVISION

of the

UNIVERSITY OF CALIFORNIA, BERKELEY

Committee in charge:

Professor Gabor A. Somorjai (Chair)
Professor A. Paul Alivisatos
Professor David T. Attwood

Spring 2006

This dissertation of Anthony Marshall Contreras is approved:

_____

Chair Date

_____

Date

_____

Date

University of California, Berkeley

Spring 2006

Nanolithographic Fabrication and Heterogeneous Reaction Studies of Two-Dimensional Platinum Model Catalyst Systems

by

Anthony Marshall Contreras

Abstract

Nanolithographic Fabrication and Heterogeneous Reaction Studies of Two-Dimensional Platinum Model Catalyst Systems

by

Anthony Marshall Contreras

Doctor of Philosophy in Chemistry

University of California, Berkeley

Professor Gabor A. Somorjai (Chair)

In order to better understand the fundamental components that govern catalytic activity, two-dimensional model platinum nanocatalyst arrays have been designed and fabricated. These catalysts arrays are meant to model the interplay of the metal and support important to industrial heterogeneous catalytic reactions. Photolithography and sub-lithographic techniques such as electron beam lithography, size reduction lithography and nanoimprint lithography have been employed to create these platinum nanoarrays. Both in-situ and ex-situ surface science techniques and catalytic reaction measurements were used to correlate the structural parameters of the system to catalytic activity.

Electron beam lithography (EBL) has been used to fabricate platinum nanoparticle arrays in the 20-nm size range on oxide thin films of silica and alumina deposited onto silicon wafers. A combination of characterization techniques (SEM, AFM, XPS, AES) has been used to determine size, spatial arrangement and cleanliness of these fabricated catalysts. Ethylene hydrogenation reaction studies have been carried out

over these platinum nanoarrays and have revealed major differences in turnover rates and activation energies of the different nanostructures when clean and when poisoned with carbon monoxide. The oxide-metal interfaces are implicated as important reaction sites that remain active when the metal sites are poisoned by adsorbed carbon monoxide.

Size-reduction lithography (SRL) and nanoimprint lithography (NIL) has been utilized to produce platinum nanowires in the 20 – 60-nm size range on oxide films (SiO_2 and Al_2O_3) deposited onto silicon wafers. A combination of characterization techniques (SEM, AFM, XPS, AES) has been used to determine size, spatial arrangement and cleanliness of these fabricated catalysts. Ethylene hydrogenation reaction studies have been carried out over these fabricated catalysts as a probe reaction and have shown to have comparable turnover rates and activation energies to other platinum catalysts.

Deep-ultraviolet lithography has been coupled with size-reduction and nanoimprint lithography to create high-density arrays of platinum nanowires with dimensions 20 nm □ 5 nm □ 12 □m (width □ height □ length) on planar oxide thin films of silica, alumina, zirconia, and ceria. These nanowire arrays have been used as two-dimensional platinum model catalysts to study the effects of support on catalytic activity during the catalytic oxidation of carbon monoxide. A strong support dependence is seen for both reaction turnover frequency and the measured activation energy. The thermal stability of these nanowire arrays has been studied by annealing at 773 K and 973 K in a flow of helium. Upon annealing, substantial silicon migration is seen through the oxide support and a marked decrease in surface platinum is measured.

Using a variation of size-reduction lithography on an EBL-patterned silicon nitride membrane, we have reduced the size of 56-nm features in a silicon nitride

membrane, call a stencil, down to 36 nm. Sub-50 nm, uniformly-sized nanoparticles are fabricated by electron beam deposition of Pt through the stencil mask. The particle pattern replicates that of the stencil. Repositioning of the stencil mask in between two consecutive Pt deposition cycles led to a doubling of the original pattern density. A self-assembled monolayer (SAM) of tridecafluoro-1,1,2,2-tetrahydrooctyl-1-trichlorosilane was used to prevent Pt clogging of the nano size holes during deposition, as well as to protect the stencil during the post-deposition Pt removal. X-ray photoelectron spectroscopy shows that the SAM protects the stencil efficiently during this post-deposition removal of Pt.

_____

Professor Gabor A. Somorjai
Dissertation Committee Chair

Table of Contents

List of Figures and Tables

Chapter 2

Acknowledgements

I would like to first thank and acknowledge Professor Gabor A. Somorjai for accepting me into his research group and guiding me through my graduate school experience. His passion for learning new chemistry and pushing the limits of all aspects of the physical sciences to learn new chemical concepts has provided me with the opportunity to learn and has pushed me to lengths I never would have attained without him. From him, I have learned to think scientifically and how to approach scientific problems efficiently and without losing sight of the big picture. I am eternally grateful for all of his guidance and wish him the best in the future.

I would also like to thank several other professors from my qualification exam committee. Professors Paul Alivisatos, Marcin Majda, Herbert Strauss, David Attwood and Joseph Cerny have all taken the time to meet with me one-on-one to guide my growth as a scientist, and I am grateful for their time and the knowledge they have bestowed upon me. As well, Professor Luciano Moretto and Dr. Alexander Liddle have met with me in the past, and I would like to thank them for taking the time to teach me new concepts and for the general scientific discussions we have had.

I want to say thank you to my wife Angela for being patient with me during the long hours at graduate school and for virtually raising our three children on her own during this time. To my Adriana, Veronica and Vicente, I want to thank you for always being there to make me smile when I need it and for reminding me that life isn't all about work. Aurora and Manuel DeLaTorre deserve a special thanks for allowing me to even attend college. Without their help in raising my children while my wife and I worked and went to school, I would have never achieved what I have. I will never forget this and

hope to be able to repay this generosity in some form or another. To my parents, grandparents, and the rest of my family, I want to say thank you for always supporting me in my endeavors regardless of your personal thoughts about my choices.

I want to acknowledge all of the graduate students and postdoctoral fellow with whom I have worked. In particular, I want to thank Jeff Grunes and Ji Zhu who worked on my project with me. They both have given me huge amounts of help and support over the past four years. Despite his poor choice of football team and complete lack of talent on the foosball table, Jeff has become good friend and has always been there to offer advice and help me work through problems in any facet of my life, and I will always appreciate this. I have also worked with Dr. Xiaoming Yan, who I want to thank for all of his help in my project. His ability to teach and talk through problems has taught me a lot about science and has influenced my way of thinking greatly. I have just begun to work with Dr. Jeong Park and Russ Renzas, and I am already certain that their experience and expertise will continue to take this project well into the future.

Max Montano and Sasha Kweskin joined the Somorjai group with me and worked with me through all of the classes, teaching and outside things we had to deal with in graduate school. I want to thank them for keeping me sane and for becoming true friends during our time here at Berkeley. To Max, I want to say thanks for heading out to the surf every week with me. It's not easy to get into the ocean at 5:30AM, but when someone else does it with you, it's a little easier. In addition, I want to thank the rest of the Somorjai group for all of the help throughout my four years at Berkeley, and I wish you all the best in the future. I want to thank the Department of Energy, Office of Basic Energy Sciences for funding the research described in this dissertation.

Chapter 1

Introduction

Heterogeneous catalysis is an established field of extreme importance to industry as well as to the environment. In 1993, $8.7 billion worth of catalysts were sold worldwide, and currently well over $3 billion worth of catalysts are sold annually in the United States alone. While these are extremely high figures, it must be understood that for each dollar being spent on catalysts in industry, approximately $600 worth of products can be fabricated. In fact, about 90% of all the chemical manufacturing processes in the United States use catalysis in, at least, one step of their fabrication process[1]. Catalysts reduce the energy barrier to reaction and allow acceleration of a chemical change. Heterogeneous catalysts make use of a solid surface to catalyze the chemical change needed and are used in many different industries such as the petroleum, polymer, petrochemical, pharmaceutical industries, and for the three-way catalyst in automobiles.

Although in heavy demand and of extreme importance, many aspects of heterogeneous catalyst systems still remain unstudied. Surface scientists have been able

to uncover many of the key aspects to catalysis by use of metal single crystals as model catalyst systems. Metal single crystals are now very well understood two-dimensional systems and demonstrate many qualities that allow their use as model systems. These single-crystalline metals are extremely flat on the atomic scale and can have a single crystal face exposed over the entire surface. In addition, these crystals are conductive and have a metal surface area of approximately 1 cm^2, which allows for use of both photon-based and electron-based surface science techniques as well as allowing the study of catalytic reactions with small reaction turnover ($< 10^{-2}$ molecules/site/s). These well-defined crystals allow for correlation of surface structure with molecular adsorption and catalytic turnover. By use of surface techniques such as temperature programmed desorption (TPD), low-energy electron diffraction (LEED), x-ray photoelectron spectroscopy (XPS), electron energy loss spectroscopy (EELS) and sum-frequency generation (SFG), key ingredients to catalysis such as the nature of the adsorbate-metal bond and the fundamental steps in catalytic reaction mechanisms have been uncovered[2,3]. Of great importance to these studies is the fact that a reproducibly clean surface can be produced and verified by use of ultra-high vacuum, ion sputtering and Auger electron spectroscopy. Thus, the nature of the bonding being studied is assured to be from the metal and the introduced adsorbate and not from impurities that surface segregate from the bulk or are present from atmosphere.

The use of single crystals as model catalytic systems has shed light on many surface phenomena, which, in turn, has helped with the choice of metallic clusters for use in industrial catalysis. Industrial catalysts, however, do not just consist of metal, but are made up of metal particles in the 1 – 100 nm size regime dispersed in a high surface area

support. They are produced by synthesizing the metal particles and support separately and then dispersing the metal clusters onto the support by techniques such as wet-impregnation, co-precipitation, or ion-exchange[4]. Thus, single-crystalline metals used for modeling industrial catalysis inherently lack the complexity needed to uncover many of the factors important to catalytic turnover and selectivity. Things such as metal support interactions, and the importance of metallic cluster size and spacing are all things of extreme importance to catalytic applications[5-7].

New model systems to be used for modeling these complex interactions are greatly needed. The use of planar supports for these new systems would allow the possibility of using surface science techniques to uncover adsorbate structure and verify support cleanliness as was the case with single crystals. Many different methods have been used recently to prepare different types of two-dimensional model catalysts such as spincasting of metal salt solutions onto planar oxide supports followed by calcinations[8], evaporation of metal films onto oxide supports[9-11], laser interference nanolithography[12], colloidal lithography[13], and photolithography[14]. All of these methods have problems, which limit their applicability to industrial catalysis. Non-lithographic methods are able to access the sub-100 nm size regime interesting for catalytic applications, but are unable to exert the control necessary to uncover the importance of metallic cluster size and spacing. Lithography techniques lend themselves nicely to the task of creating two-dimensional model systems as they have been used by the electronic industry for over two decades to produce sub-μm features uniformly and reproducibly. These lithographic methods, however, are just now approaching the ability to produce structures in the sub-100 nm size range.

The studies presented in this dissertation address the need for new two-dimensional model catalytic systems by the fabrication of sub-50 nm metallic features on planar oxide supports. All aspects of the metallic features have been controlled on the nanometer scale (height, width, and spacing) and offer a unique opportunity to study the effects of the system's structural aspects on catalytic activity. In addition, these supported catalysts offer facile change of material as the metal and support used is not limited, which offers the ability to study support-metal interactions. The fabrication methods utilized to create these model systems consist of traditional lithography techniques like I-line photolithography and deep-UV lithography as well as other lithographic techniques such as electron beam, size-reduction and nanoimprint lithographies. These techniques have been coupled to produce sub-50 nm platinum nanowires and nanoparticles by various experimental methods and have been used successfully to study catalytic reaction studies.

This dissertation will present the fabrication techniques used for creation of two-dimensional platinum model catalyst systems and their use to carry out the catalytic hydrogenation of ethylene and oxidation of carbon monoxide. Chapter 2 describes the various experimental techniques used throughout the course of this dissertation. Chapter 3 describes the production of platinum nanoparticles by electron beam lithography on silica and alumina thin films and compares the reaction kinetics of these nanoarrays for ethylene hydrogenation and the CO-poisoning of this reaction. Chapter 4 describes the use of I-line photolithography coupled with size-reduction and nanoimprint lithographies to produce platinum nanowires on oxide thin films of alumina and silica and also describes the reaction kinetics of these nanoarrays for ethylene hydrogenation and the

CO-poisoning of this reaction. Chapter 5 describes the production of platinum nanowire arrays on oxide thin films of zirconia, ceria, alumina and silica by use of deep-UV lithography coupled with size-reduction and nanoimprint lithographies, the CO oxidation reaction studies, and the annealing studies conducted to study the thermal stability of these nanowire arrays. Chapter 6 describes the coupling of several sub-lithographic techniques for creation of a parallel process to make platinum nanoparticles. Chapter 7 presents conclusions of this dissertation and proposes future work in the area of two-dimensional model catalysis.

References

1. M. Morbidelli, A. Gavriilidis, A. Varma, *Catalyst Design*, Cambridge University Press, New York, 2001.
2. Somorjai, G.A., *Introduction to Surface Chemistry and Catalysis,* Wiley, New York, 1994.
3. Somorjai, G.A., *Chemistry in two dimensions: surfaces,* Cornell University Press, Ithaca, New York, 1981.
4. J.R Anderson, *Structure of Metallic Catalysts*, Academic Press, London, 1975.
5. Bond, G.C. *Surf. Sci.*, **1985**, *156***,** 966.
6. Taylor, W.F.; Yates, D.J.C.; Sinfelt, J.H. *J. Phys. Chem.* **1964**, *68*, 2962.
7. Pajonk, G.M. *Appl. Catal.* **2000**, *202*, 157.
8. R.M. van Hardeveld, P.L.J. Gunter, L.J. Van Uzendoorn, W. Wieldraaijer, E.W. Kuipers, J.W. Niemantsverdriet, *Appl. Surf. Sci.*, 84, **1995**, 339.

9. X. Lai, T.P. St. Clair, M. Valden, D.W. Goodman, *Prog. Surf. Sci.*, 59, **1998**, 25.

10. J. Hoffmann, S. Schauermann, J. Hartmann, V.P. Zhdanov, B. Kasemo, J. Libuda, H.-J. Freund, *Chem. Phys. Lett.*, 354, **2002**, 403.

11. J. Libuda, H.-J. Freund, *J. Phys. Chem. B*, 106, **2002**, 4901.

12. M. Schildenberger, Y. Bonetti, M. Aeschlimann, L. Scandella, J. Gobrecht, R. Prins, *Catal. Lett.*, 56, **1998**, 1.

13. C. Werdinius, L. Osterlund, B. Kasemo, *Langmuir*, 19, **2003**, 458.

14. A.C. Krauth, K.H. Lee, G.H. Bernstein, E.E. Wolf, *Catal. Lett.*, 27, **1994**, 43.

Chapter 2

Experimental Techniques

2.1 Characterization

2.1.1 Ultra-High Vacuum Techniques

For many surface science applications it is necessary that ultra-high vacuum (UHV) techniques be used [1-3]. UHV offers two main advantages to atmospheric techniques. First, in order to truly study the surface of a sample, one must be able to keep the sample surface clean of atmospheric contamination for a reasonable amount of time, so that the experimental measurement may be taken. Second, many surface science measurement techniques rely upon measurements of electrons or ions emitted from the surface. For these measurements to be meaningful, there must be a reasonable signal arriving unimpeded to the detector. UHV is capable of offering both of these advantages.

When a sample is introduced to UHV from the atmosphere, it is covered with hydrocarbons and water from the atmosphere. As well, there are bulk impurities from samples that may surface segregate and cover the surface. All of these impurities may be cleaned from the surface by chemical reaction methods or by physical cleaning methods.

Cleaning by chemical reaction would mean exposure to an agent that reacts with the surface contamination to make a volatile product that would desorb from the surface. Physical cleaning methods like ion sputtering physically break up the impurities by bombarding the surface with ions of high kinetic energy. This would fragment and volatilize the surface contaminations. These cleaning methods, however, would be entirely useless without UHV, because clean metal surfaces are extremely reactive with carbon and oxygen compounds, which are abundant in atmosphere. Thus, the clean metal surfaces would be covered immediately after cleaning. This flux of impurities upon the surface can be eliminated by evacuating the system to a low enough pressure that the flux of molecules upon the surface will not be equal to a significant portion of a monolayer for a time period longer than the experimental measurement. The time necessary for an initially clean surface to be covered by a monolayer of adsorbed molecules can be calculated using the kinetic theory of gases (below)[4].

$$F = \frac{[N_A P]}{[2\pi MRT]^{1/2}}$$

Where F is the flux (impact rate) of molecules on the surface, N_A is Avogadro's number, P is the pressure, M is the average molecular weight of the gaseous species, R is the ideal gas constant and T is the temperature in Kelvin. This equation can be reduced down to the form below for ambient pressure expressed in torr[4].

$$F = \frac{[3.51 \times 10^{22}][P(torr)]}{[M(g/mole) \cdot T(K)]^{1/2}}$$

For molecular nitrogen or carbon monoxide (M = 28 g/mole) at 300 K and pressure of 1 x 10^{-9} torr, the flux upon a surface would be ~3.8 x 10^{11} molecules/ cm^2/sec. A metallic

surface such as platinum has a surface density of ~1.5 x 10^{15} atoms/ cm^2. If each molecule of CO or N_2 sticks to the surface upon striking it, it will take approximately 3900 seconds to create a monolayer on the metallic substrate. Thus, measurements can be made without threat of significant contamination from an adsorbed layer.

As mentioned above, many surface spectroscopic techniques depend on electrons or ions being emitted from the surface being studied. With UHV, it is possible for these signals to reach the detector without coming in contact with another particle. This is of extreme importance, if any reliable measurement is to be made of the energy or distribution of these emitted particles. The long mean free path in UHV allows for these particles to exit the sample and make it to the detector without colliding with other gas phase molecules in the system. The mean free path of an electron can be estimated by calculating the mean free path, λ, of a gas molecule:

$$\lambda = \frac{RT}{\sqrt{2}\pi N r^2 P}$$

Where T is the temperature in Kelvin, R is the ideal gas constant, P is the pressure in Pascals, r is the molecular radius, and N is Avogadro's number. For molecular nitrogen, with a molecular radius of 1.64 x 10^{-10} m, at 300 K and 10^{-9} torr, the mean free path would be 3.7 x 10^5 m. Thus, an electron emitted from the surface, which has a significantly smaller radius, will arrive at a detector in the system without any collisions with gas molecules.

The studies reported herein were conducted in a stainless steel UHV chamber equipped with a high-pressure reaction cell. The UHV chamber is evacuated with a 330 L/s turbomolecular pump (Balzers TPU 330), and a 440 L/s ion pump (Varian). The

chamber achieved a bakeout pressure of 5 x 10^{-10} torr and a working pressure between reactions of 1 x 10^{-9} Torr. The system is shown schematically in Figure 2.1. The inside of the reaction tube are gold-coated to minimize background reactions. The sample is heated with a polyboronitride heater (GE advanced ceramics, HT-01). This ceramic heater makes use of a pyrolytic graphite filament, which has a thermal expansion very close to the boronitride, enabling facile heating and cooling. Temperature is monitored by a 0.010" K-type thermocouple (alumel/ chromel). Both the thermocouple and the sample are attached to the heater by tantalum clips and are electrically isolated by use of alumina spacers (Figure 2.2). The heater is attached to two gold-plated electrodes, which are attached to a rotatable manipulator head. Gases are controllably admitted into the chamber by leak valves for sample cleaning. Surface cleanliness of the sample was monitored by Auger electron spectroscopy, which is described in detail below.

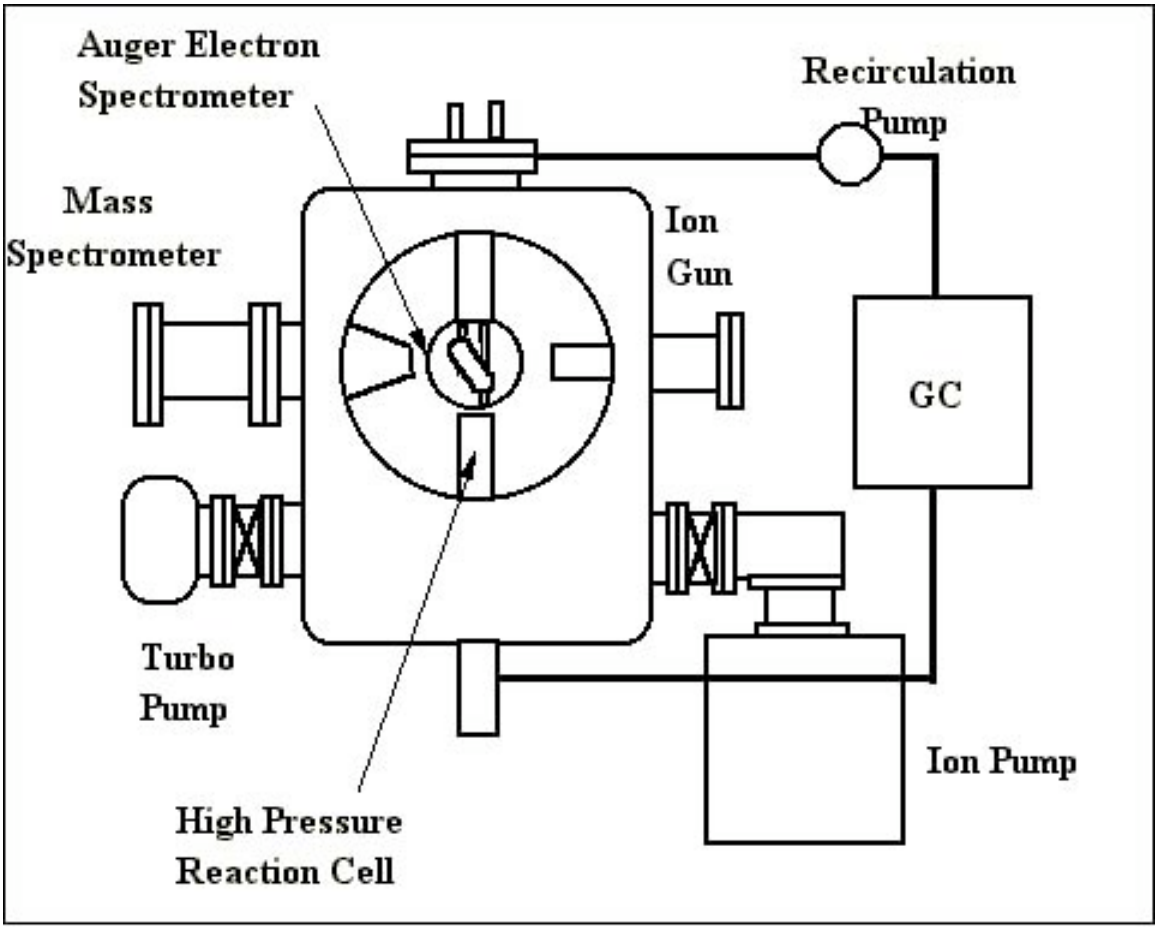

Figure 2.28: Schematic of UHV system coupled with high-pressure reaction cell

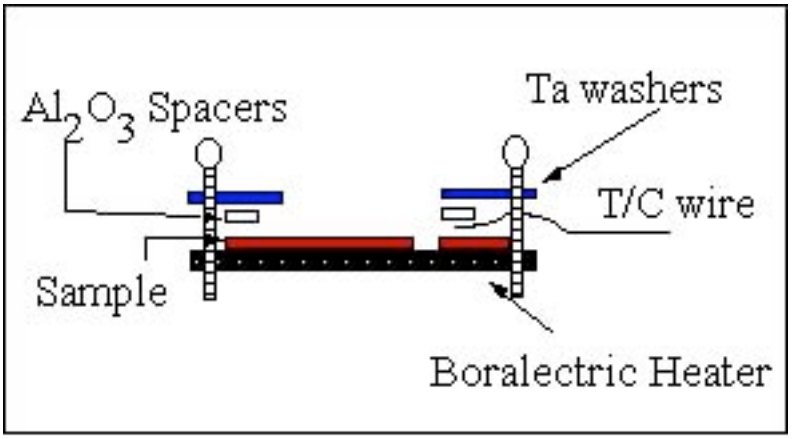

Figure 2.29: Mounting of sample and thermocouple assembly onto boronitride heater

2.1.1.1 Auger Electron Spectroscopy

As mentioned above, UHV allows the flux of molecules onto the surface to be slow enough that a measurement can be taken before a monolayer of contaminants covers the substrate. The problem remains, however, that the substrate surface needs to be verified as 'clean' or free of common contaminants from the atmosphere or bulk of the substrate. Auger electron spectroscopy (AES) is used to monitor the surface cleanliness of substrates being used for measurement or reaction[5-7].

In an Auger process, highly energetic electrons (1-5 keV) strike the surface of the substrate. This electron bombardment ionizes atoms in the substrate, and core shell electrons are emitted. Electronic emission leaves a core hole in the ionized atom. The potential energy of this ionized atom is reduced by a subsequent electronic relaxation to fill the core hole and an emission of energy[8]. This energy emission can come in the form of a photon (x-ray fluorescence) or in the form of electronic emission of a second, more loosely bound electron (Figure 2.3a-d). Photon emission is only dominant when the core hole is 10 keV or more[9]. The secondary electron that is emitted is called the Auger electron. These electrons can be collected and analyzed for their kinetic energy. This kinetic energy is indicative of the spacing of the energy levels of the ionized atom. Certain energy level spacings are indicative of specific elements and thus can be used to give an atomic makeup of the sample. AES is a surface sensitive technique due to the short mean free path of electrons in a solid. Secondary electrons tend to have kinetic energies on the order of 15 – 1000 eV, which limits the mean free path to between 1 and 2 nm. The electron mean free path does differ with the kinetic energy of the electron, and

a plot of the mean free path of the electron versus the kinetic energy, commonly called 'The Universal Curve'[9], demonstrates this energy dependence (Figure 2.4).

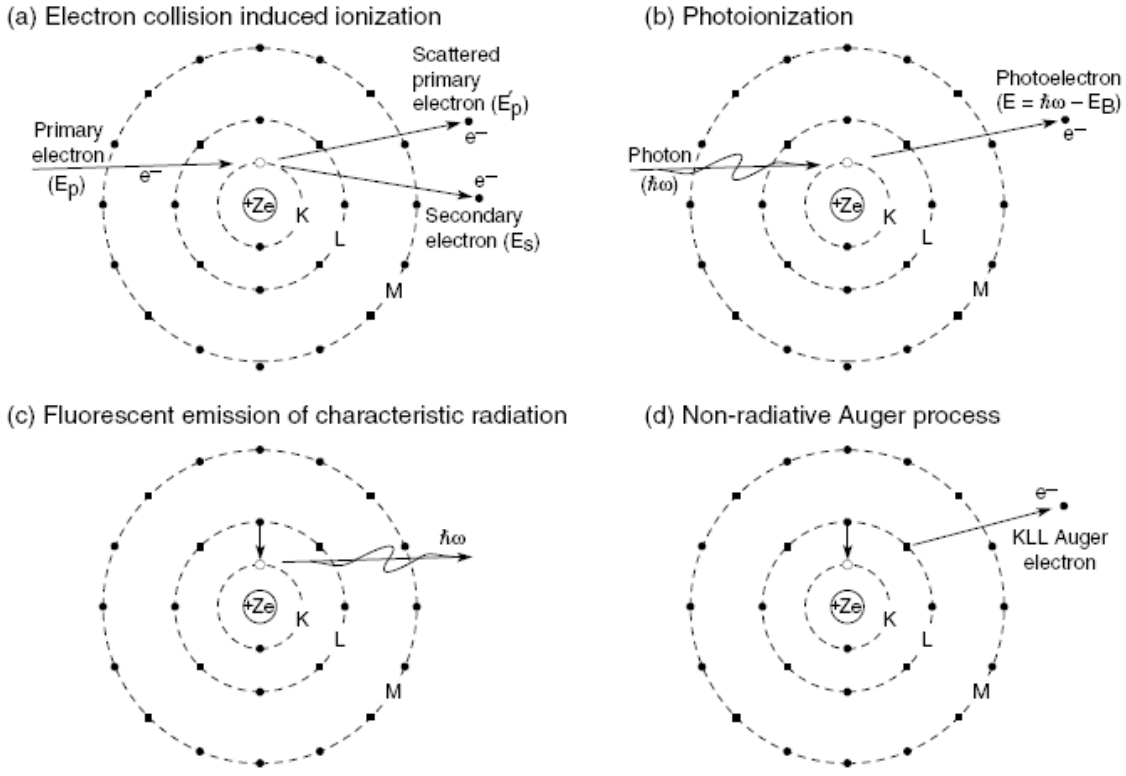

Figure 2.30: Depiction of processes occurring after electron bombardment of sample surface.

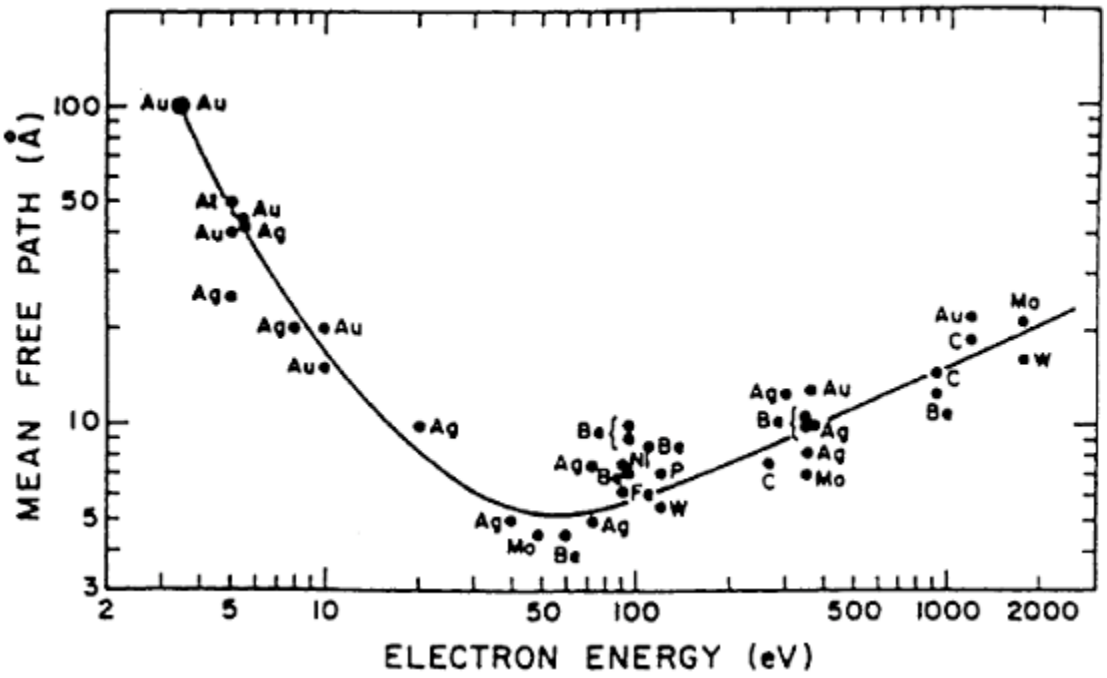

Figure 2.31: Universal curve showing the inelastic mean free path of electrons in a solid plotted as a function of electron kinetic energy.

The Auger electron is a secondary electronic emission, so its kinetic energy is not dependent upon the excitation energy used. It is a three energy level process and is dependent upon the spacing of those energy levels. For example, if the core energy level ionized is E_K, then a more loosely bound electron from energy level E_{L1} can relax down to fill the core hole at E_K and emit a secondary electron from E_{L2}. This process is shown schematically in Figure 2.5. When the Auger electron is emitted, it ejects with a characteristic kinetic energy specific to the element from which it is excited. If the three energy levels involved in the process are E_K, E_{L1}, and E_{L2}, as above, then this energy can be calculated from the equation:

$$E_{KLL} = E_K - E_{L1} - E_{L2} - U$$

where E_{KLL} is the kinetic energy of the Auger electron, E_K, E_{L1}, and E_{L2} are the normal one-electron binding energies and U is the hole-hole interaction energy. The normal one-

electron binding energies are those usually measured in x-ray photoelectron spectroscopy, which include one-hole relaxation effects. The U in the equation takes into account the effects of having two electron holes and can be separated into two terms.

$U = H - P$

In this equation, H takes into account the hole-hole interaction energy in the free atom and the P takes account of the relaxation effects of the solid-state environment.

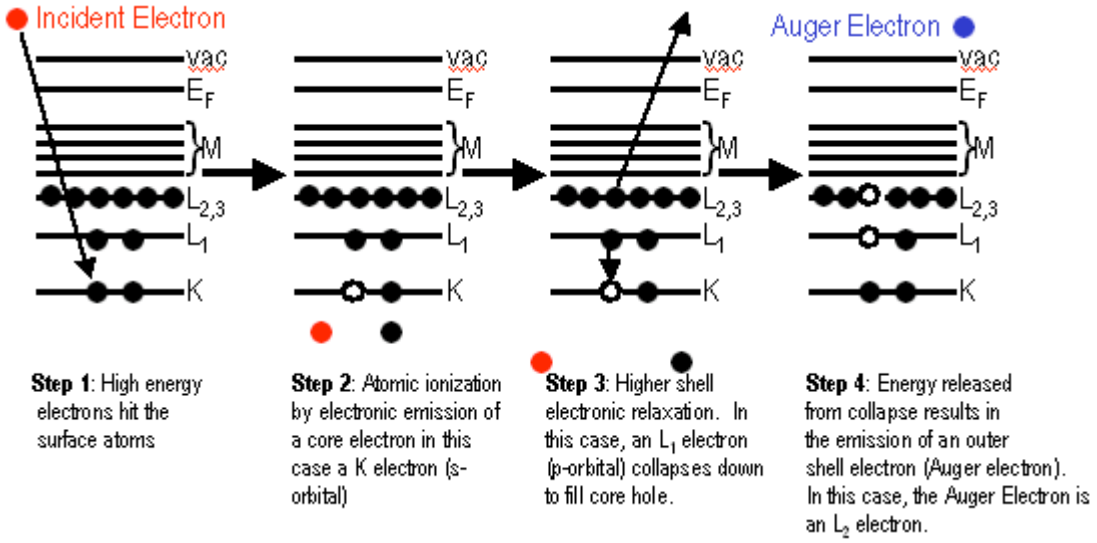

Figure 2.32: Auger electron emission process.

When the Auger electrons are emitted from the sample, they are collected and their kinetic energy is measured. The raw data recorded is then, electron current vs. kinetic energy. However, there is a large background signal of secondary electrons, which slowly varies. So, the signal, N(E), is differentiated with respect to E to distinguish the small Auger yield (dN(E)/dE) from the large background. This Auger yield (dN(E)/dE) or the number of electrons counted for an ABC Auger transition (Auger current) from species I, on the surface at a site x, y, z, can be written as:

$dN(E)/dE_i$ = (incident electron flux of energy E_p at x,y,z) □ (number of atoms of i at x,y,z) □ (ionization cross section of level A of species i at energy E_p) □ (backscattering

factor for energy E_p and incident direction) × (probability of decay of A level of species i to give ABC Auger transition) × (probability of no loss escape of electrons from x,y,z) × (acceptance solid angle of analyzer) × (instrumental detection efficiency)

The fact that terms 4 and 6 are sample dependent makes quantitative analysis of the Auger signal more difficult. However, this can be accomplished by using independent techniques such as low-energy electron diffraction, radioactive tracers, and quartz-crystal microbalance for creation of a very controlled sample to use in calibrating the Auger signal. Since the spectra are generally presented as the first derivative of the Auger signal, the calibration can be made using the peak-to-peak ratio rather than the area; however, the two ratios are equal if a Gaussian peak shape is assumed[10].

While this quantitative analysis is possible, AES is generally used to qualitatively verify that the substrate surface is clean for measurement and to verify surface species after reaction or measurement. For catalysis, AES works very well for this type of qualitative surface analysis. This is due to the fact that many catalytically relevant elements like C, Cl, S, Pt, Ir, and Rh have their main Auger electrons emitted with kinetic energies in the 100 – 300 eV range. This energy range would limit the mean free path of these electrons to less than 1 nm. Thus, AES would have an optimal surface specificity.

The AES spectra are taken with a Phi 13-255G double pass cylindrical mirror analyzer (CMA) coupled with a built-in electron gun. The electron beam comes in normal to the sample and has a kinetic energy of 3 keV. While taking the spectra, the sample is electrically grounded. The electrons emitted from the sample are collected and analyzed with the CMA. Only emitted electrons, which possess a specific kinetic energy, can pass through the space between the negatively charged outer cylinder and the

electrically grounded inner cylinders of the CMA to reach the electron multiplier (Physical Electronics, 20-075). The electrons enter into the CMA through a slot in the inner cylinder and are then deflected by a DC potential on the charged outer cylinder. For the electrons to go through the exit slot, they must equal the pass energy of the CMA. This pass energy is adjusted by use of a small, superimposed AC voltage, which is scanned to allow electrons with different kinetic energy to pass. If an electron has more kinetic energy than the pass energy, it will strike the outer cylinder, and if it has less kinetic energy than the pass energy it will strike the inner cylinder of the CMA. The signal registered at the electron multiplier is the electron energy distribution (N(E) vs. E). and has the same frequency as the original modulation. This signal is proportional to the derivative of the current to the voltage, which is recorded using a lock-in amplifier. For a more detailed discussion on the operation of CMA, further references can be consulted[6,9].

2.1.1.2 X-Ray Photoelectron Spectroscopy

X-ray photoelectron spectroscopy (XPS) is a technique that can be used to give an elemental make-up of a sample[6,8,9,11-13]. XPS is based on the photoelectric effect put forth by Einstein in 1905[14]. This process takes place by irradiating a sample with sufficient energy for electronic emission to occur. The number of electrons emitted depends on the intensity of the radiation being used (photon flux), and the kinetic energy of the emitted electrons is dependent upon the energy of the incident radiation.

In photoelectron spectroscopy, the sample is irradiated with a photon of energy hν. This photon penetrates the sample and is absorbed by an electron with a binding

energy E_b (with reference to the Fermi level). When the photon has sufficient energy to overcome this binding energy and the work function ( ) of the sample, the electron is emitted (Figure2.6).

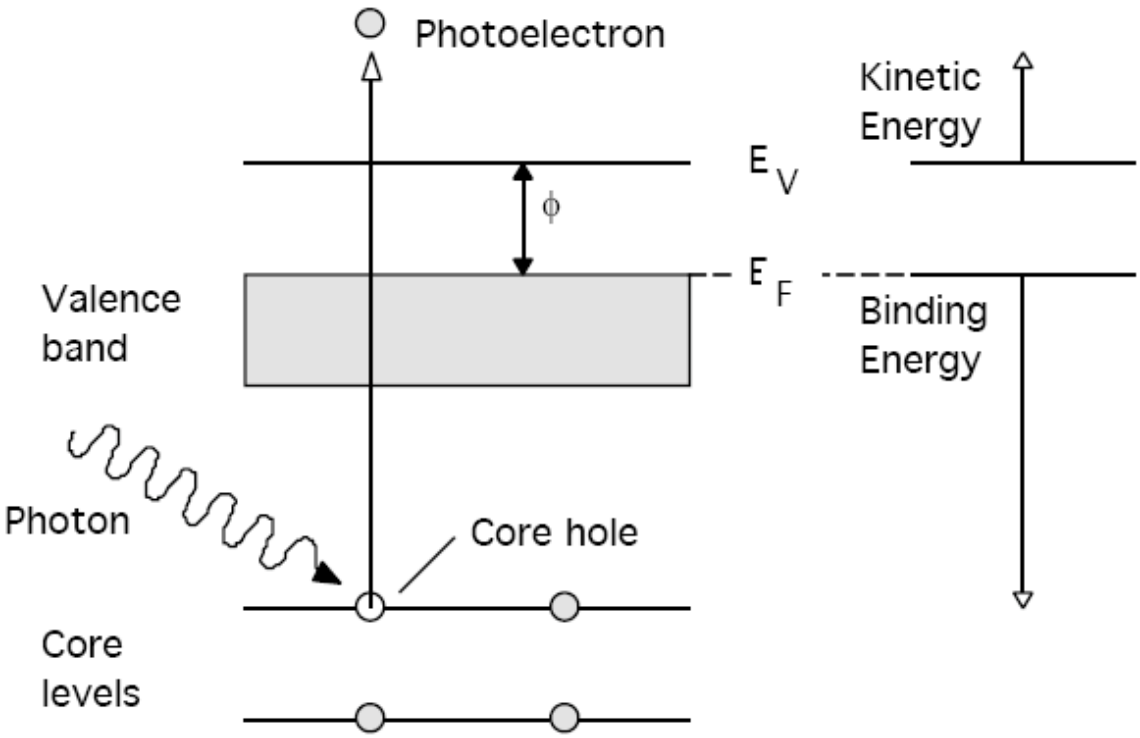

Figure 2.33: Photoelectron emission process. An incoming x-ray excites a core shell electronic emission. This photoelectron is collected and analyzed.

After this photoelectron is emitted, the electrons are collected and their kinetic energy is measured. With knowledge of this kinetic energy, the initial energy of the photon, and the work function of the sample, the binding energy, E_b, of the electron can be calculated by the equation shown below.

$$E_B = h\nu - E_K - \phi$$

Specific binding energies are indicative of specific elements in the sample. This equation, however, is an approximation and ignores several parameters that will affect binding energy of the electron, which can cause mislabeling of the peaks in the spectra.

If no relaxation followed photoelectron emission, then the binding energy would be the same magnitude of the orbital energy, which can be calculated by Hartree-Fock calculations. The calculated photoemission peaks, and the measured peaks can differ in energy anywhere from 10 eV to 30eV. There are a couple of things that happen to cause this difference in calculation and experiment, but the biggest difference is made by the solid electronic rearrangement to shield the core hole. When the photoelectron is emitted, the atom is left in a highly energetic state. Since the atom is within a solid, other surrounding electrons rearrange and shield the core hole. Thus, the emitted electron does not feel as great of a binding energy as orbital energy calculations would show. Therefore, the kinetic energy by calculation would undergo an apparent increase and the calculated binding energy would be smaller than expected. This solid-state relaxation needs to be corrected and the equation for binding energy would become:

$$E_B = h\nu - E_K - \Phi + E_R$$

Where E_R is the extra relaxation energy associated with the solid environment. An additional factor that comes into play is that the sample is electrically grounded to the system. This will create an additional slightly positive charge that the photoelectron must overcome to be emitted. This term can be added to the work function of the sample (Φ) to make a larger work function for the material, which would just be considered the work function of the spectrometer, $\Phi_{spectrometer}$ (Figure 2.7). The binding energy would then be:

$$E_B = h\nu - E_K - \Phi_{spectrometer} + E_R$$

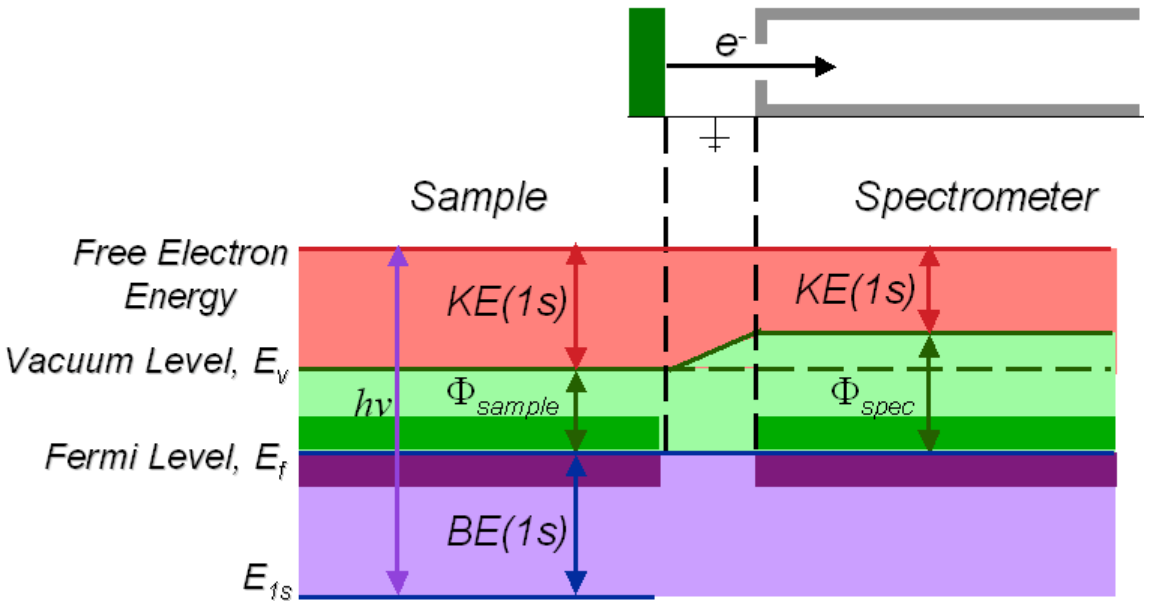

Figure 2.34: Energy level diagram of XPS process.

The sample is irradiated with nearly monochromatic soft x-rays of energy between 1 and 1.5 keV. The x-ray excites a core shell electronic emission and the core shell electron (photoelectron) is collected and analyzed for its kinetic energy as explained above. With binding energies on the order of 1-1000 eV, and work functions of ~5 eV, the emitted photoelectron will have a kinetic energy between 250 eV and 1450 eV. Thus, the mean free path of the photoelectron would be under 3 nm, and the photoelectrons excited out of the surface would be limited to the first few atomic layers.

As was mentioned in the section 2.1.1.1, when a core hole is created, an Auger process can result (Figure 2.8) due to a more loosely bound electron relaxing to fill the core hole. The kinetic energy of an Auger electron does not depend on the energy of the excitation source, whereas the kinetic energy of the photoelectron does have this dependence. Therefore, Auger electrons can be identified and separated from the photoelectron peaks, by changing the excitation source. If the kinetic energy of the emission changes positions by the same amount as the change in energy of the excitation

source, then it is a photoelectron. If the kinetic energy stays the same, then it is due to an Auger transition.

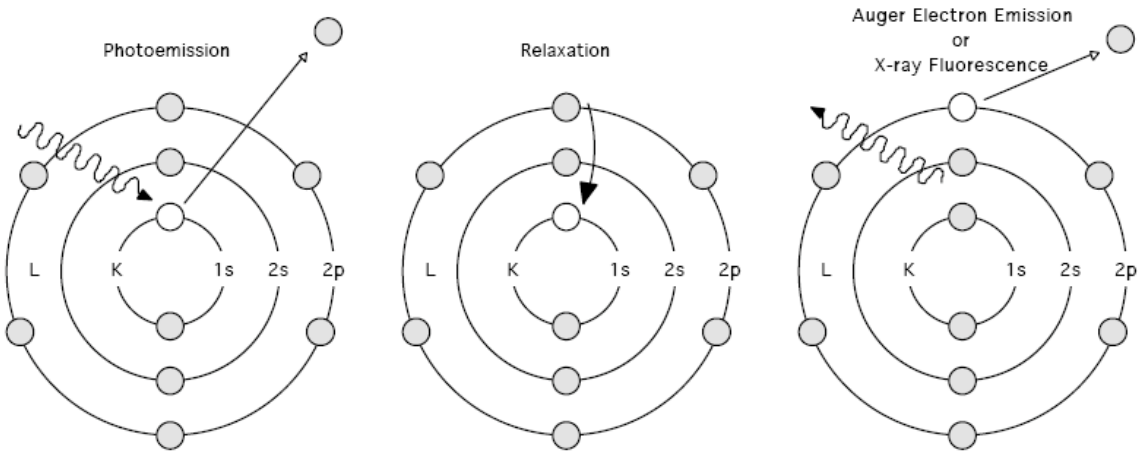

Figure 2.35: Upon core-shell electronic emission, relaxation of a more loosely bound electron can result in either photon emission (x-ray fluorescence) or another electronic emission (Auger electron).

The binding energy of the core and valence electrons is a function of the chemical environment and oxidation state of the surface atom. The position of the peaks in the spectrum thus identifies different elements, and the shifts in the binding energies of core electrons indicate different oxidation states of the same element. Chemical shifts of the same element with different oxidation states can be on the order of 0-3 eV from known standards. When electron density is removed from an element, as takes place with oxidation, the core and valence electrons feel a stronger attraction towards the nucleus. The charge at the nucleus stays the same, but there are not as many electrons present to balance out the positive charge. Thus, each electron has more positive potential energy attracting it towards the nucleus than before and is therefore bound more strongly to the atom. This additional binding energy is what is seen in the photoemission spectrum and is what allows deciphering of different oxidation states of the atom. The chemical shift

of the photoemission peak is then dependent on both the initial oxidation state and the final ionized state and can be calculated using the point charge model as shown below.

$$E_i = E_i^0 + kq_i + \sum q_i / r_{ij}$$

Where E_i is the binding energy of an atom, i, E_i^0 is the binding energy of atom i at a given reference state, kq_i is the weighted charge of atom i, and $\sum q_i / r_{ij}$ is the sum of all the potentials at atom i due to the surrounding charges. XPS, then, does not just give an elemental makeup of the surface, but also gives information as to the nature of the sample surface. The compositional analysis of a sample is carried out by comparison of peak areas and heights in the spectrum. To do this quantitatively, the peak areas must be integrated and divided by the atomic sensitivity factor for the orbital responsible which emits the photoelectron. Atomic sensitivity factors account for the probability that the atomic orbital will be excited by a photoelectron (photoelectric cross section), the mean free path of the photoelectron, and the detection efficiency for electrons emitted from the sample. Atomic sensitivity factors change instrument to instrument, which must be taken into account if an absolute elemental surface concentration is to be calculated. However, many studies focus on the change of peak ratios as the treatment of the sample changes. This give the relative change of two different peaks on the surface and giving an indication of the chemistry that is occurring. The photoelectric current, I, is the signal collected from the photoelectron emission of the sample (below).

$$I = N\sigma DJL\theta AT$$

Where N is the number of atoms per unit volume of sample, σ is the photoelectric cross section, D is the detector efficiency, J is the photon flux, L is the orbital symmetry factor, θ is the inelastic mean free path of the photoelectron, A is the analysis area (determined

by solid angle of collection from detector), and T is the analyzer transmission efficiency. The concentration of a particular element in the surface of the sample is then:

$$N = I / (\sigma DJL \lambda AT)$$

Where the denominator ($\sigma DJL \lambda AT$) is the atomic sensitivity factor (ASF) discussed above. Then the relative concentration, C, of a particular element, x, in the analyzed volume of the sample would be the fraction of the signal from the element x divided by the sum of the signal from all other species, i, in the sample. The expression would then be:

$$Cx = [Ix/(ASF)x] / [\sum In/(ASF)n]$$

As mentioned above, there are spectral contributions from Auger electrons as well as photoelectrons. Other peaks in the spectrum can be from shake-up contributions and plasmon excitations. Shake-up losses are final state effects, which arise when the photoelectron imparts energy to another electron of the atom upon emission. This causes a loss of part of the photoelectron's kinetic energy, which will make the binding energy appear to be higher. When the energy of the photoelectron is transferred to the plasmon excitation in a metallic sample, multiple smaller peaks may appear at specific energy distances away from the photoelectron peak on the higher binding energy side.

XPS experiments are performed with a Physical Electronics PHI 5400 ESCA system equipped with a dual target x-ray source of Al K_α (1486.6 eV) and Mg K_α (1253.6 eV). The x-rays were not filtered and not monochromatic, which resulted in satellite peaks that were removed by processing of the spectral peaks. Regardless of which excitation source was used, an acceleration voltage of 15 kV was used for the x-ray target with a power of 400 W. The system was maintained at a base pressure of approximately

8×10^{-9} torr and made use of a differentially pumped load lock to input samples. Thus maintaining UHV while allowing facile sample exchange. Electrons are detected with a hemispheric energy analyzer mounted at a 45-degree angle with respect to the sample. The samples are electrically grounded through metallic sample holders and are inputted through the load lock into the UHV portion of the chamber by use of a transfer arm. Carbon and oxygen 1s peaks from atmospheric contaminations are used as internal calibration peaks.

2.1.2 Microscopy Techniques

The work detailed in this dissertation involves many fabrication techniques all aimed at modeling catalysis in two-dimensions. The catalyst samples consist of sub-100nm metallic features on an oxide thin-film support. The samples proceed through many fabrication steps before completion and must be inspected between process steps to ensure that the process is accomplishing the anticipated result. While chemical identification of the surface species is important, a picture of the surface is invaluable to fabrication. The two techniques most heavily used for characterization of the process steps in fabricating the two-dimensional catalysts are scanning electron microscopy (SEM), and atomic force microscopy (AFM). SEM measurements are used to verify spacing of and width of the fabricated structures, and AFM measurements are used to verify the height of the structures.

2.1.2.1 Atomic Force Microscopy

Atomic force microscopy (AFM) was developed as a method of imaging surfaces that were insulating in nature[15-17]. Its parent technique, scanning tunneling microscopy has the capability of giving atomic resolution of surfaces, but is limited to substrates that are electrically conductive[18,19]. AFM can give topographic images of electrically conductive and insulating surfaces and additionally is capable of giving surface roughness and friction measurements of the surface. The principle of AFM works in the following manner. A probe, which is an extremely sharp tip, is brought to the vicinity of the sample surface and interacts with the surface through various potentials it encounters. As the tip is scanned across the surface, the topographic and material change of the sample will change the interaction and the information can then be used to form an image of the sample surface.

The sharp tip brought into the vicinity of the sample generally has a radius of curvature between 10 and 20 nm (Figure 2.9c). It is attached to a reflectively coated flexible cantilever (Figure 2.9b). A laser (HeNe) is reflected off of the cantilever into a position sensitive photodiode (Figure 2.9a). The tip approaches the sample by use of a micron scale stepper motor followed by finer approach by a piezoelectric actuator. When the tip comes into contact with the sample surface, the cantilever flexes and the beam moves on the photodiode. The photodiode is split into quadrants, and the beam is initially centered between the four quadrants (Figure 2.10). Thus, when the cantilever flexes and the beam position moves, the photodiode measures this movement by the difference in potential from one quadrant to the other. If the potential difference is between the upper two quadrants and the lower two quadrants, then the movement is due

to topography. When the cantilever experiences torque and there is a voltage difference measured between the two left and two right quadrants, it is due to surface friction, which can be measured. The tip is moved across the surface by use of the above-mentioned piezoelectric actuator. The piezoelectric actuator is a non-centrosymmetric ceramic material, usually $BaTiO_3$. This solid-state material actually alters its structure when exposed to an applied potential. This structural alteration changes the length of the ceramic material on the Å-nm scale. A typical piezoelectric material will expand ~1nm per applied volt. There are four piezoelectric legs on the actuator. By applying a potential across one leg and the opposite potential across the leg across from it, the actuator can bend with reproducible precision on the sub-nm scale. In this way, the tip is moved in a raster pattern across the surface. When, the tip encounters forces along the surface, the cantilever bends, and the topography is mapped as mentioned above.

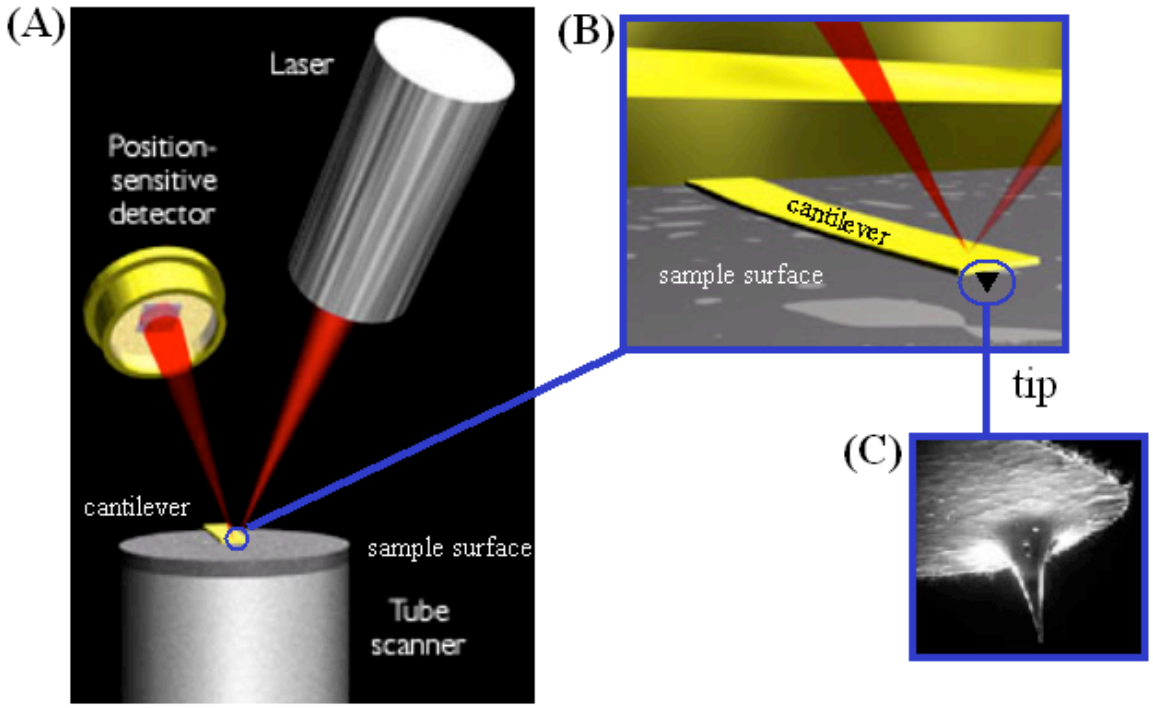

Figure 2.36: Instrumental setup of AFM (a) complete configuration showing laser beam reflecting off of the cantilever into the position sensitive photodiode (b) close-up picture of the laser reflecting off of the cantilever with tip attached (c) electron micrograph of a sub-20 nm AFM tip.

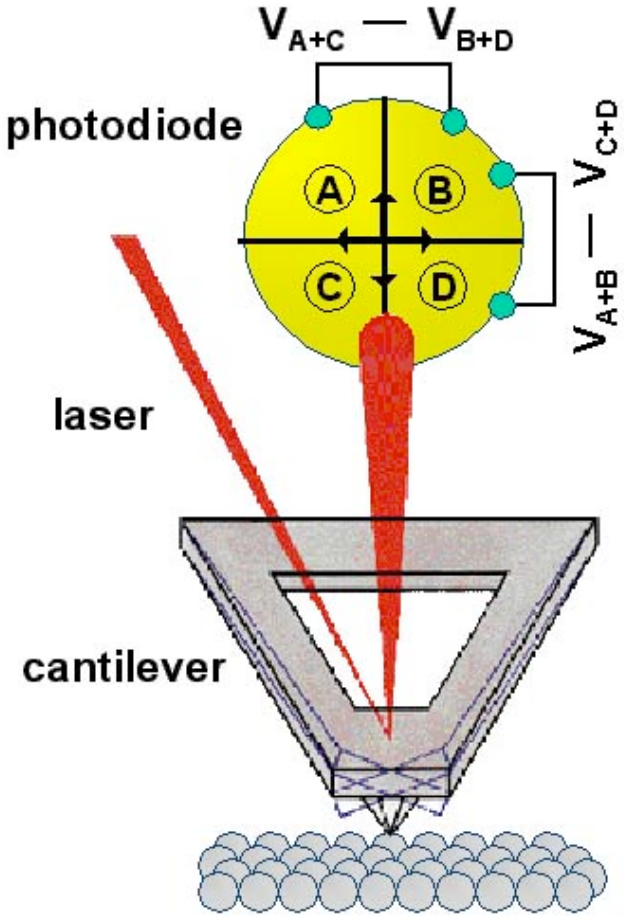

Figure 2.37: The AFM measures tip movement by the change in voltage across the quadrants in the photodiode. The beam is initially centered, so that up and down movements registers a difference in potential between the upper two and lower two quadrants (topography), and side-to-side movement registers a difference between the right and left quadrants. Side-to-side movements are registered due to torque on the tip, which can give surface friction information.

When moved across the surface the tip will encounter many forces including van der Waals forces, adhesion forces, capillary forces due to surface contamination, electrostatic and mechanical contact forces.

Van der Waals forces are attractive forces experienced by all atoms due to their instantaneous fluctuating dipoles. The dipole interaction potential, is a function of the distance, r, between the dipoles and can be written as:

$$V(r) = -\frac{C}{r^6}$$

Where C is the dipole interaction constant, which changes depending upon the nature of the interaction (i.e. dipole-dipole, dipole-induced dipole). The van der Waals forces in AFM, however, are not so straightforward, because both the tip and the sample are composed of many atoms. To account for this the Hamaker assumption[20] can be used, which assumes additivity, a continuous medium, uniform material property, and non-retarded interaction. Assuming all of this, the total force between the tip and sample can be integrated. If the end of the tip is considered a sphere with radius R and the sample a flat plane, the interaction potential between them is:

$$V = -\frac{HR}{6d}$$

where d is the distance between the sphere (tip) and the plane (sample), and H is the Hamaker constant given below.

$$H = \pi C \rho_1 \rho_2$$

Where C is the interaction constant, ρ_1 and ρ_2 are the atomic number densities of the interacting bodies. By differentiating the potential with respect to d ($-\partial V/\partial d$) the van der Waals force can be obtained.

$$F = -\frac{HR}{6d^2}$$

Adhesive forces occur when the probe is in contact with the surface. If the same model of a sphere interacting with a plane is used, the adhesion force can be approximated by:

$$F_A = 4\pi R\gamma$$

where γ is the surface energy of the interface between the tip and the sample.

As mentioned above in section 2.1.1 on UHV, when a sample is in ambient air, the surface is covered with a thin layer (< 50 nm) of contaminants consisting of mainly water and hydrocarbons. This surface contamination can cause an attraction of the tip to the sample surface. This force is called a capillary force and its magnitude can be expressed as:

$$F_c = 4\pi R\gamma\cos(\theta)$$

Where θ is the contact angle, and γ is the water surface tension

Electrostatic interactions occur most notably on insulating surfaces. Insulating surfaces can store charge, which can interact very strongly with the AFM tip. These forces can be strong enough to bend the cantilever when scanning across the surface.

Repulsive contact force happens when the tip and the sample are in physical contact and continuum mechanics models have been developed to describe the interaction. The three most widely used models are the Hertz model[21], the JKR model[22] and the DMT model[23]. For detailed information, the original papers can be consulted.

The AFM studies were performed on two different instruments: Park Scientific Instrument Autoprobe M5 and Molecular Imaging Pico SPM 100. The systems consisted of a detachable scan head, force detection system, feedback electronics, and noise damping components. The feedback electronics could be manipulated depending on the mode of operation for the AFM. When the feedback circuit is switched on, the tip-sample distance was kept constant, resulting in a constant force between the tip and the

sample. When the feedback circuit is switched off, the tip scans across the sample surface at constant height. This mode of operation is used to generate a spatial map of the interaction force (topography). Noise damping components are incorporated into the system to improve the signal-to-noise ratio. For the images presented in this dissertation, the AFM was operated under constant force mode.

2.1.2.1 Scanning Electron Microscopy

Stintzing first proposed the idea of a scanning electron microscopy (SEM) in 1927[24] based on the work of de Broglie[25] and Busch[26]. The SEM is now the most widely used method of imaging a surface with sub-micron dimensions. In SEM, a stream of electrons is emitted from an electron gun and accelerated towards a sample to be analyzed. This stream of electrons is accelerated through several metal apertures and magnetic lenses until it is focused into a highly energetic beam of electrons. This electron beam is moved across the sample by means of electromagnetic deflection coils in a raster pattern and the backscattered and secondary electrons emitted from the surface are collected. These electrons are counted and the signal is used to form an image of the surface[27-30]. The setup of a scanning electron microscope is shown below in Figure 2.11.

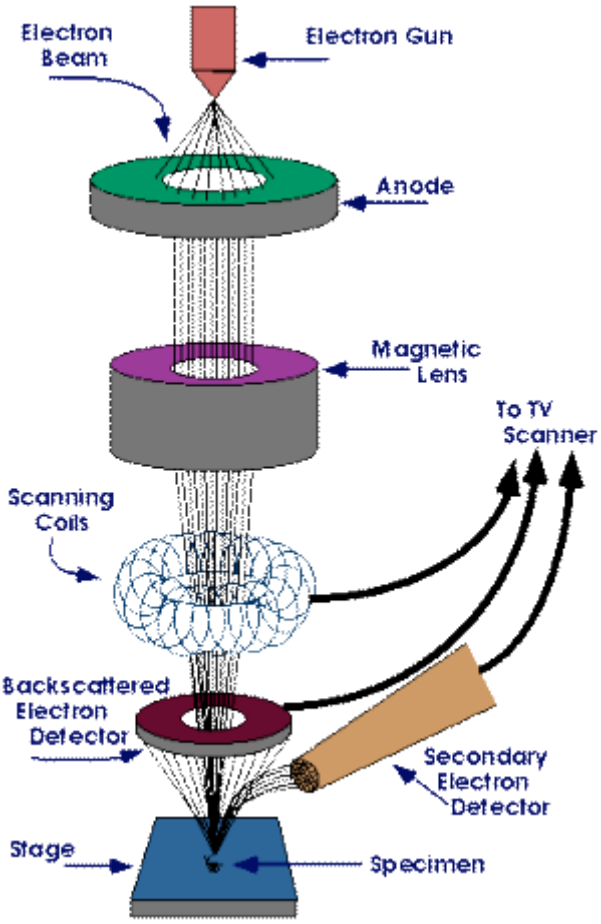

Figure 2.38: Schematic of scanning electron microscope.

Several different type of electron guns can be used to produce the stream of electrons used in SEM. Conventionally, a tungsten hairpin filament can be heated by running an electrical current through it until thermionic electron emission occurs. A tungsten filament electron gun can provide a brightness of between 10^4 and 10^5 A $cm^{-2}sr^{-1}$ with an acceleration voltage of about 10kV. This brightness will achieve a current of a few picoamps at the sample surface in a probe of about 5-nm diameter. The signal to noise ratio using a tungsten hairpin filament is not optimal however. This can be improved by used of a LaB_6 filament. This filament also emits electrons thermionically but has a higher brightness. Since the probe size will be approximately the same, but the

source is brighter, there will be a better signal-to-noise ratio. The highest source brightness, 10^8-10^9 A cm^{-2} sr^{-1} is achieved with a cold field emission source. For this type of electron gun, a DC potential is applied to a sharp tungsten tip ($r_{tip} < 100$ nm). The electric field at the tip is the largest and can be calculated by:

$$E = \frac{V}{r_{tip}}$$

When the electric field is high enough at the tip, electrons are emitted from the tip towards an accelerating voltage at the first anode. Below in Table 2.1, the three described electron guns are compared.

Electron Gun Type	Brightness (amp/cm^2/sr)	Source Size	Energy Spread	Vacuum Required (torr)
Tungsten	10^5	25 m	2-3 eV	10^{-6}
LaB_6	10^6	10 m	2-3 eV	10^{-8}
Cold Field Emitter	10^9	5 nm	0.22 eV	10^{-10}

The electron gun provides a large, stable current , which is accelerated through the column towards the sample. The first magnetic lens that the beam runs through is the condenser lens. The first condenser lens forms the beam and limits the amount of current in the beam. It works in conjunction with the condenser aperture, which further constricts the electron beam and eliminates high-angle electrons from the beam. There are usually two condenser lenses within the electron column followed by an objective lens, which provides the final focusing of the electron beam before it impinges upon the sample. This final lens (the objective lens), is the most critical lens in controlling the resolution of the microscope. Its function is to focus the image by controlling the movement of the probe along the optical axis of the column and to focus the electron beam further. The resolution in SEM has a lot to do with the size of the electron probe on the sample surface. Therefore, lens aberrations that can severely enlarge the final spot

size must be carefully eliminated to ensure resolution. Higher acceleration voltage (~30 kV) can also help to reduce the size of the electron beam, but causes imaging problems due to surface charging. With a field emission source, the same electron beam size can be achieved with a lower acceleration voltage (1-10 kV), which can eliminate the sample-charging problem and still give good resolution.

Exposure of the sample to the electron beam causes two different types of interactions, elastic and inelastic. Elastic scattering produces backscattered electrons while inelasatic scattering generates secondary electrons, Auger electrons, characteristic and bremsstrahlung x-rays, and cathodoluminescence. The backscattered electron is the dominating feature in the distribution. At much lower energies, below 50 eV, the number of electrons emitted from the specimen increases sharply to a level much greater than the expected contribution from backscattered electrons, these electrons are called secondary electrons. They are produced as a result of interactions between energetic electrons and the loosed bound conduction band electrons in metal or outer-shell valence electrons in semi-conductors and insulators. Because the difference in energy between the incident electrons and the specimen electrons, the energy transfer is not efficient and leads to the small kinetic energy of the secondary electrons. In fact, most of the secondary electrons have energy below 10 eV. In SEM, secondary and backscattered electrons are collected and processed to form an image of the sample. Both signals depend on the sample surface topography and chemical composition. The secondary electron emission is more sensitive towards topographic variations on the sample surface and confined to a volume near the beam's impact area, permitting images to be obtained at relatively high resolution. The more energetic backscattered electrons, on the other hand, are more

chemically sensitive, due to the Z^2 (Z = atomic number) dependence of the backscattering event, and have a larger interaction volume. Therefore the images taken with backscattered electrons tend to have lower resolution, but they also offer an atomic number contrast between different elemental compositions. So, images taken of planar samples with features in the substrate of different chemical composition will show a difference in contrast despite the absence of topography.

The SEM images presented in this dissertation are taken with a JEOL JSM-6340F field emission SEM. The typical experimental parameters used were 5 – 10 kV acceleration voltage, 12 μA emission current, and working distance of 6 mm.

2.2 Fabrication Methods

Model catalyst samples have been made by making extensive use of microfabrication techniques generally used for electrical engineering in both industry and academia. The four main lithography techniques used in making these catalyst samples, electron-beam lithography, photolithography, size-reduction lithography, and nanoimprint lithography, are described in detail below. The specific experimental details of the use of these techniques in the fabrication of the catalyst samples are given in further chapters.

2.2.1 Electron Beam Lithography

Electron beam lithography (EBL) is a high-resolution patterning technique used for fabrication of masks used in photolithography and direct pattern generation onto a wafer[31]. In EBL, the pattern is generated in several steps. First, a wafer is coated with

an electron-sensitive polymer. Next, the pattern is written into the polymer coating by exposure of the polymer to the electron beam. The electron beam breaks up the exposed polymer backbone and allows for development of the pattern by a developer solution, which selectively dissolves lower molecular weight polymer fragments. After pattern development, the wafer substrate is exposed. Upon exposure of the underlying substrate, either a material may be directionally deposited through the pattern onto the substrate surface, or the pattern may be transferred into substrate surface by using the patterned polymer as an etch mask. For the purposes of model catalyst creation a metal thin film is deposited through the pattern onto the substrate surface. After the pattern has been transferred either by etching or material deposition, the polymer mask is removed by immersing the sample in a solvent bath to dissolve the mask, and only the patterned wafer remains. This process is shown schematically below in Figure 2.12. The materials shown below are those used for fabrication of Pt nanoparticles described in Chapter 3.

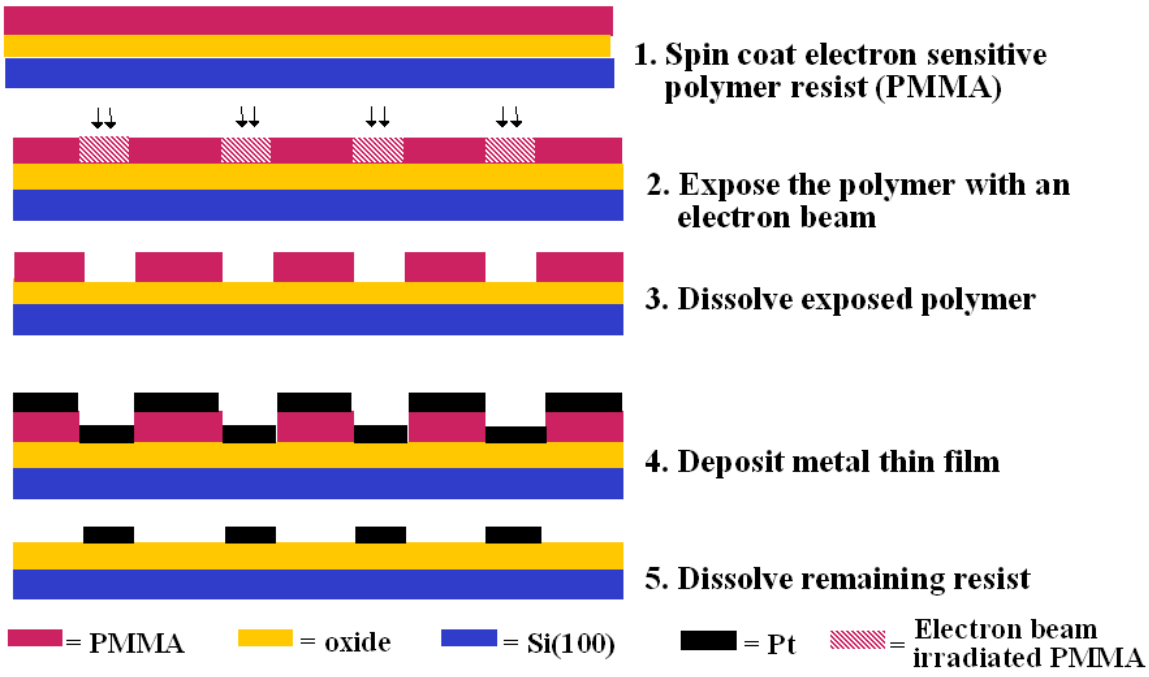

Figure 2.39: Scheme of electron beam lithography fabrication process.

The high-energy electrons used to expose the polymer are accelerated towards the sample with energy between 10-100 keV, focused into a narrow beam and then used to expose the electron-sensitive resist. The electron optics used in EBL instrumentation is very similar to that used for SEM. The beam must be confined down and focused to a spot < 5 nm similar to SEM. A main requirement for EBL system is the exposure control system, which determines not only the electron dose but also the position of delivery on the sample surface. The generic setup of an EBL system is shown in Figure 2.13[32] and a more detailed structure is shown in Figure 2.14.

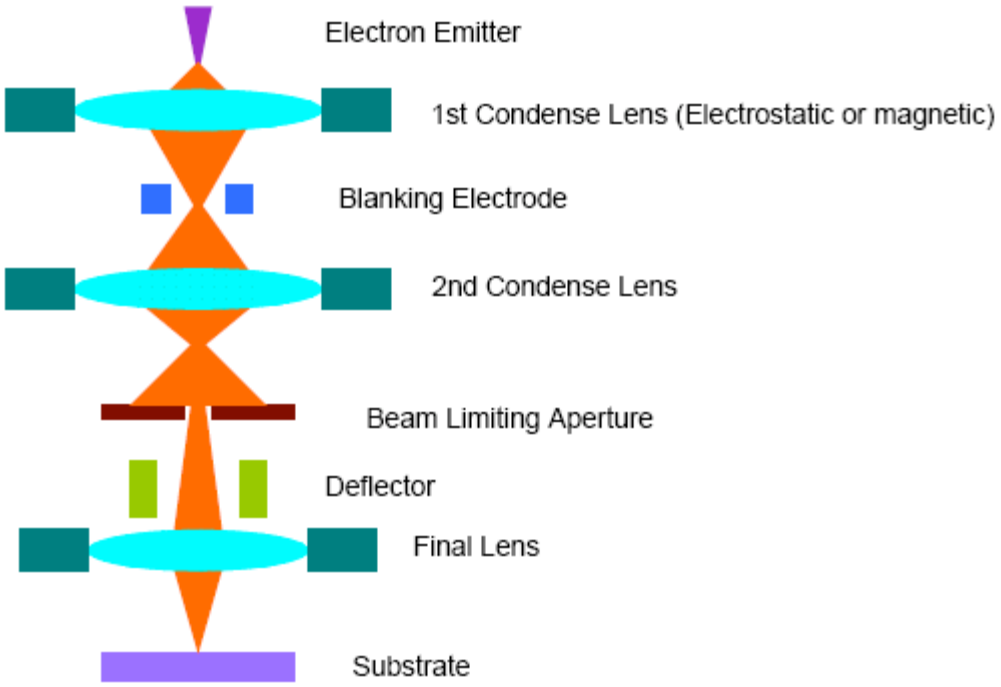

Figure 2.40: General setup of an EBL system.

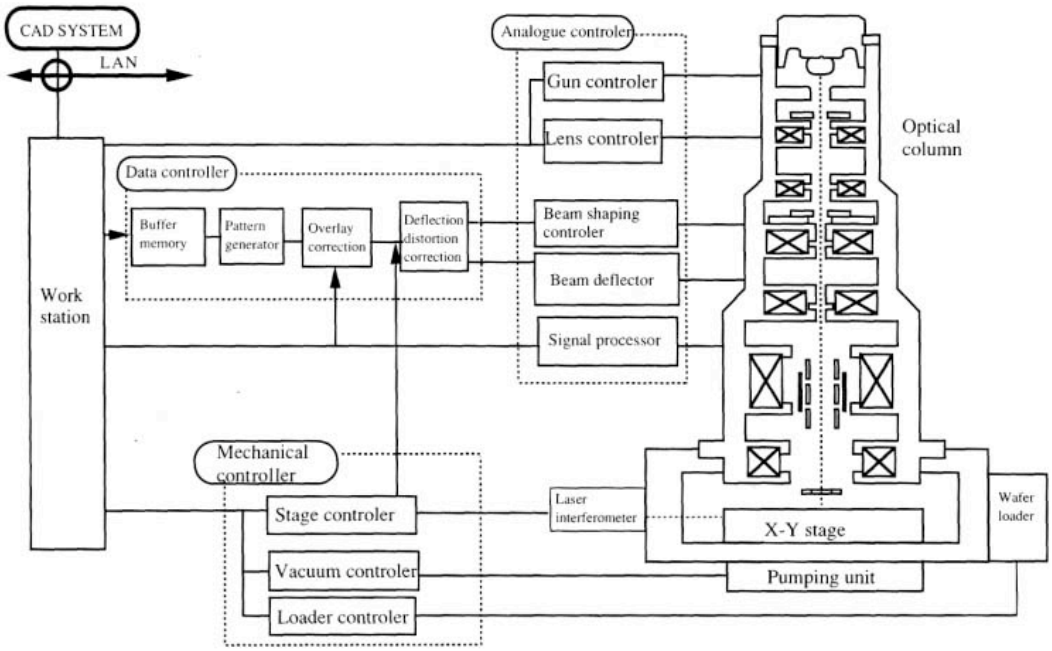

Figure 2.41: Detailed schematic of electron beam lithography fabrication system.

The minimum feature size generated by EBL is not limited by diffraction as is the case with conventional photolithography. With an acceleration of 100 kV, the de Broglie wavelength for the electrons in the beam is on the order of picometers. The resolution is instead controlled by the electrons scattered after impinging upon the substrate and electrostatic effects (Figure 2.15 from, ref. 32). These scattered electrons have relatively high energy and can expose some resist outside of the intended exposure area. This phenomenon is called the proximity effect. The energy deposited on the sample surface can be expressed in the following double gaussian equation[33]:

$$f(r) = \frac{1}{1+\eta}\left\{\frac{1}{\beta_f^2}\exp\left(-\frac{r^2}{\beta_f^2}\right) + \frac{\eta}{\beta_b^2}\exp\left(-\frac{r^2}{\beta_b^2}\right)\right\}$$

where r is the distance from the irradiation point, β_f is the forward scattering range, β_b is the backscattering range, η is the ratio of back-scattering energy to the forward scattering

energy. Both forward scattering in the resist and backscattering from the substrate contributes to the proximity effect. However, due to the low atomic number of the resist and long range of backscattering electrons, the backscattered electrons contribute much more to the exposure of resist outside of the impact point. A variety of methods have been developed to compensate for this proximity effect. These methods include the use of a thinner layer of resist, adjustment of the acceleration voltage, use of a thinner substrate, adjustment of the beam shape and size, and adjustment of the dose level to compensate for scattering. Sub-10 nm beam size has been demonstrated with EBL and sub-15 nm features can be routinely obtained with the latest tools[34].

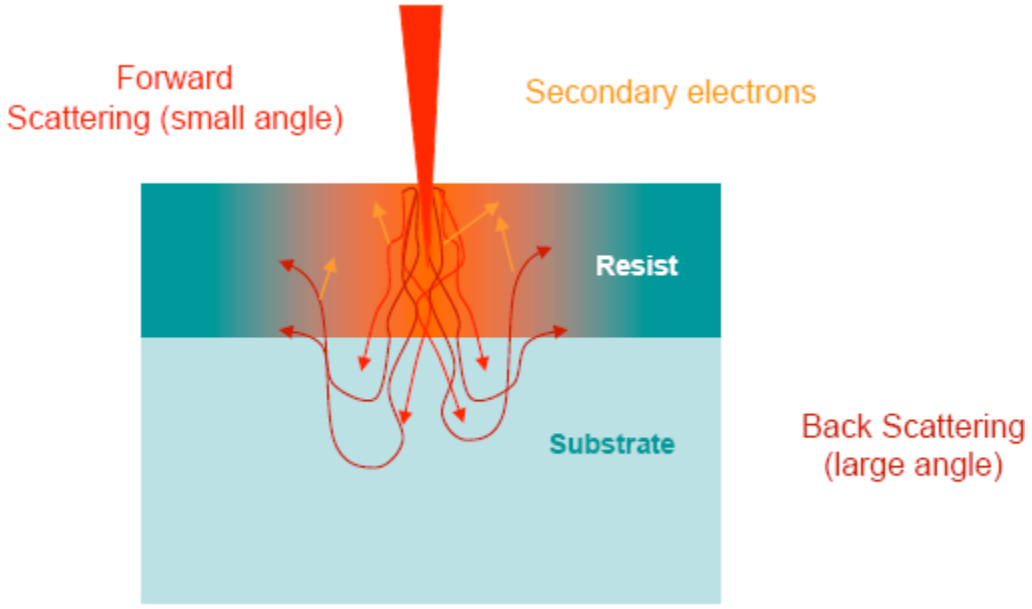

Figure 2.42: In EBL, resolution is controlled by electron scattering when the electron beam hits the surface. This is called the proximity effect.

EBL was performed with a Leica 100 EBL Nanowriter. The electron beam was produced by a field emission source and accelerated towards the sample using a voltage of 100 kV. The electron optics focus the beam to a tight spot of about 5-8 nm. A 4-inch

Si(100) wafer was used as a support for the sample. The wafer was coated with a 15-nm thin film of oxide (either SiO_2 or Al_2O_3). The thin film deposition was done by electron beam evaporation which leaves a non-stoichiometric oxide on the surface. To fill the oxygen vacancies within the oxide thin film, the oxide-coated wafers are oxidized in a tube furnace at 1073 K for 1hour. This process ensures thermodynamic stability. This wafer was first cleaned with isopropanol, acetone, and water. The electron-sensitive polymer resist used for the process is poly-methylmethacrylate or PMMA (M_w = 996 K). The chemical structure of PMMA is shown below in Figure 2.16, where n is ~10,000. A 2% (by mass) PMMA in chlorobenzene solution was prepared and spin-coated onto the wafer at 4000 rpm for 45 s. The resist layer was then baked at 348 K for a minimum of 12 hr. After the square-periodicity pattern was generated in the computer, the wafer was then exposed to the electron beam. Typical conditions include a beam current of 600 pA, a dose of 2500 $\mu C/cm^2$, and a dwell time of ~6 μs at each particle site. The polymer backbone is broken up when exposed to the electron beam, which makes the polymer more soluble in the developer solution. The developer solution consists of 3:1 (volume ratio) isopropanol:methyl isobutyl ketone. After the development of the PMMA, metal (platinum) was deposited directionally and with complete coverage with the same electron-beam evaporator (Veeco) used to deposit the oxide layer on the wafer. The electron-beam evaporation system is equipped with water-cooled crucibles with various metal and oxide sources, a tungsten filament for thermionic emission of electrons, a magnet to direct the electrons into the evaporation source, and a sample holder at the top of the bell jar chamber to hold the wafer. A shutter and a quartz crystal microbalance help to control the film thickness. The distance between the source and the sample is

approximately 1 m. For liftoff to occur reproducibly, the resist-undercut angle should be greater than the evaporation angle and the resist thickness should be about four times greater than the deposited metal thickness. Pt deposition was carried out at a pressure of 2×10^{-6} torr with a measured rate of ~1 Å/s. Care was taken to remain below the glass transition temperature of PMMA[35] (T_g = 120°C) during evaporation. After metal deposition, the sample was immersed in an acetone bath and ultrasonicated for five minutes to dissolve any residual polymer. This entire procedure left platinum nanoparticles on a thin film of alumina or silica supported on a Si(100) wafer.

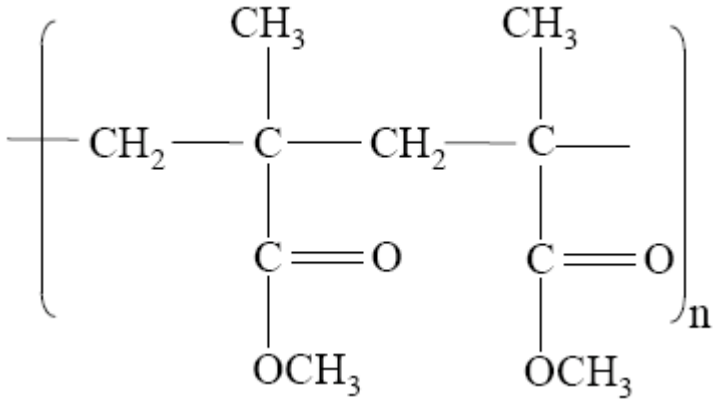

Figure 2.43: Chemical structure of poly-methylmethacrylate (PMMA). For a M_w=996K, n=~10,000.

While EBL, is capable of providing patterns with size resolution beyond that of conventional photolithography without use of a patterned mask, it is a relatively slow, serial process. So, the electron beam must actually be moved and expose the desired pattern across the surface one-by-one. This makes EBL extremely inefficient time-wise and undesirable for industrial patterning applications, which can be done with parallel lithography methods. Photolithography, for example, exposes a polymer resist in an area of about $1cm^2$ and repeat this procedure over an entire wafer in a couple of minutes.

2.2.2 Photolithography

Photolithography techniques have been used by the microelectronic industry to create reproducibly small features in the sub-micron size-regime for the last two decades[31,36]. Photolithography is a parallel process by which a planar substrate coated with a polymer resist is exposed to radiation through a patterned mask. In EBL, the electron beam exposed onto the polymer resists breaks up the polymer backbone and in this manner, creates a pattern to be developed. In the case of photolithography, the polymer resist is exposed to radiation, and a chemical reaction results from this exposure. As mentioned above, this exposure is through a patterned mask. Thus, the radiation-initiated chemical reaction is in certain areas of the resist. This pattern is then developed to expose the underlying substrate, and etching or material deposition through the pattern can be performed. The general scheme for photolithography is shown below in Figure 2.17a.

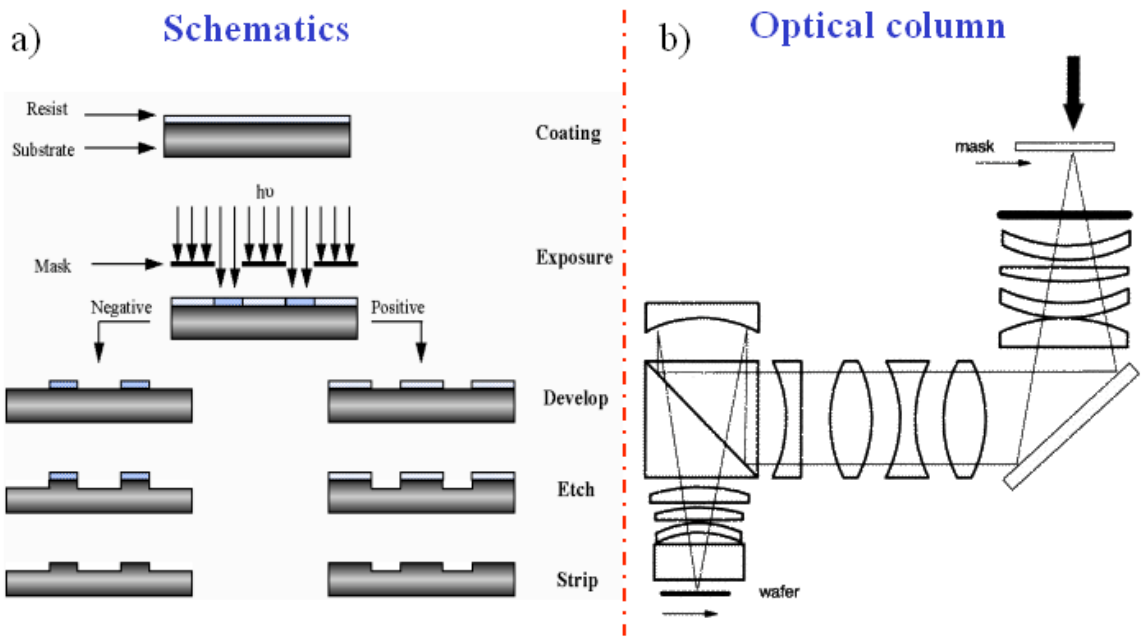

Figure 2.44: (a)General scheme for photolithography (b) optical column used to focus radiation on the photoresist surface for I-line photolithography

The fabrication sequence shown above is very much like that of EBL. For a positive resist, the radiation-exposed polymer is rendered more soluble in a developer solution. A negative photoresist would cross-link upon radiation exposure and become less soluble than the rest of the polymer surface, thus generating the negative of the radiation pattern. The radiation source can vary but all need to be focused through a series of lenses in an optical column before being sent through the mask and onto the polymer surface. Figure 2.17b is an example of an optical column for a wafer stepper used in I-line photolithography. The radiation source will determine the wavelength of the radiation. The ultimate feature size is dependent upon both the wavelength of the radiation source and the numerical aperture of the focusing element (Resolution = □/NA).

In this dissertation, photolithography is used as a starting point to create a mold for use in nanoimprint lithography (described in section 2.2.4). Two different radiation

sources have been used for fabrication. The first radiation source was the I-line of a mercury lamp (365 nm), and a KrF deep-UV (DUV) source (248 nm). While it would appear straightforward to use a smaller wavelength radiation source for achievement of smaller feature sizes, the polymer resist chemistry upon exposure must be taken into account as well. This is the main difference between the I-line and DUV photolithography and is described below.

2.2.2.1 I-Line versus Deep-Ultraviolet Photolithography Resist Chemistry

While the general steps in photolithography are not dependent on the radiation source (exposure, development, pattern transfer, resist removal), the chemistry occurring for pattern transfer is dependent upon this.

In I-line photolithography, 365 nm radiation from the I-line of a mercury discharge lamp is used as a source. There are three main components to the photoresist. The resin component gives the polymer film its structures. The most common resin is a durable polymer called novolac. The formation of this resin is shown below in Figure 2.18. The other component of the resist is the photoactive compound (PAC), which reacts with the radiation. A common PAC, diazo-quinone, is shown in Figure 2.19. The reaction that occurs upon radiation exposure is shown in Figure 2.20. The PAC, which inhibits solubility in basic solutions reacts with radiation to change to a carboxylic acid, which reacts favorably with a basic developer solution. The third component is the solvent that the resin and PAC are dissolved in, which controls the mechanical properties of the resist such as the viscosity of the base, keeping it in a liquid state. The time of exposure is key to the pattern transfer. If the exposure is not long enough, then the pattern will not develop fully (down to substrate), and if the exposure is too long, there

will be photoacid diffusion. This diffusion will give the feature a profile and can cause feature broadening.

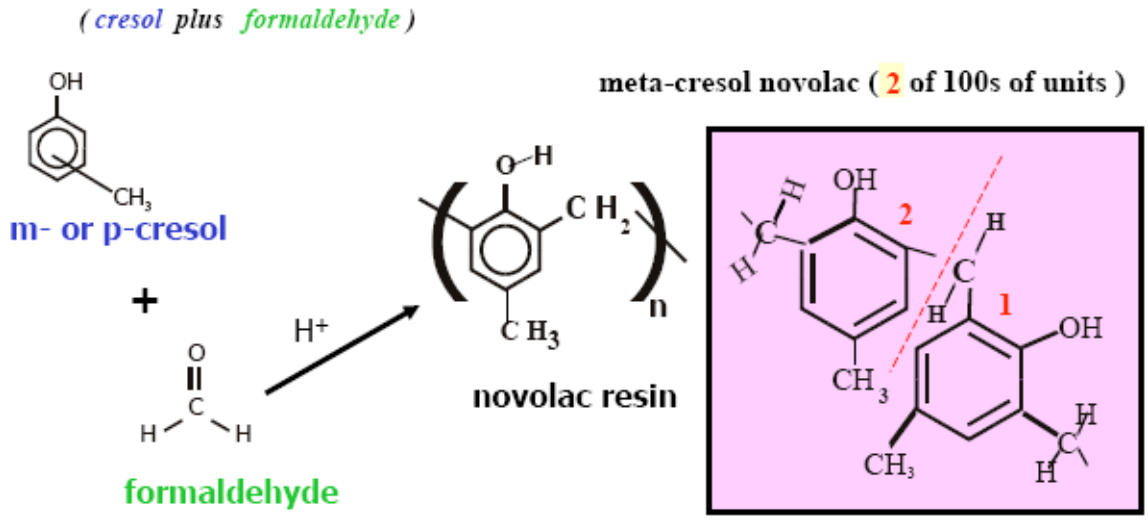

Figure 2.45: Formation of novolac resin, where n is equal to the number of monomeric sub-units in the polymer resin.

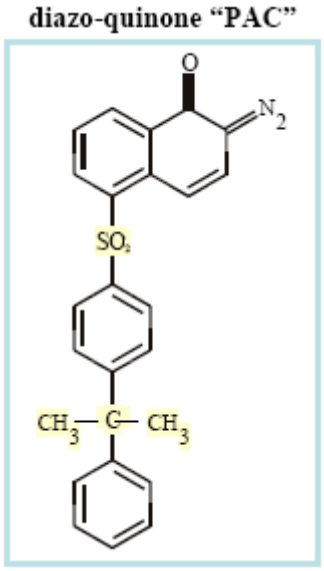

Figure 2.46: Diazo-quinone is a common photoactive component in positive photoresist.

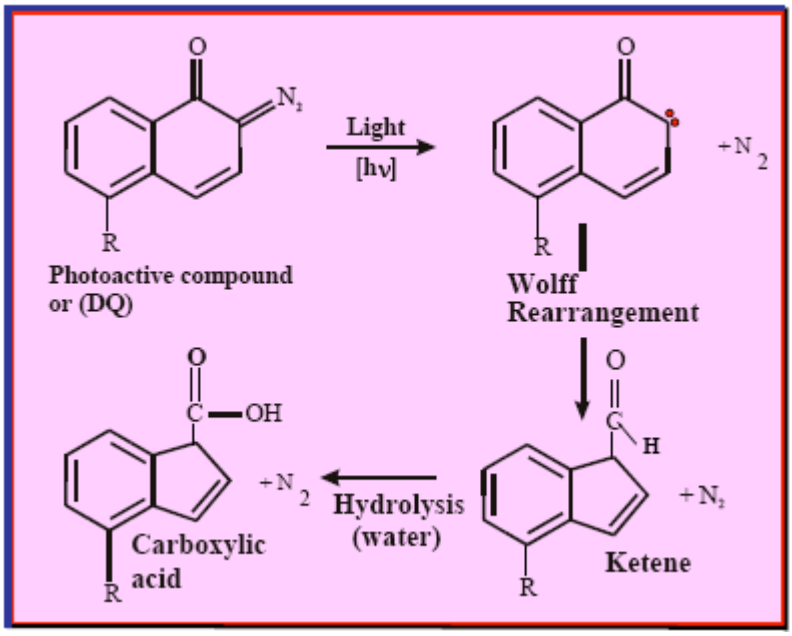

Figure 2.47: Photoreaction which occurs with the PAC diazo-quinone

While the above-explained I-line resist chemistry is very well known and widely used, the absorption of these resists for DUV-wavelength radiation is excessive and unbleachable, which makes them unsuitable for DUV lithography[37-39]. This absorption is due to the novolac resin. As well, the imaging mechanism used in I-line resists requires absorption of photons to release a useful product (photoacid), is not employable for DUV lithography due to the novolac resist's lack of sensitivity, which would make it impractical. Instead, DUV resists depend on a chemical amplification mechanism, where a photoabsorption event results in photoacid generation, and this acid-catalyzes several other reactions without being consumed[40-44]. This mechanism is shown below in Figure 2.21[Figure from reference 38]. High ultraviolet transparency is achieved by use of poly(4-hydroxystyrene) (PHOST) as the base polymer, which allows for aqueous base solubility. To render the polymer insoluble in base, and to achieve a chemically amplified polarity change, PHOST is protected with the addition of a t-

butoxy-carbonyl (t-boc) group onto the hydroxyl group of the PHOST creating the PBOCST shown below in Figure 2.21. Further development in resists is necessary as the wavelength of radiation steadily decreases to create smaller and smaller features.

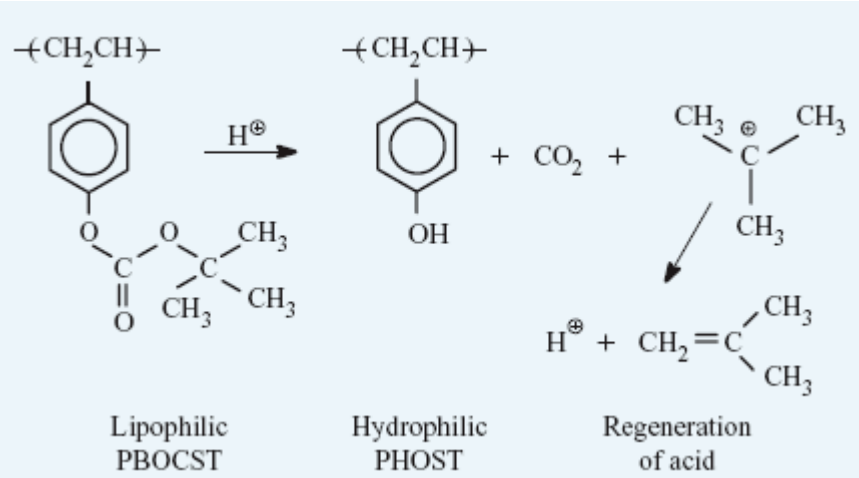

Figure 2.48: DUV resist chemical amplification mechanism

Both DUV and I-line photolithographies have been used to fabricate a mold of Si nanowires for the creation of 2-dimensional model catalysts, which have been used to study reactions (Chapters 4-7). However, it is clear that if photolithography is limited by the wavelength of light, then another method must be used to achieve feature sizes in the sub-100 nm regime. This method will be the focus of the next section.

2.2.3 Size Reduction Lithography

The pattern defined by photolithography is limited by the diffraction limits of light. Meaning, the wavelength of the radiation source used is usually the smallest that a feature size will be. For the purposes of our model catalytic studies, we wanted to be able to access the catalytically relevant size-regime (sub-100 nm). While photolithography provides us with a parallel fabrication method to achieve high surface

area of a controlled feature, I-line and DUV could not provide this size range. For this purpose, post-lithographic methods have been used to further reduce the printed feature size from photolithography and define sub-100 nm features.

The method created to achieve this ultimate goal of sub-100 nm features with regular periodicity across a full wafer-sized substrate was size-reduction lithography. A very similar method was used by Y.K. Choi *et al*. to successfully produce electronic devices in silicon with sub-40 nm structures starting from 600-nm structures produced by photolithography[45-47]. Their method, spacer lithography, produced higher quality features than those made by electron beam lithography. Using the techniques reported by Choi, the size reduction lithography (SRL) process was created and used to produce 20-nm wide single-crystal silicon nanowire arrays, starting from a wire structure with a diameter (linewidth) of 600 nm or 250 nm for I-line and DUV lithography exposures, respectively.

The first step in the SRL process is photolithographic patterning of photoresist and development of the photolithography pattern. This pattern can be transferred into the substrate below by an anisotropic plasma etch (Figures 2.21 and 2.22). The reduction of size of the feature takes place over several steps. If the patterned has been transferred into either the Si wafer or polycrystalline silicon (poly-Si), a conformal deposition of SiO_2 is used to coat the entire patterned surface. The sample is then anisotropically etched to expose the underlying pattern and to leave the deposited sidewall. The original poly-Si or Si pattern can then etched away selectively leaving only the deposited SiO_2 sidewalls. At this point the feature size has been reduced to the size of the sidewall deposition, and the pattern surface density has been doubled. The feature can then be

further etched down into the Si wafer and a mold of sub-100 nm Si nanowires will result. In this manner, sub-10 nm Si nanowires have been fabricated with average wire spacing of 900 nm. These Si nanowires will be used in conjunction with nanoimprint lithography to reproduce their structures out of a catalytically active metal. A schematic of the SRL process used in these studies is shown below. Figure 2.22 shows the photolithography process and transfer of pattern into the underlying substrate. Figure 2.23 shows the size-reduction process. The feature spacing and size is representative of this process carried out using I-line photolithography, and the images shown are representative results of carrying out these processes.

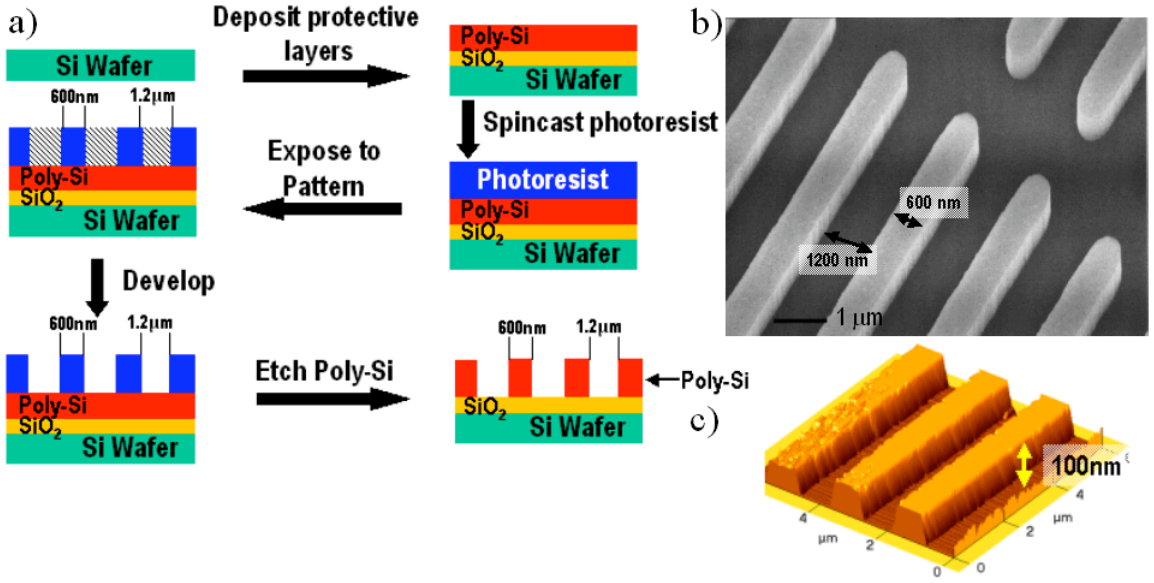

Figure 2.49: (a) Schematic of photolithography process pattern transfer to substrate (b) SEM image of polycrystalline silicon features on SiO_2 substrate, which is shown at last step of part (a). The features are 600 nm wide with 1200 nm spacing. (c) AFM image of polycrystalline silicon features showing that features have 100-nm height.

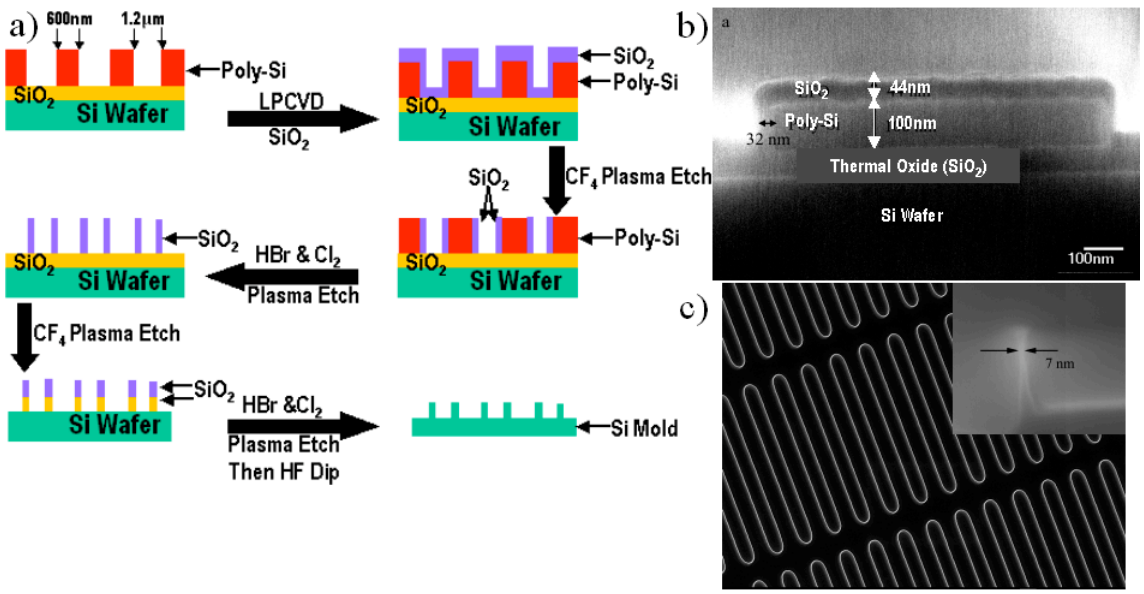

Figure 2.50: (a) Schematic of size-reduction process (b) Cross-sectional SEM characterization of the second step of the process in (a). (c) SEM characterization of the final step in (a). The inset shows the 7-nm final size of the nanowire which can be achieved.

Using SRL, 7□10^8 nanowires on a 4-inch Si(100) wafer were produced, which if reproduced out of metal, would allow for enough surface area to study of low turnover reactions. The SRL process has demonstrated the ability to produce sub-10 nm Si nanowires after used of oxidative trimming techniques (Figure 2.23 c)[48]. The specific process parameters used to produce the Si nanowire molds used in our studies are detailed in Chapters 4 and 5. Size-reduction lithography provides a sub-photolithographic method of pattern generation, which can be used for various applications. For the purpose of catalytic studies and applications, the pattern needs to be further transferred for change of materials from silicon to something catalytically active. For this purpose, a pattern transfer technique is employed.

2.2.4 Nanoimprint Lithography

Nanoimprint Lithography (NIL) is a technique, by which a pattern generated by other means can be transferred to another substrate with other materials. Shortly after Chou at Princeton invented this technique[49,50], extensive research was done to study the process, and the technique advanced very quickly[51-55]. In this case, the pattern generation has been carried out by use of photolithography and size-reduction lithography as described above. In order to transfer this pattern to another substrate and change the pattern from Si nanowires to Pt nanowires for use in catalysis studies, NIL is used.

In NIL two things are needed for pattern transfer. The first thing is a master mold, which has a pattern for duplication. The fabrication of this mold is described above in sections 2.2.3 and 2.2.4. The goal of this fabrication is a two-dimensional nanocatalyst array. Thus, the other thing needed is a substrate to support the catalyst array. For this support, a Si(100) wafer coated with an oxide thin film is used. A polymer coating is spincast upon the oxide thin film as a resist, and the mold and substrate are clipped together. The sample is then put into a hydraulic press which was built in our laboratory. It is then placed between two stainless steel plates that have been machined flat. The hydraulic press is equipped with a heating ring to heat the sample for imprint and a mechanical pump for evacuation of residual vapors during the imprint process. The hydraulic press assembly is shown schematically in Figure 2.24 and a picture of the actual press is shown in Figure 2.25. The sample is then heated above the glass transition temperature of the polymer and the mold is pressed into the resist on the substrate. They are pressed together at 4000 psi and since PMMA is the polymer resist

being used (M_w = 15k, Figure 2.16), an imprint temperature of 403 K is used. This pressure and temperature are held for 5 minutes. Then, the apparatus is cooled by flowing N_2 gas while maintaining the applied pressure. The sample is then removed from the press and the mold is separated from the imprinted resist. The negative of the mold pattern is left in the resist, and residual PMMA is left at the bottom of the imprinted features (Figure 2.27). This remaining PMMA is removed by anisotropically etching with O_2 plasma to expose the underlying oxide thin film. At this point, platinum is deposited by e-beam evaporation through the imprinted features and onto the substrate. A schematic of this process is shown below in Figure 2.26.

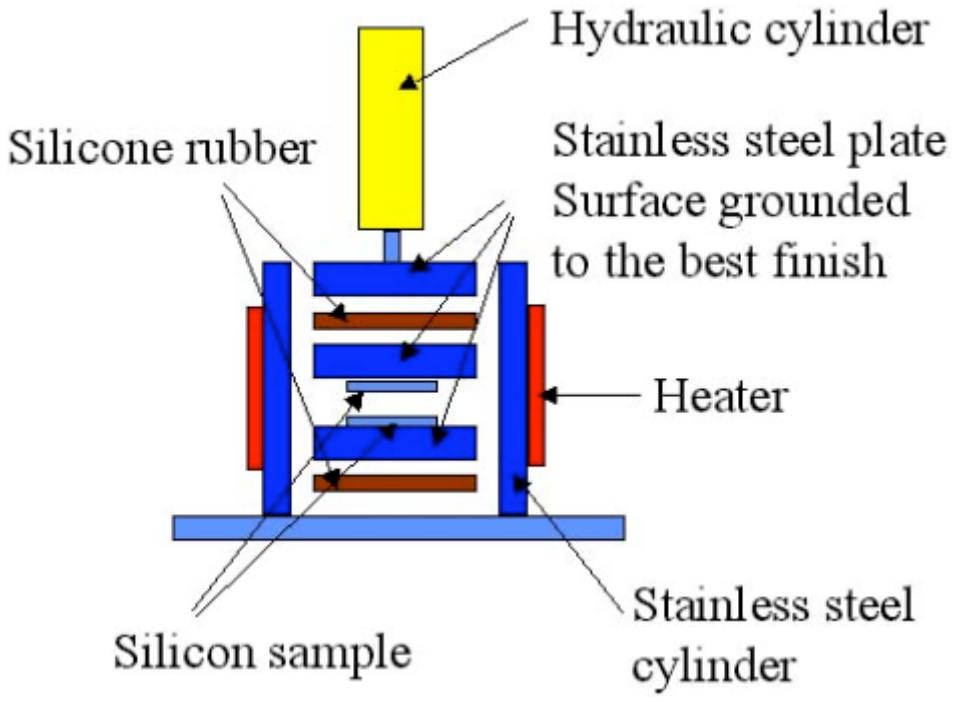

Figure 2.51: Schematic of the hydraulic press built for nanoimprint lithography

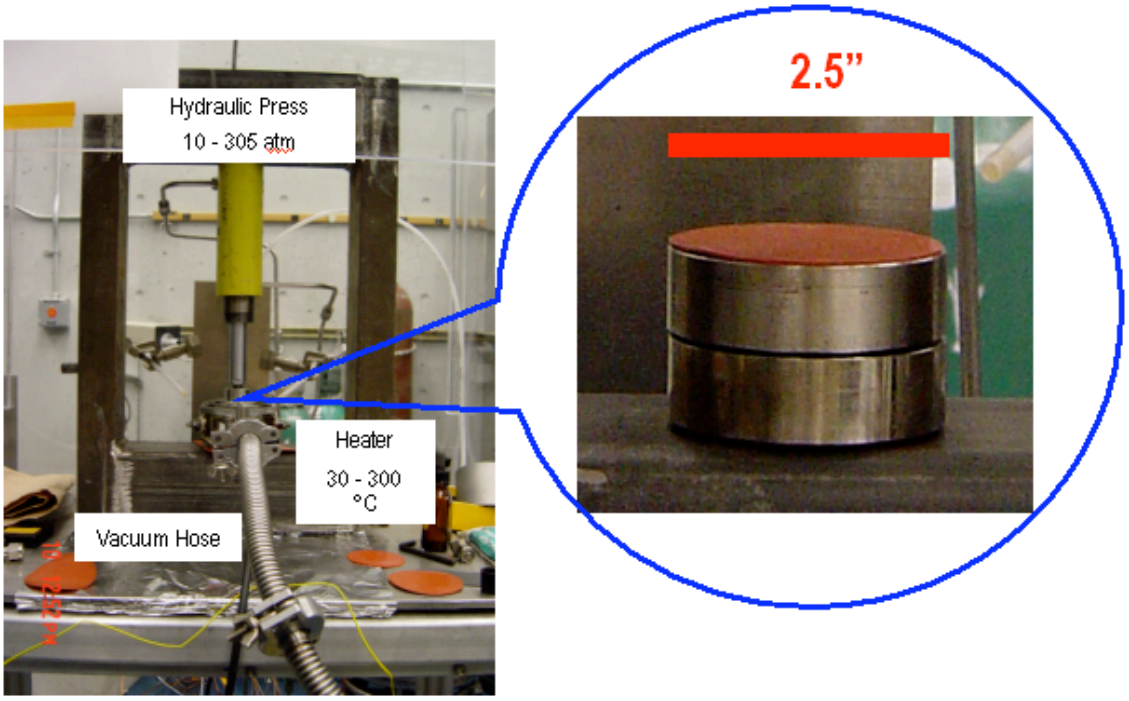

Figure 2.52: Picture of the hydraulic press used for nanoimprint lithography. Inset shows the two stainless steel plates used to compress the mold into the polymer resist.

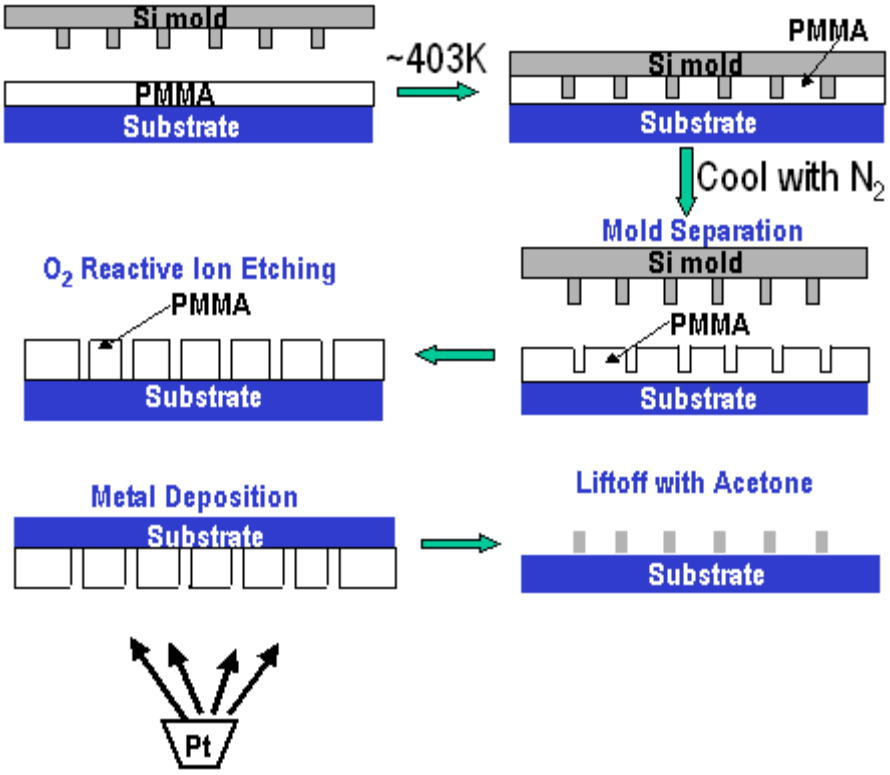

Figure 2.53: Nanoimprint lithography scheme used for fabrication of platinum nanowire samples.

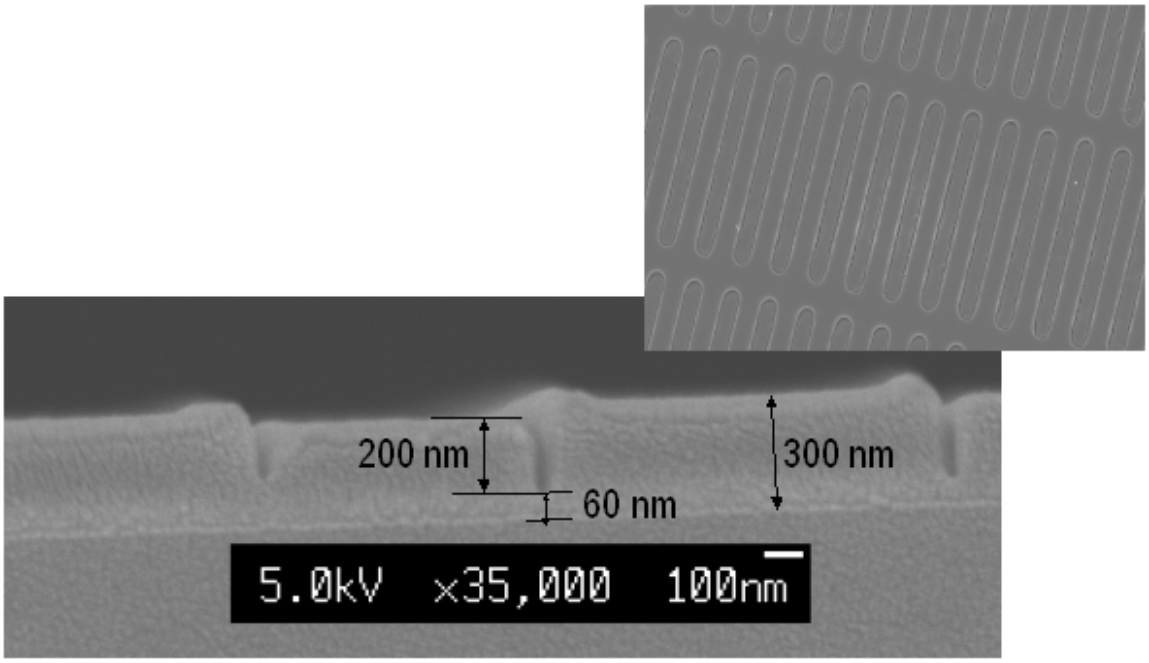

Figure 2.54: SEM characterization of PMMA resist layer after imprint with Si nanowire mold. The top-right picture shows a top-down view of the imprinted surface. The bottom left picture shows a cross-sectional view. The negative of the mold pattern has been produced in the resist layer and about 60 nm residual PMMA is still on the bottom of the imprinted features.

The NIL process has been used to successfully fabricate various samples of Pt nanowires on differing oxide supports. These samples have been used for catalytic reaction studies. The reaction studies and specific experimental details are given in Chapters 4 and 5.

2.3 Catalytic Reaction Measurement

Once the model catalysts have been fabricated by the techniques explained above, they are used to conduct reaction studies in heterogeneous catalysis. The reaction chamber used for these studies has been described in section 2.1.1. Reaction gases are introduced into the high-pressure cell and are circulated over the model catalyst by use of a recirculation pump (Metal Bellows). In order to measure the accumulation of products

a gas chromatography (GC) is part of the reaction loop and samples the reaction gases every five minutes by use of a six-port sampling valve.

2.3.1 Gas Chromatography

Gas chromatography[56,57] is a chemical separation technique, where an analyte gas is admitted into a tubular column and pushed through by a carrier gas (mobile phase). The stationary phase of the column, or the substance filling the column, is usually a non-volatile liquid coating the column walls like carbowax or a fine-solid support such as alumina or silica. The different chemicals within the sampled gas will have different affinities for the stationary phase material and will separate as they are pushed through the column by the mobile phase. The stationary phase of the column is chosen based on what chemicals are going to be separated. For instance, there are stationary phases that can separate compounds based on molecular weight and polarity. The columns are often very long between 10 and 50 meters. When the analyte arrives at the end of the column, it is passed through a detector, which measures a current based upon how much of the analyte is present. If the detector current is plotted versus time, a peak will be present for each chemical species separated on the column. He is constantly being pushed through the column. Thus, the baseline of the detector is established from the He signal. In these studies, two types of detectors are used, a flame-ionization detector (FID), and a thermal-conductivity detector (TCD). The FID detector is the more sensitive of the two detectors with the ability to detect as little as 2 picograms per second. Whereas, the TCD has a limit of detection of 400 picograms per milliliter of analyte passed through the detector. For FID, the gas leaving the column is burned in a mixture of air and hydrogen. Carbon

atoms produce CH radicals when burned in a hydrogen flame and produce ions as shown below.

$$CH + O \rightarrow CHO^{+} + e^{-}$$

These ions are produced at the anodic flame tip and are attracted to a biased cathodic collector where they are detected as an electrical current. About 1 in every 10^5 carbon atoms will produce an ion for detection. Carbonyls and carboxyl atoms are not capable of detection in this manner. Whereas FID is limited to carbon-containing compounds and is not able to be used for carbonyls, TCD is more universal. Thermal conductivity detection has the ability to detect any gas mixed with either He or H_2, which have the two highest thermal conductivities. Any gas mixed with He, then, will lower its thermal conductivity. The detector consists of a Pt-Re filament. A voltage is applied across this filament, which sends current through it and heats it up. This heating increases the resistance across the filament, which affects the potential measured across it. When no analyte is present, only He is measured coming over the filament and this can be used as a baseline. When gases coming off of the column (mixed with He) flow over the filament, the thermal conductivity decreases and the heat of the filament is not carried away as efficiently. This makes the filament heat up more and the resistance increases. This increase in resistance changes the potential measured across the filament. A reference He gas is sent through the detector as well, so that there is a constant baseline measured to compare against. This is accomplished by arranging the filaments in a wheatstone bridge, which is an electrical circuit used for precise comparison of resistances. In these studies, flame-ionzation detection was used to measure the gas phase products of reactions described in Chapters 3 and 4 (ethylene hydrogenation), and

thermal-conductivity detection was used for product measurement for the reaction studies described in Chapter 6 (CO oxidation).

References

1. A. Roth, *Vacuum Technology, 2nd Edition*, North-Holland, Amsterdam, 1982.
2. P.A. Redhead, J.P. Hobson, E.V. Kornelsen, *The Physical Basis of Ultrahigh Vacuum*, Chapman and Hall, London, 1968.
3. G.A. Somorjai, *Chemistry in Two-Dimensions: Surfaces*, Cornell University Press, Ithaca, New York, 1981.
4. G.A. Somorjai, *Introduction to Surface Chemistry and Catalysis*, John Wiley and Sons, New York, 1994.
5. M. Thompson, *Auger Electron Spectroscopy*, John Wiley and Sons, New York, 1985.
6. G. Ertl, J. Kuppers, *Low Energy Electrons and Surface Chemistry,* Verlag-Chemie, Germany, 1974).
7. R. Weissmann, K. Muller, *Surf. Sci. Rep.*, 105, **1981**, 251.
8. J.W. Niemantsverdriet, *Spectroscopy in Catalysis,* Wiley-VCH, Germany, 2000.
9. D.P. Woodruff, T.A. Delchar, *Modern techniques of surface science*, Cambridge University Press, Great Britain, 1986.
10. P.B. Needham, T.J. Driscoll, N.G. Rao, *Appl. Phys. Lett.,* 21, **1972**, 502.
11. J.F. Moulder, W.F. Stickle, P.E. Sobol, K.D. Bomben, *Handbook of X-Ray Photoelectron Spectroscopy*, Physical Electronics, Inc., Eden Prairie, MN, 1995.

12. D. Briggs, M.P. Seah, *Practical Surface Analysis: Auger and X-ray Photoelectron Spectroscopy*, John Wiley and Sons, New York, 1996.
13. B. Feuerbacher, B. Fitton, R.F. Willis, *Photoemission and the Electronic Properties of Surfaces*, John Wiley and Sons, New York, 1978.
14. A. Einstein, *Ann. Phys.*, Leipzig, 17, **1905**, 132.
15. G. Binnig, C.F. Quate, C. Gerber, *Phys. Rev. Lett.*, 56, **1986**, 930.
16. S. Dror, *Scanning force microscopy: with application to electric, magnetic and atomic forces,* Oxford University Press, New York, 1994.
17. S.F. Alvarado, *Surf. Rev. Lett.*, 5, **1995**, 607.
18. G. Binnig, H. Rohrer, *Helvetica Physica Acta*, 55, **1982**, 726.
19. G. Binnig, C.F. Quate, C. Gerber, *Appl. Phys. Lett.*, 40, **1982**, 178.
20. H.C. Hamaker, *Physica* 4, **1937**, 1058.
21. H. Hertz, *J. Reine Angew Math*, 92, **1881**, 156.
22. K.L Johnson, K. Kendall, A.D. Roberts, *Proc. R. Sco. Lond. A.*, 324, **1971**, 301.
23. B.V. Derjaguin, V.M. Muller, Y.P. Toporov, *J. Coll. Inter. Sci*., 67, **1975**, 314.
24. H. Stintzing, *DRP*, 481, **1927/29**, 155.
25. L. de Broglie, *Theses de doctorat*, Paris, Masson u. Co, **1924**.
26. H. Busch, *Ann. d. Phys.*, 81, **1926**, 974.
27. S.L. Flegler, J.W. Heckman, K.L. Klomparens, *Scanning and transmission electron microscopy: An introduction*, Oxford University Press, New York, 1993.
28. M.A. Hayat, *Principles and techniques of scanning electron microscopy*, Van Nostrand Reinhold, New York, 1974.

29. J.I. Goldstein, D.E. Newbury, P. Echlin, D.C. Joy, A.D. Romig, C.E. Lyman, C. Fiori, E. Lifshin, *Scanning electron miscroscopy and X-ray microanalysis: A text for biologists, materials scientists, and geologists*, Second edition, Plenum Press, New York, 1992.
30. K. Wetzig, *In situ Scanning Electron Microscopy in Materials Research*, Akadamie Verlag GmbH, Berlin, 1995.
31. S.A. Campbell, *The science and engineering of microelectronic fabrication*, Second edition, Oxford University Press, New York, 2001.
32. E. Chen, class notes, *Applied Physics 298r*, Harvard University, 2004.
33. Y. Nishi, R. Doering, *Handbook of semiconductor manufacturing technology*, Marcel Dekker, New York, 2000.
34. W. Chao, B.D. Harteneck, J.A. Liddle, E.H. Anderson, D.T. Attwood, *Nature*, 435, **2005**, 1210.
35. J. Brandrup, E.H. Immergut, E.A. Grulke, eds. *Polymer Handbook.* John Wiley & Sons, New York, 1989.
36. M.J. Madou, *Fundamentals of Microfabrication: The Science of Miniaturization, Second Edition*, CRC Press, New York, 2002.
37. P.B. Sahoo, R. Vyas, M. Wadhwa, S. Verma, *Bull. Mat. Sci.*, 6, **2002**, 553.
38. H. Ito, *IBM J. Res. & Dev.*, 5, **2001**, 683.
39. H. Ito, *SPIE*, 3678, **1999**, 2.
40. H. Ito, *Solid State Technol.*, 36, **1996**, 164.
41. H. Ito, *IBM J. Res & Dev.*, 41, **1997**, 69.

42. H. Ito, C.G. Willson, J.M.J. Frechet, *Digest of Technical Papers of 1982 Symposium on VLSI Technology*, **1982**, 86.

43. H. Ito, C.G. Willson, *Technical Papers of SPE Regional Technical Conference on Photopolymers*, **1982,** 86.

44. H. Ito, C.G. Willson, *ACS Symposium Series 242 "Polymers in Electronics"*, ACS, Washington D.C., 1984, 11.

45. Y.K. Choi, T.J. King, C. Hu, *IEEE Trans. Electron Devices*, 49, **2002**, 436.

46. Y.K. Choi, T.J. King, C. Hu, *IEEE Electron Device Lett*., 23, **2002**, 25.

47. Y.K. Choi, T.J. King, C. Hu, *Solid State Electronics*, 46, **2002**, 1595.

48. Y.K. Choi, J. Zhu, J. Grunes, J. Bokor, G.A. Somorjai, *J. Phys. Chem. B*, 15, **2003**, 3340.

49. S.Y. Chou, P.R. Krauss, P.J. Renstrom, *Appl. Phys. Lett*., 67, **1995**, 3114.

50. S.Y. Chou, P.R. Krauss, P.J. Renstrom, *Science*, 272, **1996**, 85.

51. W. Wu, B. Cui, X.-Y. Sun, W. Zhang, L. Zhuang, L. Kong, S.Y. Chou, *J. Vac. Sci. Technol. B*, 16, **1998**, 3825.

52. S.Y. Chou, P.R. Krauss, P.J. Renstrom, *J. Vac. Sci. Technol. B*, 14, **1996**, 4129.

53. S. Zankovych, T. Hoffmann, J. Seekamp, J.-U. Bruch, C.M. Sotomayor Torres, *Nanotechnology*, 12, **2001**, 91.

54. C. Marrian, S.Y. Chou, eds. *Proc. First International Conference on Nanoimprint Nanoprint Technology*, San Francisco, California, 2002.

55. C. Marrian, S.Y. Chou, eds. *Proc. Second International Conference on Nanoimprint Nanoprint Technology*, Boston, Massachusetts, 2003.

56. D.C. Harris, *Quantitative Chemical Analysis, Fifth Edition*, W.H. Freeman and Company, New York, 1999.

57. www. Agilent.com, *Gas Chromatograph HP 5890 Series II: Owner's Manual*

Chapter 3

Fabrication of 2-Dimensional Platinum Nanoparticle Arrays by Electron Beam Lithography: Ethylene Hydrogenation and CO-Poisoning Reaction Studies

3.1 Abstract

Electron beam lithography (EBL) has been used to fabricate platinum nanoparticle arrays in the 20-nm size range on oxide thin films of silica and alumina deposited onto silicon wafers. A combination of characterization techniques (SEM, AFM, XPS, AES) has been used to determine size, spatial arrangement and cleanliness of these fabricated catalysts. Ethylene hydrogenation reaction studies have been carried out over these platinum nanoarrays and have revealed major differences in turnover rates and activation energies of the different nanostructures when clean and when poisoned with carbon monoxide. The oxide-metal interfaces are implicated as important reaction sites that remain active when the metal sites are poisoned by adsorbed carbon monoxide.

3.2 Introduction

Nanoscience, over the past decade, has come to the forefront of technology in many areas of research [1-4]. The reproducible manipulation of matter in the sub-100 nm size regime all the way down to the atomic scale has been proven possible and is being used to explore the size effects of many new systems and materials [5,6]. Employing this new technology to solve problems in catalysis is essential to unlocking some of the key ingredients to catalytic activity and selectivity. Many industrial platinum catalysts are nanoparticles that are dispersed on high surface area porous oxide supports. The resistance of these industrial catalysts to poisoning under industrial conditions has been the focus of much research, and it has been postulated that this may be due to the presence of an oxide-metal interface. Industrial catalysts, however, are very complex systems that need to be studied piece by piece in order to make progress towards understanding their inner workings. Traditionally, metal single crystals have been used as model catalysts in combined surface science and catalytic reaction studies[7-22]. They have revealed the surface structure sensitivity or insensitivity of different catalytic reactions, the roles of surface defects such as steps and kinks, and additives that are bonding or structure modifiers. Single crystals provide a wealth of information about adsorbate bonding to different crystal faces and catalytic reaction mechanisms but are unable to successfully model reactivity intrinsic to industrial catalysts that involve the oxide-metal interface or the oxide surface. There has been considerable effort to create a model catalytic system with an oxide-metal interface that can be tuned precisely in the nanometer size range. With precise control of the fabrication of a catalyst comes the ability to systematically vary different parameters of the metal structure such as size and

spacing as well as a choice of the oxide-metal interface of the catalyst. Control of these parameters in the nanoscale regime is difficult to obtain, but lithography lends itself nicely to this task. The use of electron beam lithography (EBL) to construct platinum nanoparticle arrays on oxide surfaces as new model platinum catalysts has been explored[23,24]. About 10^9 nanoparticles can be produced using this technique in a 6 mm × 6 mm array on a 1-cm^2 silicon wafer in about a day. This corresponds to a platinum surface area of about 0.1 cm^2. However, the study of low turnover reactions ($<10^{-4}$ s^{-1}) requires ~1 cm^2 of platinum surface area for practical detection of reaction products. Because of the sequential nature of electron beam exposure, the production of ~1 cm^2 of exposed platinum surface area would require approximately 10 days to fabricate, which is not practical. While the EBL-fabricated platinum samples can be used to study high turnover reactions (such as ethylene hydrogenation) or the thermal and chemical stability of the platinum nanoparticles [25], the small metal surface area somewhat limits the number of reactions that can be studied on these catalysts.

This chapter describes the production of platinum nanoparticle arrays fabricated by EBL. These platinum nanoarrays have been used as model catalysts to carry out ethylene hydrogenation with and without the presence of carbon monoxide. Surprisingly large differences in turnover rates and activation energies were found for these model catalyst systems even for this structure insensitive reaction.

3.3 Experimental

3.3.1 Characterization

The Pt nanoarrays were characterized by scanning electron microscopy (SEM), atomic force microscopy (AFM), and x-ray photoelectron spectroscopy (XPS). SEM images are taken with a JEOL JSM-6340F equipped with a cold field emission source operating between 3 kV and 20 kV with a probe current of 12 □A. All SEM images are acquired using an E-T combined backscatter and secondary electron detector at a working distance of 6 mm. A typical SEM image of the samples is shown in Figure 3.1c. AFM is used to determine the height and to verify the periodicity of the arrays. AFM images of the nanoparticle arrays are taken on a Park Scientific Instruments, M5 AFM. The AFM uses a feedback loop between a scan piezo and a position-sensitive photodiode array at a constant force to monitor the reflected laser light from the backside of the cantilever. A typical AFM image of the samples is shown in Figure 3.1b. XPS spectra are taken to analyze the chemical composition of the surface after fabrication. Spectra are taken on a 15-kV, 40-Watt PHI 5400 ESCA/XPS system equipped with a Mg anode x-ray source. Samples are cleaned of any foreign particulates before being analyzed with a stream of nitrogen gas. The spectra are inspected for the Pt $4f_{7/2}$ and $4f_{5/2}$ peaks to verify that platinum had been deposited. As well, the spectra verify the presence of the characteristic Si and Al peaks for each of the oxide substrates.

3.3.2 Pt nanoparticle arrays on alumina and silica: fabrication by EBL

The EBL fabrication process of platinum nanoparticle arrays has been reported elsewhere[23,24], and the general scheme is shown in Figure 3.1a. Briefly, a thin layer of electron sensitive polymer resist is spincast onto a Si(100) wafer coated with a 15-nm

thick film of either alumina (Al_2O_3) or silica (SiO_2). The photoresist used was poly-methyl methacrylate (PMMA) with M_w=950 k. The resist is exposed to a highly collimated electron beam (Leica Nanowriter) in a computer-generated dot-like pattern across the polymer surface. The electron beam is generated by a field emission source that exposed the polymer with a beam current of 600 pA and an accelerating voltage of 100 kV giving the beam a diameter of between 5 and 8 nm. Upon exposure to the electron beam, the polymer undergoes bond scission, which renders it more soluble in a developer solution. After developing the pattern, 15 nm of Pt is vacuum deposited onto the exposed underlying oxide substrate by means of electron beam evaporation using a quartz crystal microbalance thickness monitor. Liftoff of the remaining polymer is achieved by ultrasonication in acetone for five minutes, leaving an array of Pt nanoparticles on the surface. Atomic force microscope (AFM) and scanning electron microscope (SEM) images of the platinum arrays on an alumina substrate are shown in Figures 3.1b and 3.1c, respectively. SEM measurements show the diameter of the Pt particles on both alumina and silica to be 28 ± 2 nm and the periodicity to be 100 ± 1 nm. The area of the EBL arrays both on alumina and silica are 36 mm^2 equivalent to 3.6 □ 10^9 Pt particles. AFM measurements verify the height of the nanoparticles to be 15 ± 1 nm.

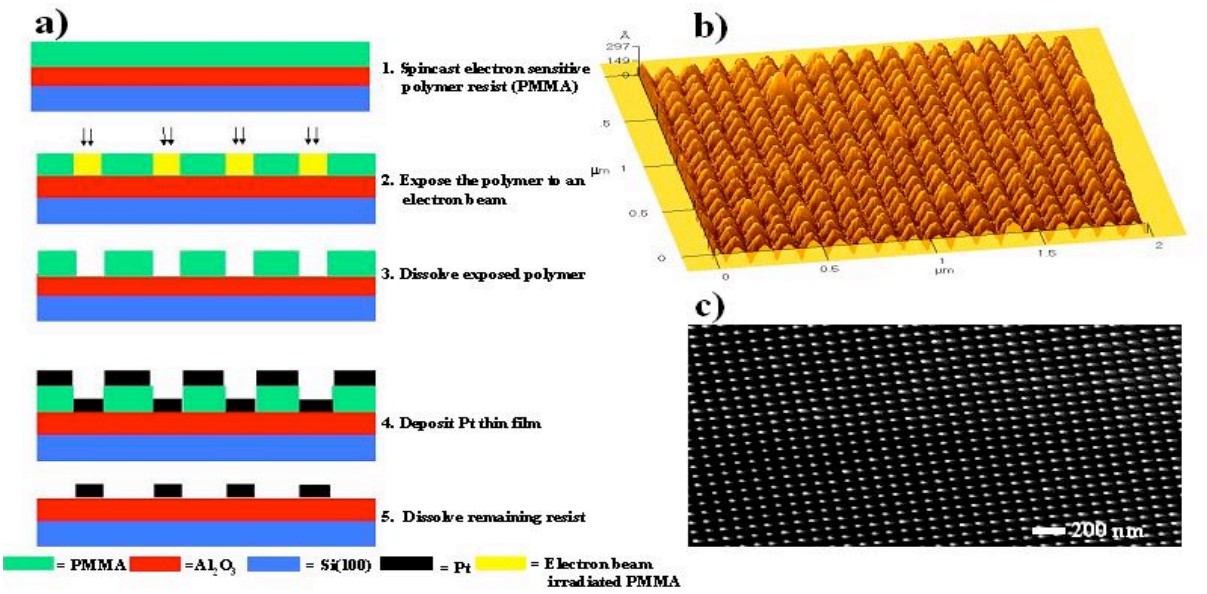

Figure 3.55: a) EBL fabrication scheme b) Atomic force microscopy image of Pt nanoparticle array showing Pt particle height of 15 nm c) Scanning electron microscopy image of Pt nanoparticle array showing particle diameters of 28 nm and particle spacing of 100 nm.

3.3.3 Reaction Apparatus

The reaction studies are carried out in an ultrahigh vacuum (UHV) chamber equipped with a high-pressure reaction cell, which was described in Chapter 2. The general design of this type of chamber has been described elsewhere[26,27]. The outer chamber achieves a working pressure of 1×10^{-9} Torr between reactions. The chamber was evacuated by use of a turbomolecular pump (Balzers TPU 330), and an ion pump (Varian). All of the nanocatalyst arrays are cleaned by dosing with 1×10^{-6} Torr of NO_2 at 573 K for 20 minutes, followed by dosing the sample with 10 L of CO and flashing the temperature to 573 K to remove the remaining CO from the surface. This procedure has been established to be effective for cleaning supported Pt nanostructures and Pt(111) single crystals of their major surface impurities such as carbon and oxygen [28]. This cleaning procedure is used before the start of every experiment. Sample mounting

procedures have been detailed elsewhere[28,29]. Auger electron spectroscopy (AES) is used to monitor the surface cleanliness of the sample. All Auger spectra are taken using a Physical Electronics Industries, Inc. Auger system. As the Auger process itself can deposit carbon impurities on the surface of the sample, the sample is always cleaned after any Auger spectra are taken. A schematic of the UHV reaction system is shown in Figure 3.2.

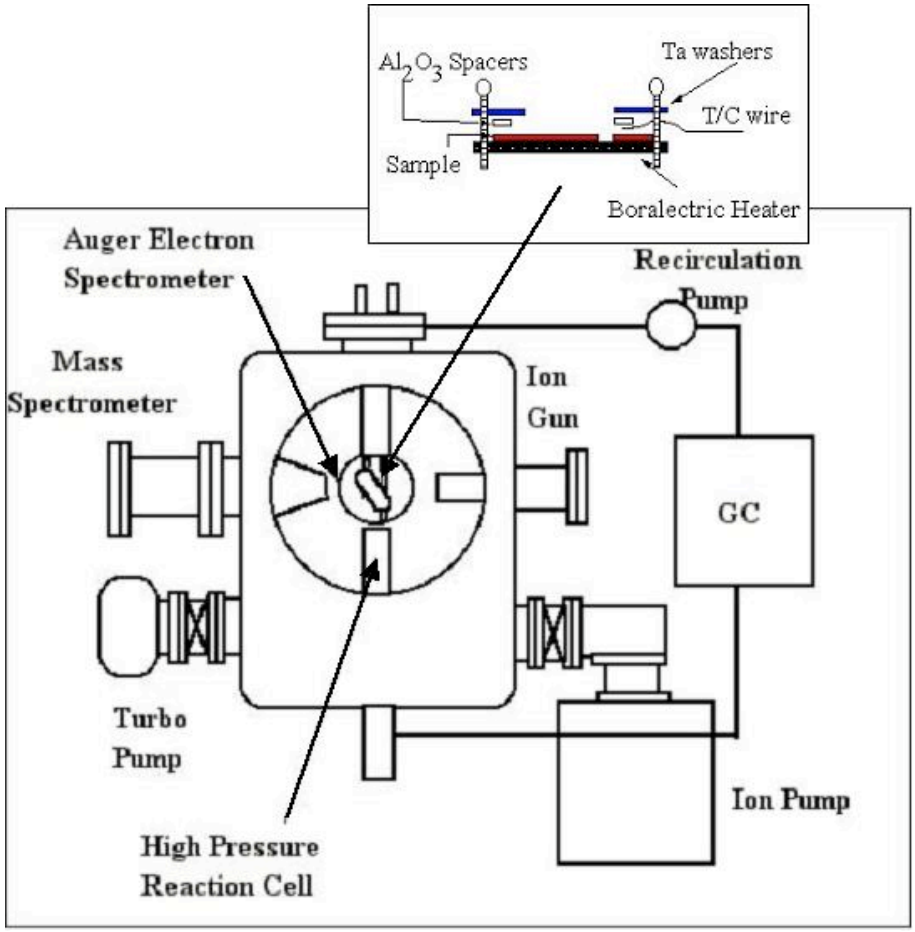

Figure 3.56: Schematic of UHV reaction system. Inset shows the sample mount used for reactions.

3.3.4 Reaction Studies

Every sample is cleaned as described above before introducing reaction gases. Catalytic studies are carried out on all catalyst samples using 10 Torr C_2H_4, 100 Torr H_2,

and 650 Torr Ne gas. For CO poisoning studies, 300 mTorr of CO is added to the manifold with the reaction gases. Gases are premixed in the gas manifold approximately 20 minutes before introduction to the catalyst and the reaction line. The gases are circulated through the reaction line with a Metal Bellows re-circulation pump. A HP Series II gas chromatograph equipped with a FID detector and a 50-m alumina capillary column (J&W Scientific) was used to separate and analyze products. The GC was part of the reaction loop and sampled the circulating reaction gases every 2.5 minutes using an automatic sampling valve. The H_2, C_2H_4, Ne, and CO had gas purities of 99.99%, 99.5%, 99.999%, and 99.3%, respectively. All reaction turnover rates are reported in units of s^{-1}, for brevity, but are defined as the number of reactant molecules reacting per Pt surface atom per second (molecule/ site/ second).

3.4 Results

3.4.1 Reaction Studies

The ethylene hydrogenation reaction studies over the nanoparticle catalyst arrays were carried out in the 313 – 413 K temperature range without the presence of CO and in the 393 – 473 K temperature range with the presence of CO. This is a structure insensitive reaction on platinum catalysts, meaning that in most cases the turnover rate will be the same for different platinum catalysts reacting under similar conditions. A summary of the measured activation energies and turnover rates at 300 K is shown below in Table 3.1 for both of the nanoparticle arrays. A typical ethane accumulation curve is shown in Figure 3.3. Due to the small metal surface area of the catalyst samples, ethane accumulation is slow at room temperature. Therefore, all reported turnover rates have

been extrapolated from the Arrhenius plots to recover the turnover rates at 300 K. The reactions on the fabricated catalysts are compared to the reaction studies on Pt(111) single crystal by Zaera *et. al.*[30] and Hwang *et. al.*[31]. The single crystal data shows a turnover rate of 10 s^{-1} and an activation energy of 10.8 ± 0.1 kcal/mol with no CO poisoning. Upon CO poisoning, the turnover rate decreases sharply to 4.8 □ 10^{-6} s^{-1} and there is a corresponding increase in the activation energy to 20.2 ± 0.1 kcal/mol. The turnover rate of for the Pt(111) single crystal was calculated using the empirical rate equation of Zaera *et. al.*[30] The turnover rate for the CO poisoning of the single crystal was extrapolated from the Arrhenius plot in ref. 31.

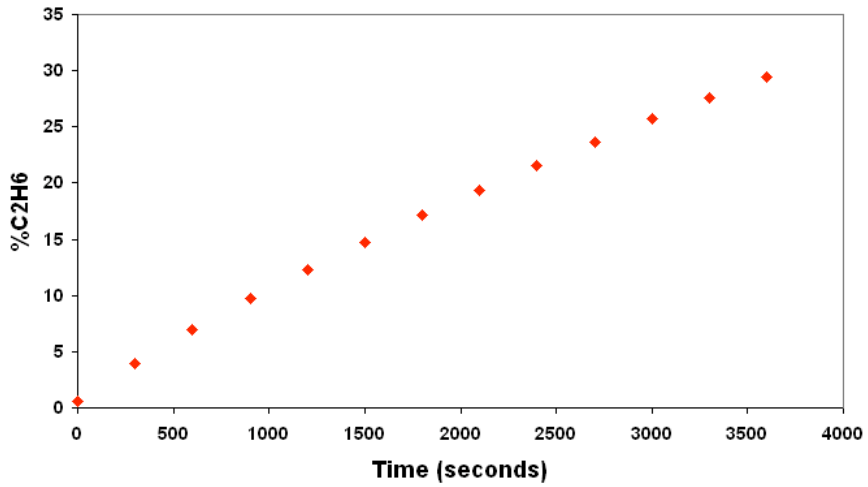

Figure 57.3: Typical ethane accumulation curve used to calculate turnover rates. This data was obtained at 353K using a Pt nanoparticle catalyst on a silica support.

Table 3.1: Summary of reaction studies.

Catalyst Sample	Unpoisoned E_a (kcal/mol)	CO Poisoned E_a (kcal/mol)	Unpoisoned Turnover Frequency @300K (s^{-1})	Poisoned Turnover Frequency @300K (s^{-1})
Pt (111)[31,32]	10.8 ± 0.1	20.2 ± 0.1	10	4.8 □ 10^{-6}
28-nm Pt nanoparticles on alumina support	10.2 ± 0.2	11.4 ± 0.5	7.3	0.071
28-nm Pt nanoparticles on silica support	11.3 ± 0.1	15.6 ± 0.4	5.3	0.041

The Pt nanoparticle arrays, both on silica and alumina, show similar behavior for the unpoisoned ethylene hydrogenation studies. However, the CO-poisoned reaction studies have dramatically different behavior than the Pt(111) single crystal. Unpoisoned ethylene hydrogenation studies on the silica and alumina supported catalysts show apparent activation energies of 11.3 ± 0.1 kcal/mol and 10.2 ± 0.2 kcal/mol and turnover rates of 5.3 s^{-1} and 7.3 s^{-1}, respectively. As mentioned above, these numbers are similar to those seen for the Pt(111) single crystal. The activation energies are almost identical to that of Pt(111), and the turnover rates are close to the accepted value of ~10 s^{-1}. The CO poisoning studies show that the nanoparticle arrays have a lower energy of activation than seen with CO-poisoned Pt(111). The silica and alumina supported arrays show apparent activation energies of 15.6 ± 0.4 kcal/mol and 11.4 ± 0.5 kcal/mol, and turnover rates of 0.041 s^{-1} and 0.071 s^{-1}, respectively. The activation energies are significantly lower than that measured on CO-poisoned Pt(111), and the turnover rates are four orders of magnitude higher than that seen for the single crystal. The Arrhenius plots for these two samples are shown below (Figures 3.4a,b).

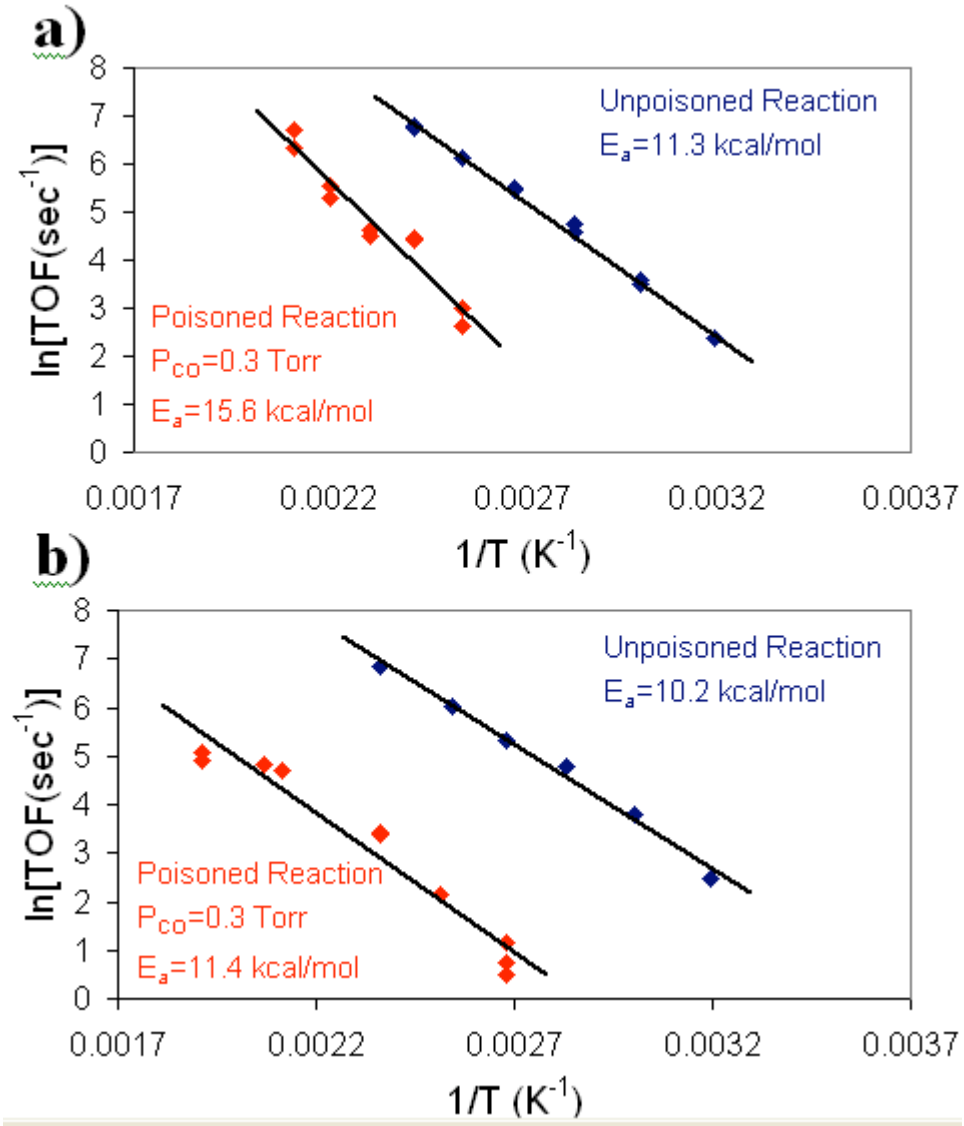

Figure 3.58: Arrhenius plots for ethylene hydrogenation reactions on Pt nanoparticle arrays supported on a) silica and b) alumina.

3.5 Discussion

Table 3.1 summarizes the turnover rates and activation energies for ethylene hydrogenation on the platinum nanoparticles deposited on silica and alumina with and without CO poisoning. These results are also compared with similar data obtained on the (111) crystal face of platinum, which may be used as a reference state of a platinum

catalyst without the presence of an oxide support. In order to calculate the turnover rates for each of the fabricated catalyst arrays, the metal surface area was calculated using geometrical considerations. The nanoparticle geometry was considered to be that of a cylinder standing on a planar oxide support with a diameter of 28 nm and a height of 15 nm (Figure 3.5). The platinum and oxide surface areas that result from these calculations are shown below in Table 3.2. Without the presence of oxide, the clean Pt(111) surface has a turnover rate of about 10 s^{-1} at 300 K and an activation energy of about 11 kcal/mol. The oxide-supported platinum nanoparticles have very similar turnover rates and activation energies for this reaction.

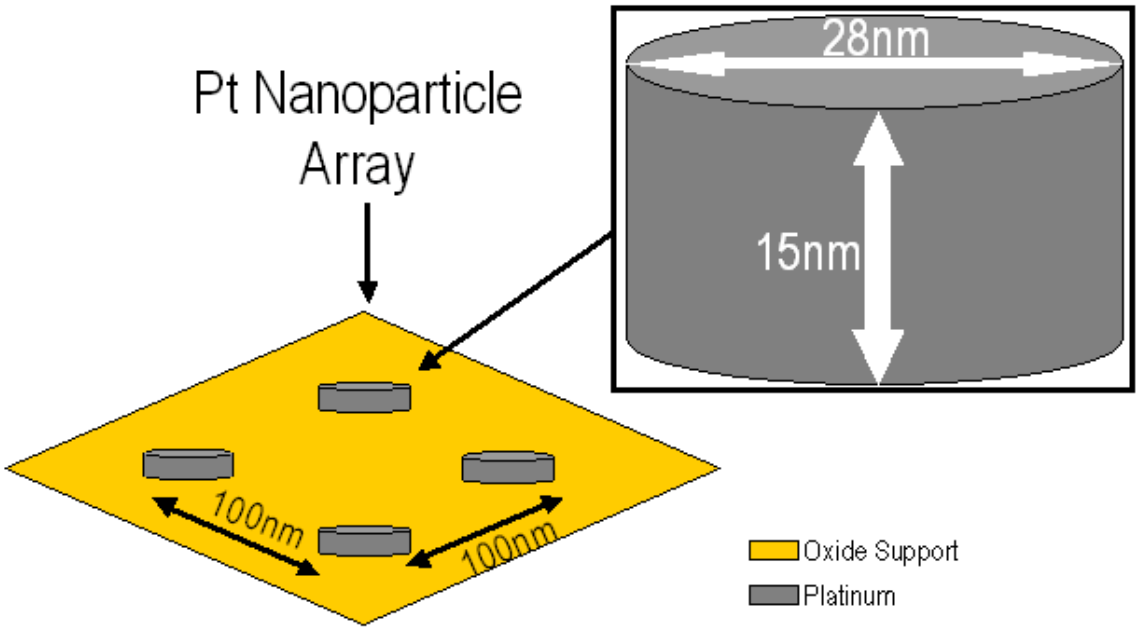

Figure 3.59: Schematic of Pt nanoparticle array showing the geometry used to calculate the number of surface platinum sites available for reaction.

Table 3.2: Comparison of catalyst metal and oxide surface areas.

Catalyst Sample	Total Pt Surface Area (cm^2)	Oxide Surface Area (cm^2)	Ratio of Oxide to Metal Surface Area
28-nm Pt nanoparticles on alumina support	0.070 ± 0.006	0.34 ± 0.01	4.9 ± 0.4
28-nm Pt nanoparticles on silica support	0.070 ± 0.006	0.34 ± 0.01	4.9 ± 0.4

Major differences in catalytic behavior emerge, however, when the platinum catalysts are poisoned by adsorbed carbon monoxide. CO binds strongly to platinum and thus adsorbs preferentially to other gases in the reaction mixture like ethylene. Before a reaction can occur, a CO molecule must desorb from the metal surface. CO also restricts the mobility of the adsorbed reactant molecules[22], therefore lowering the probability of a reaction occurring. For Pt(111), CO poisoning of the reaction increases the activation energy to 20 kcal/mol, and decreases the turnover rate at 300 K by seven orders of magnitude, to approximately 10^{-6} s^{-1}.

Upon CO adsorption, the platinum nanoparticle arrays show dramatically different behavior than the Pt(111) single crystal. The CO-poisoned activation energies for ethylene hydrogenation on the alumina and silica supported samples are 11.4 kcal/mol and 15.6 kcal/mol, respectively. These are much lower than for the Pt single crystal. The turnover rates are in the range of ~5□10^{-2} s^{-1}, which is orders of magnitude greater than for the single crystal surface. It appears that on these platinum nanoparticle arrays deposited on the oxides (SiO_2 or Al_2O_3), there are reaction sites that do not deactivate for ethylene hydrogenation in the presence of coadsorbed carbon monoxide. These sites may be at the oxide-metal interfaces. An attempt was made to correlate the Pt-oxide interface sites to the turnover seen during CO-poisoning of the reaction by calculating the turnover

rates and considering them to be a consequence of either the total amount of Pt on the surface of the nanoparticle or of just the oxide-Pt interface sites on the surface. The number of interface sites on each particle was calculated geometrically by first calculating the circumference of a Pt nanoparticle with 28-nm diameter and then dividing it by the diameter of a Pt atom (2.77 Å). The oxide-metal interface was considered to be one Pt atom high. The results of these calculations are shown in Table 3.3. The unpoisoned turnover frequencies for the Pt nanoparticle samples on Al_2O_3 and SiO_2 are 7.3 s^{-1} and 5.3 s^{-1}, respectively. If the same amount of platinum is taken into consideration (i.e. the platinum surface area of the entire particle), then the CO-poisoned turnover frequencies for the Al_2O_3 and SiO_2 supported samples are 0.071s^{-1} and 0.041s^{-1}, respectively. However, if the interface sites are considered to be the only active sites for reaction during CO poisoning, and the turnover frequency is calculated from just these sites alone, then the Al_2O_3 and SiO_2 supported samples have turnover frequencies of 7.1 s^{-1} and 4.2 s^{-1}, respectively. These turnover frequencies are almost identical to those of the unpoisoned samples. In the SiO_2-supported sample, the activation energy increases from 11.3 kcal/mol to 15.6 kcal/mol upon CO-poisoning. If the reaction is proceeding fully at the oxide-metal interface, and the catalytically active sites are similar before and after addition of CO to the reaction mixture, then the activation energy should not be significantly higher. However, a significant increase in activation energy is measured, which is indicative of a change in the catalytically active sites and the rate-determining step of the reaction. At present, there is no information on how the active sites change upon CO-poisoning. While not conclusive, these results do lend credence to the idea of oxide-metal interface sites remaining active under poisoning conditions. Varying the

EBL platinum particle size and determining if the CO-poisoned turnover frequency scales accordingly can perhaps elucidate this idea further.

Table 3.3: Comparison of turnover frequencies between the two EBL-fabricated catalyst samples. a) Unpoisoned turnover frequencies. b) CO-poisoned turnover frequencies calculated assuming all Pt surface sites are active. c) CO-poisoned turnover frequencies assuming only oxide-Pt interface sites are active. Pt surface sites and oxide-Pt interface sites were determined by geometrical considerations.

Catalyst Sample	**Turnover Frequency @300K (s^{-1})**	**b) CO-Poisoned Turnover Frequency @300K (s^{-1})**	**c) CO-Poisoned Turnover Frequency @300K (s^{-1})**
28-nm Pt nanoparticles on alumina support	7.3	0.071	7.1
28-nm Pt nanoparticles on silica support	5.3	0.041	4.2

Other studies have shown that platinum nanoparticles of varying sizes (1.7, 2.9, 3.6, and 7.1 nm) supported within the channels of the mesoporous oxide SBA-15 behave similar to platinum single crystals upon CO-poisoning of ethylene hydrogenation[32]. The apparent activation energy for the reaction doubles from about 10 kcal/mol to about 20 kcal/mol upon poisoning with CO. This is interesting because catalysts such as these should also have oxide-metal interface sites available to turnover reaction. However, the cleaning of these catalysts is done by oxidation/reduction cycles with oxygen and hydrogen flowing over the catalysts while heating. The cleanliness of the platinum surface is not verified by Auger electron spectroscopy after the oxidation/reduction cycles, so there may be remaining carbon deposits on the surface, which block these interface sites. Therefore, a direct comparison with this type of supported catalyst is difficult at this time. Further work is needed to better characterize the nature of the oxide-metal bonding in our system and other supported catalyst systems in order to open up comparisons between different catalysts.

These investigations of the catalytic behavior of platinum model catalysts using a single reaction such as ethylene hydrogenation point to the existence of active sites other than the platinum metal sites. These active sites may allow the continued catalytic activity for some supported platinum catalysts as compared to the rapid deactivation of platinum crystal surfaces or thin films during hydrocarbon conversion.

3.6 Conclusions

Electron beam lithography has shown that nanofabrication methods can not only produce viable model catalysts in the sub-50 nm size regime, but can also enable broader conclusions about some of the macroscopic phenomena being measured in catalytic studies. These fabricated catalysts have proven to be viable model catalysts by use of ethylene hydrogenation as a probe reaction. EBL platinum nanoparticle samples have demonstrated the ability to resist poisoning by carbon monoxide, and a correlation has been made between the number of oxide-Pt interface sites and the CO-poisoned turnover frequency. Further studies incorporating the use of spectroscopy will help shed some light on the pertinent surface chemistry.

References

1. V.V. Poborechii, T. Tada, T. Kanayama, Appl. Phys. Lett. 75 (1999) 3276.
2. M.C. Wanke, O. Lehmann, K. Muller, Q. Wen, M. Stuke, Science 275 (1997) 1284.
3. A.J Haes, R.P. Van Duyne, JACS, 124 (2002) 10596.

4. K.-B. Lee, S.-J. Park, C.A. Mirkin, J.C. Smith, M. Mrksich, Science 295 (2002) 1702.
5. J. Hu, L.-S. Li, W. Yang, L. Manna, L.-W. Wang, A.P. Alivisatos, Science 292 (2001) 2060.
6. Y. Xia, P. Yang, Y. Sun, Y. Wu, B. Mayers, B. Gates, Y. Yin, F. Kim, H. Yan, Adv. Mat. 15 (2003) 353.
7. T. Mitsui, M.K. Rose, E. Fomin, D.F. Ogletree, M. Salmeron, Surf. Sci. 511 (2002) 259.
8. J. Christiansen, K. Morgenstern, J. Schiøtz, K.W. Jacobsen, K.-F. Braun, K.-H. Rieder, E. Lægsgaard, F. Besenbacher, Phys. Rev. Lett. 88 (2002) 206106-1.
9. M. Salmeron, G.A. Somorjai, J. Phys. Chem. 85 (1981) 3835.
10. M. Salmeron, G.A. Somorjai, J. Phys. Chem. 86, (1982) 341.
11. S.M. Davis, G.A. Somorjai, J. Phys. Chem. 87, (1983) 1545.
12. X. Su, P.S. Cremer, Y.R. Shen, G.A. Somorjai, J. Am. Chem. Soc. 119, (1997) 3994.
13. K.R. McCrea, J.S. Parker, G.A. Somorjai, J. Phys. Chem. B 106, (2002) 10854.
14. J. Horiuti, M. Polanyi, Trans. Faraday Soc. 30, (1934) 1164.
15. F. Zaera, G.A. Somorjai, J. Catal. 84, (1983) 375.
16. F. Zaera, G.A. Somorjai, J. Phys. Chem. 89, (1985) 3211.
17. A.L. Backman, R.I. Masel, J. Vac. Sci. Technol. 6, 1137 (1988).
18. A.L. Backman, R.I. Masel, J. Vac. Sci. Technol. A 9, (1991) 3.
19. P. Cremer, C. Stanners, J.W. Niemantsverdriet, Y.R. Shen, G.A. Somorjai, Surf. Sci. 328, (1995) 111.

20. T. Ohtani, J. Kubota, J.N. Kondo, C. Hirose, K. Domen, J. Phys. Chem. B 103, (1999) 4562.
21. R. Deng, E. Herceg, M. Trenary, Surf. Sci. 560, (2004) L195.
22. D.C. Tang, K.S. Hwang, M. Salmeron, G.A. Somorjai, J. Phys. Chem. B 108, (2004) 13300.
23. A.S. Eppler, J. Zhu, E.A. Anderson, G.A. Somorjai, Top. Catal. 13 (2000) 33.
24. J. Zhu, G.A. Somorjai, Nano Lett. 1 (2001) 8.
25. A.S. Eppler, G. Rupprechter, E.A. Anderson, G.A. Somorjai, J. Phys. Chem. B 104 (2000) 7286.
26. J.C. Schlatter and M. Boudart, J. Catal. 24 (1972) 482.
27. E. Segal, R.J. Madon, M.J. Boudart, Catal. 52 (1978) 45.
28. J. Grunes, J. Zhu, E.A. Anderson, G.A. Somorjai, J. Phys. Chem. B 106 (2002) 11463.
29. A.M. Contreras, J. Grunes, X.-M. Yan, A. Liddle, G.A. Somorjai, Cat. Lett. 100 (2005) 115.
30. F. Zaera, G.A. Somorjai, J. Am. Chem. Soc. 106 (1984) 2288.
31. K.S. Hwang, M. Yang, J. Zhu, J. Grunes, G.A. Somorjai, J. Mol. Cat. A 204-205 (2003) 499.
32. R.M. Rioux, R. Komor, H. Song, J.D. Hoefelmeyer, M. Grass, P.D. Yang, G.A. Somorjai, Submitted to Journal of Catalysis.

Chapter 4

Fabrication of 2-Dimensional Platinum Nanowire Arrays by Nanoimprint Lithography: Ethylene Hydrogenation and CO-Poisoning Reaction Studies

4.1 Abstract

Nanoimprint lithography (NIL) has been utilized to produce platinum nanowires in the 20 – 60-nm size range on oxide films (SiO_2 and Al_2O_3) deposited onto silicon wafers. A combination of characterization techniques (SEM, AFM, XPS, AES) has been used to determine size, spatial arrangement and cleanliness of these fabricated catalysts. Ethylene hydrogenation reaction studies have been carried out over these fabricated catalysts as a probe reaction and have shown to have comparable turnover rates and activation energies to other platinum catalysts.

4.2 Introduction

Metal single crystals have long been used as model catalysts in combined surface science and catalytic reaction studies. Platinum single crystals of different orientation

crystal faces have been used for H_2/D_2 exchange[1-3], CO oxidation[4,5], and hydrocarbon conversion reactions like ethylene hydrogenation[6-16]. They revealed the surface structure sensitivity or insensitivity of different catalytic reactions, the roles of surface defects such as steps and kinks, and additives that are bonding or structure modifiers. Many industrial platinum catalysts are nanoparticles that are dispersed on high surface area porous oxide supports. The resistance of these industrial catalysts to poisoning under industrial conditions has been the focus of much research, and it has been postulated that this may be due to the presence of an oxide-metal interface. Single crystals provide a wealth of information about adsorbate bonding to different crystal faces and catalytic reaction mechanisms, but are unable to successfully model reactivity intrinsic to industrial catalysts that involve the oxide-metal interface or the oxide surface. One direction of research in our laboratory is to bridge this gap between the catalytic chemistry of model single crystals and high surface area platinum nanocluster catalysts used in the chemical technologies. There has been considerable effort to create a model catalytic system with an oxide-metal interface that can be tuned precisely in the nanometer size range. While turnover frequencies are measured under many conditions for various oxide-metal systems, the nature of the catalytically active sites in industrial catalysts is not well understood. Thus, precise control over the fabrication of a catalyst must be achieved to allow systematic variance of different parameters of the metal structure such as size and spacing as well as a choice of the oxide-metal interface of the catalyst. To this end, we first explored the use of electron beam lithography (EBL) to construct platinum nanoparticle arrays on oxide surfaces as new model platinum catalysts as described in Chapter 3[17,18]. Approximately 10^9 nanoparticles could be produced

using this technique on a 1-cm^2 silicon wafer in about a day. This corresponds to a platinum surface area of about 0.1 cm^2. However, the study of low turnover reactions ($<10^{-4}$ s^{-1}) requires ~1 cm^2 of platinum surface area for practical detection of reaction products. Because of the sequential nature of electron beam exposure, the production of ~1 cm^2 of exposed platinum surface area would require approximately 10 days to fabricate, which is not practical. While the EBL-fabricated platinum samples could be used to study high turnover reactions (such as ethylene hydrogenation) or the thermal and chemical stability of the platinum nanoparticles, we turned to another technique, photolithography, to fabricate higher surface area nanoarrays of platinum catalysts. Photolithography techniques have been used successfully in the microelectronic industry for years and have proven successful in creating sub-μm structures with high degree of uniformity and reproducibility[19-21]. Size reduction lithography (SRL), developed in our laboratory, couples photolithography with low-pressure chemical vapor deposition and reactive-ion etching techniques to create structures smaller than the normal diffraction limits of photolithography. When this size-reduction technique is used multiple times, it can drastically increase feature density. SRL has previously demonstrated the ability to produce a silicon mold with nanowire structures of 7-nm diameter[22,23]. It has also been shown, that a silicon mold can be used in nanoimprint lithography (NIL) to reproduce sub-10 nm features by using the mold to imprint its features into a polymer resist and depositing the desired material into the negative of the mold pattern[24-26]. The NIL process is a practical fabrication method, which offers a high-throughput method with low production cost, and a choice of deposition materials and substrates. Here, size reduction lithography has been used in conjunction with

nanoimprint lithography to fabricate arrays of platinum nanowires. After using photolithography and SRL to produce a silicon mold with nanowire features, the mold was used to imprint its features into a polymer resist. This imprint was followed by platinum deposition through the imprinted features to produce platinum replicas of the original silicon mold on either a SiO_2 or Al_2O_3 surface.

This paper describes the production of platinum nanocatalyst arrays fabricated by NIL to create nanowire arrays. We use these platinum nanoarrays to carry out ethylene hydrogenation with and without the presence of carbon monoxide. The collected experimental data indicates that these nanoarrays have similar turnover rates and activation energies to other platinum model catalysts.

4.3 Experimental

4.3.1 Pt nanowire arrays on alumina and silica: fabrication by NIL

The process for using SRL to define a nanowire array on a single-crystalline Si surface has been detailed previously[22,23]. Briefly, the Si mold used for fabrication of Pt nanowire arrays was fabricated by first growing a 50 – 70-nm thermal SiO_2 layer onto the surface of a Si(100) wafer. Next, a 100-nm polysilicon layer is deposited by low-pressure chemical vapor deposition (LPCVD) at 873 K as a sacrificial layer. A positive photoresist is spincast onto the poly-Si layer and exposed to radiation through a patterned mask. The radiation-exposed polymer is removed with developing solution. This leaves the unexposed, patterned photoresist on top of a polysilicon layer. This pattern is then transferred into the underlying polysilicon layer by reactive-ion etching in a HBr and Cl_2 plasma (LAM TCP 9400). The remaining 20 – 30 nm of photoresist is then stripped off

in oxygen plasma. An SEM image of the polysilicon features is shown in Figure 4.2b. At this point, a low-temperature silicon oxide (LTO) layer is deposited over the defined polysilicon pattern by low-pressure chemical vapor deposition at 723 K. This is a conformal deposition and coats the entire patterned surface. The thickness of the sidewall deposition during this step will define the ultimate feature size. The LTO layer on top of the sacrificial polysilicon feature is anisotripically etched away in CF_4 plasma. The exposed polysilicon feature is then selectively etched away leaving an LTO pattern of nanowires on the thermal oxide underlayer. These wire features are transferred into the thermal oxide layer by anisotropic etching with CF_4 plasma. The thermal oxide pattern is then transferred into the single-crystalline Si wafer by anisotropically etching with HBr and Cl_2 plasma. 20-nm silicon nanowires are routinely produced by this process. This process is pictured schematically in Figure 4.1a. Oxidative trimming techniques are then used to reduce the nanowire width. The wafer is thermally oxidized at 1073 K for 30 minutes and then dipped into HF for oxide removal, reducing the wire width to 7 nm. The nanowire features on the Si mold used in the preparation of samples for this study had a height of 110 nm, and a width of 7 nm (Figure 4.1c).

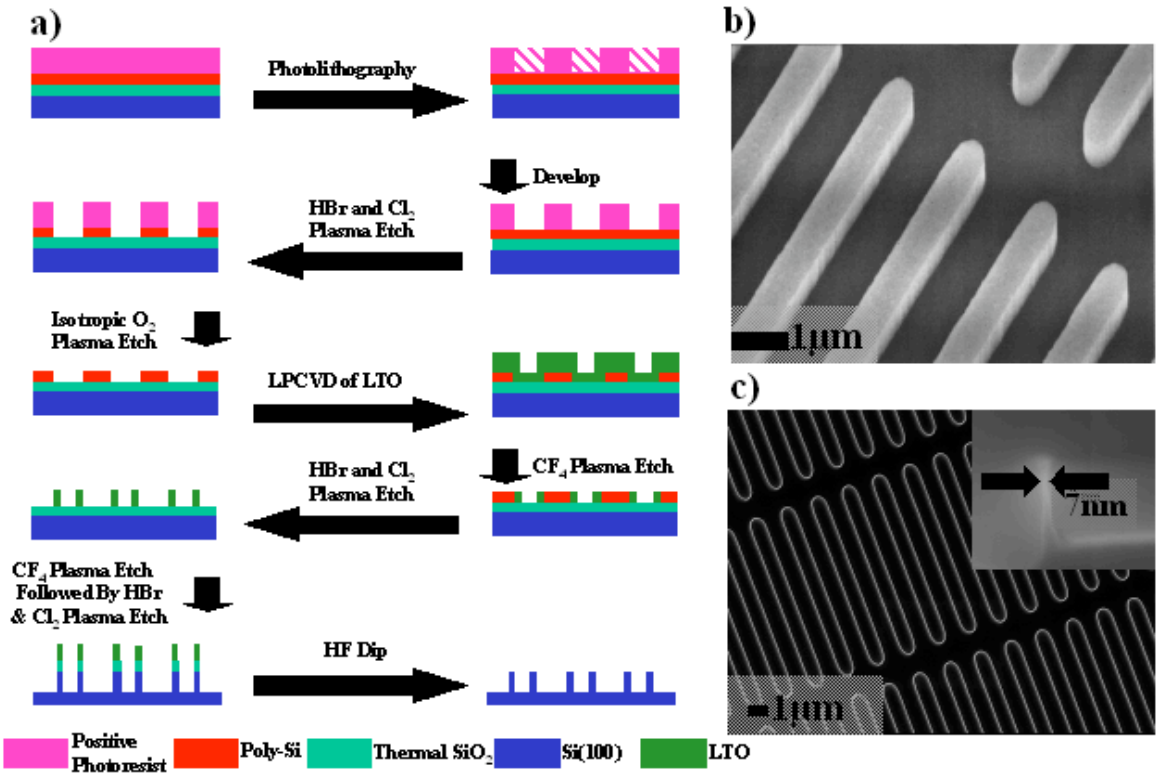

Figure 4.60: a) SRL Scheme used for fabrication of Si nanowire mold. A Si(100) wafer is used to grow a thermal oxide (SiO2). A polysilicon layer is then grown by low-pressure chemical vapor deposition (LPCVD) on top of the thermal oxide. A positive photoresist is spincast onto the poly-Si surface and exposed to radiation through a patterned mask. The pattern is developed and etched into the poly-Si layer with HBr and Cl2 plasma. A conformal deposition of low temperature oxide (LTO) covers the poly-Si features, and the sidewalls of this deposition define the new feature size. The poly-Si feature is exposed by a CF4 plasma etch. The poly-Si is then selectively removed by an HBr & Cl2 plasma etch. The pattern can now be transferred into the Si wafer by etching through the SiO2 layers with CF4 plasma followed by HBr & Cl2 plasma to etch the pattern into the wafer. An HF dip cleans the surface of all SiO2 and leaves the features made of single crystal silicon. b) SEM image of polysilicon features on SiO2 support. Features have a 600-nm width with 1.2□m spacing. c) SEM image of final silicon mold with nanowire pattern. Wires are Si(100) as is the support. The inset shows the 7-nm sidewall of the silicon nanowire pattern.

This Si nanowire pattern was used as a mold to reproduce its patterns by use of NIL. The NIL fabrication method used to create our catalysts is shown schematically in Figure 4.2a. Previous to using the silicon mold for imprinting, the surface is functionalized by physical vapor deposition of a fluoropolymer, which acts as a lubricant. The fluoropolymer used to functionalize the silicon surface is (tridecafluoro-1,1,2,2-tetrahydrooctyl)-1-trichlorosilane or $C_6F_{13}C_2H_4SiCl_3$ (FTS). The FTS solution prepared

was 10% by mass in *n*-octane. The FTS solution is physical vapor deposited onto the silicon mold surface at 343 K for five minutes. Contact angle measurements on the silicon mold showed a water contact angle of approximately 100° after deposition of the fluoropolymer. This surface functionalization lowers the surface energy of the mold, so that separation of the mold from the imprinted polymer substrate is more facile. The polymer used for our imprinting was (poly)-methylmethacrylate (PMMA M_w=15 k). The PMMA solution prepared was 4% by mass in chlorobenzene. This solution is spincast at 900 RPM onto a Si(100) wafer coated with either 15 nm of alumina or silica. The sample is then baked at 363 K for 5 minutes to remove residual solvent. The resultant PMMA films have an average thickness of about 180 nm measured by reflectometry. The PMMA coated substrate and Si mold are placed in contact with each other for imprinting. The mold and substrate are heated to 400 K (PMMA T_g=378 K) and pressed to 4000 PSI (27.6 MPa) for 5 minutes. The mold and substrate are then cooled under pressure by flowing N_2 gas over the imprinting apparatus and subsequently separated at room temperature leaving the negative pattern of the Si mold in the PMMA layer. It was found that a better imprint resulted from more rapid cooling with N_2 gas rather than allowing the apparatus to cool slowly. To remove the remaining polymer from the bottom of the imprinted features it is necessary to etch the pattern deeper into the polymer layer. To avoid any broadening from this etching and in an attempt to control the final feature size, 15 nm of SiO_2 is shadow deposited by electron beam evaporation at an optimized 45° angle with respect to the evaporation source. The substrate is then rotated 180° and 15 nm of SiO_2 is again evaporated at a 45° angle with respect to the evaporation source. At this point, the remaining PMMA at the bottom of the imprinted features is removed by O_2

reactive-ion etching (LAM TCP 9400) using 10 mTorr O_2 pressure, a flow of 100 sccm with the top and bottom electrodes set at 100 W and 25 W, respectively. After etching the residual polymer layer away, 15 nm of Pt is vacuum deposited, by electron beam evaporation with a quartz crystal microbalance thickness monitor. The Pt is deposited through the imprinted pattern and onto the exposed oxide support. The remaining polymer is removed by ultrasonication in acetone for five minutes, leaving a Pt array of nanowires. The "shadow deposition" process employed here has been used and studied in the past[27] and is used successfully here to protect the imprinted sidewall from broadening during reactive-ion etching and in defining a smaller feature size in the final pattern. The 7-nm diameter Si features on the mold have been transformed into 22-nm and 25-nm features of Pt on alumina and silica, respectively. Despite the shadow deposition, there is still significant broadening in the features indicating that the broadening originates during the imprint process. It was found that the post-spin bake was not long enough to evaporate all of the solvent from the polymer. So upon heating up to the imprinting temperature, the remaining solvent evaporates and broadens the features[28]. This problem is currently being addressed. An AFM image of the 22-nm Pt nanowire array on an alumina substrate is pictured below in Figure 4.2b and an SEM image of the same sample is shown in Figure 4.2c. A 64-nm Pt nanowire array on silica was also prepared by NIL without the use of the shadow deposition process.

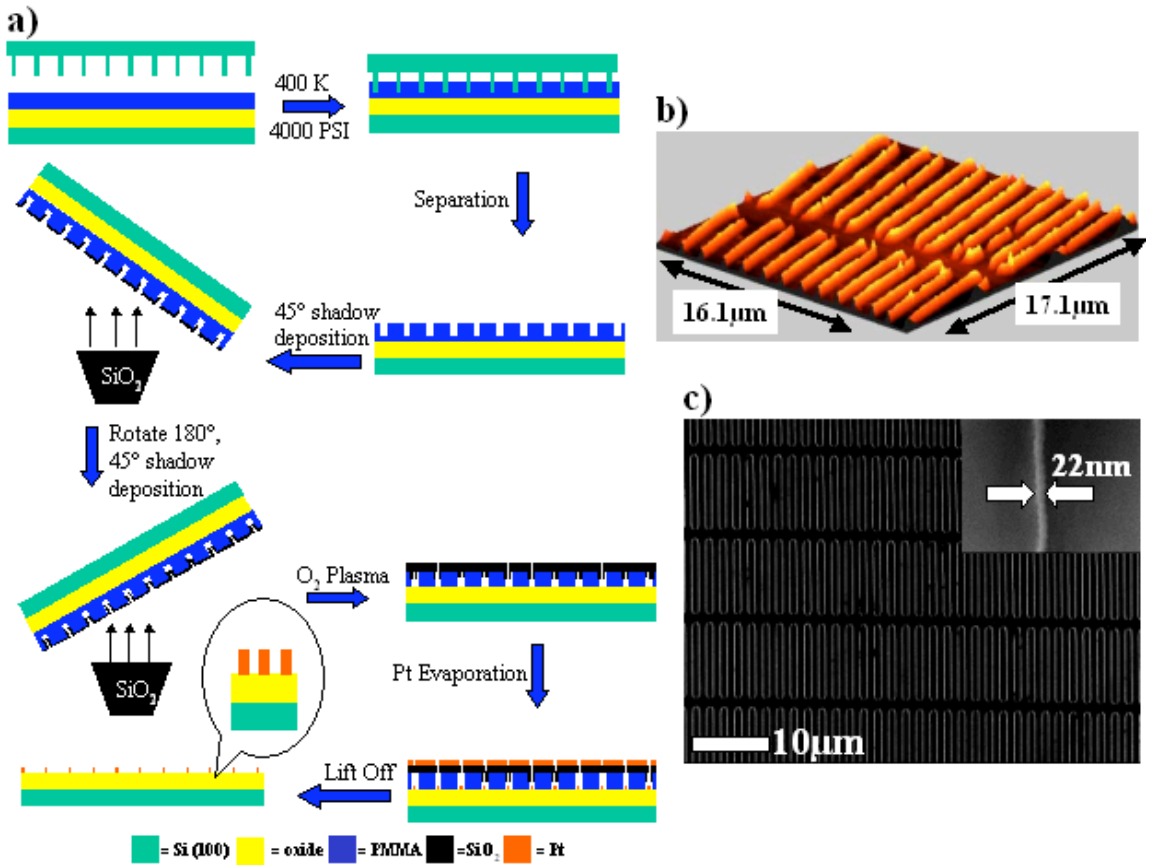

Figure 4.61: a) Nanoimprint lithography fabrication scheme. PMMA is spincast onto an oxide-coated wafer and placed in contact with the Si mold. The mold and PMMA-coated wafer are heated to 400 K and pressed to 4000 PSI for 5mins. 15 nm of SiO_2 is deposited by electron beam evaporation at a 45° angle. The sample is rotated 180° and another 15 nm of SiO_2 is deposited at a 45° angle. The remaining PMMA at the bottom of the imprinted features is removed by an O_2 plasma etch. 15 nm of platinum is deposited onto the exposed oxide surface and remaining PMMA is removed by submersing the sample in acetone and ultrasonicating for 5 minutes. b) AFM image of Pt nanowires on alumina support showing 15-nm height of wires. c) SEM image of Pt nanowires on alumina support. Inset shows 22-nm width of wires.

4.3.2 Characterization

The Pt nanoarrays were characterized by scanning electron microscopy (SEM), atomic force microscopy (AFM), and x-ray photoelectron spectroscopy (XPS). SEM images are taken with a JEOL JSM-6340F equipped with a cold field emission source operating between 3 kV and 20 kV with a probe current of 12 □A. All SEM images are acquired using an E-T combined backscatter and secondary electron detector at a working

distance of 6 mm. Typical SEM images of the samples are shown in Figures 4.1b, 4.1c and 4.2c. AFM is used to determine the height and periodicity of the arrays. AFM images of the nanoparticle arrays are taken on a Park Scientific Instruments, M5 AFM. AFM images of the nanowire arrays are taken on a Molecular Imaging PicoSPM. Both AFM's use a feedback loop between a scan piezo and a position-sensitive photodiode array at a constant force to monitor the reflected laser light from the backside of the cantilever. A typical AFM image of the samples is shown in Figures 4.2b. XPS spectra are taken to analyze the chemical composition of the surface after fabrication. Spectra are taken on a 15-kV, 40-Watt PHI 5400 ESCA/XPS system equipped with a Mg anode x-ray source. Samples are cleaned of any foreign particulates before being analyzed with a stream of nitrogen gas. The spectra are inspected for the Pt $4f_{7/2}$ and $4f_{5/2}$ peaks to verify that platinum had been deposited. As well, the spectra verify the presence of the characteristic Si and Al peaks for each of the oxide substrates.

4.3.3 Reaction Apparatus

The reaction studies are carried out in an ultrahigh vacuum (UHV) chamber equipped with a high-pressure reaction cell. The general design of this type of chamber has been described elsewhere[29] and is shown schematically in Chapters 2 and 3. The outer chamber achieved a working pressure of $1\square10^{-9}$ Torr between reactions. The chamber was evacuated by use of a turbomolecular pump (Balzers TPU 330), and an ion pump (Varian). All of the nanocatalyst arrays are cleaned by dosing with $1\square10^{-6}$ Torr of NO_2 at 573 K for 20 minutes, followed by dosing the sample with 10L of CO and flashing the temperature to 573 K to remove the remaining CO from the surface. This procedure has been established to be effective for cleaning supported Pt nanostructures

and Pt(111) single crystals of their major surface impurities such as carbon and oxygen[30]. This cleaning procedure is used before the start of every experiment. The catalyst samples are mounted on a ceramic heater (Advanced ceramics, HT-01) with Ta clips. The temperature of the surface is measured with a 0.010-in. diameter chromel/alumel thermocouple wire. The thermocouple wire is clamped to the sample with a Ta clamp and an alumina spacer. The alumina spacer is used to avoid electrical contact between the heater and the thermocouple. Auger electron spectroscopy (AES) is used to monitor the surface cleanliness of the sample. All Auger spectra are taken using a Physical Electronics Industries, Inc. Auger system. As the Auger process itself can deposit carbon impurities on the surface of the sample, the sample is always cleaned after any Auger spectra are taken.

4.3.4 Reaction Studies

Every sample is cleaned as described above before introducing reaction gases. Catalytic studies are carried out on all catalyst samples using 10 Torr C_2H_4, 100 Torr H_2, and 650 Torr Ne gas. For CO poisoning studies, 300 mTorr of CO is added to the manifold with the reaction gases. Gases are premixed in the gas manifold approximately 20 minutes before introduction to the catalyst and the reaction line. The gases are circulated through the reaction line with a Metal Bellows re-circulation pump. A HP Series II gas chromatograph equipped with a FID detector and a 50-m alumina capillary column (J&W Scientific) was used to separate and analyze products. The GC was part of the reaction loop and sampled the circulating reaction gases every 2.5 minutes using an automatic sampling valve. The H_2, C_2H_4, Ne, and CO had gas purities of 99.99%, 99.5%, 99.999%, and 99.3%, respectively.

4.4 Results

4.4.1 Nanowire Samples on Alumina and Silica

SEM images of the nanowire arrays on silica and alumina show the nanowire diameters to be 64 ± 3 nm and 25 ± 2 nm on silica, and 22 ± 2 nm on alumina. SEM measurements also show the distance in the middle of the wire to be 600 ± 3 nm and between two different wires to be 1072 ± 4 nm for the 64-nm Pt wires, 1150 ± 3 nm for the 25-nm Pt wires, and 1156 ± 3 nm for the 22-nm Pt wires. AFM images of the nanowires, show them to have a height of 15 ± 1 nm (Figure 4.2b) and confirm the width of the Pt features. AFM and SEM images above in Figures 4.2b and 4.2c, respectively are that of the 22-nm nanowires on an alumina substrate.

4.4.2 Reaction Studies

The ethylene hydrogenation reaction studies over the various catalyst arrays were carried out in the 313 – 413 K temperature range without the presence of CO and in the 393 – 473 K temperature range with the presence of CO. This is a structure insensitive reaction on platinum catalysts, meaning that under most conditions the turnover rate will be the same for different platinum catalysts reacting under similar conditions. A summary of the measured activation energies and the turnover rates at 300 K is shown below in Table 4.1 for all of the fabricated catalysts. The accumulation of ethane is monitored by gas chromatography and is plotted versus reaction time. The slope of this accumulation curve yields the rate of reaction at different temperatures and using this information, Arrhenius plots are constructed to obtain the apparent activation energy of reaction. Due to the small metal surface area of the catalyst samples, ethane accumulation is slow at room temperature. Therefore, all reported turnover rates have

been extrapolated from the Arrhenius plots to recover the turnover rates at 300 K. The reactions on the fabricated catalysts will be compared to the reaction studies on Pt(111) single crystal by Zaera *et. al.*[31] and Hwang *et. al.*[32]. The single crystal data shows a turnover rate of 10 s^{-1} and an activation energy of 10.8 ± 0.1 kcal/mol with no CO poisoning. Upon CO poisoning, the turnover rate decreases sharply to 4.8 × 10^{-6} s^{-1} and there is a corresponding increase in the activation energy to 20.2 ± 0.1 kcal/mol. The turnover rate of for the Pt(111) single crystal was calculated using the empirical rate equation of Zaera *et. al*[31]. The turnover rate for the CO poisoning of the single crystal was extrapolated from the Arrhenius plot in ref. 32.

Table 4.4: Summary of reaction studies.

Catalyst Sample	Unpoisoned E_a (kcal/mol)	CO Poisoned E_a (kcal/mol)	Unpoisoned Turnover Frequency @300K (s^{-1})	Poisoned Turnover Frequency @300K (s^{-1})
Pt (111)[31,32]	10.8 ± 0.1	20.2 ± 0.1	10	4.8 × 10^{-6}
22-nm Pt nanowires on alumina support	13.6 ± 0.2	21.3 ± 0.2	14	5.0 × 10^{-5}
25-nm Pt nanowires on silica support	13.5 ± 0.1	22.2 ± 0.3	11	1.4 × 10^{-5}
64-nm Pt nanowires on silica support	13.0 ± 0.3	19.8 ± 0.3	9.1	7.9 × 10^{-5}

A size comparison was done for Pt nanowires on a silica support with nanowires of diameters 25 nm and 64 nm. Unpoisoned ethylene hydrogenation measured on these wire samples shows apparent activation energies of 13.5 ± 0.1 kcal/mol and 13.0 ± 0.3 kcal/mol, and turnover rates of 11 s^{-1} and 9.1 s^{-1}, respectively. The measured activation energies are a bit higher than that measured for the Pt(111) and Pt nanoparticles, but the turnover rates are around the accepted value of 10 sec^{-1}. CO poisoning of the reaction

measured on the 25-nm wires show an apparent activation energy of 22.2 ± 0.3 kcal/mol and a turnover rate of 1.4 × 10^{-5} s^{-1}. The 64-nm nanowire array show an apparent activation energy of 19.8 ± 0.3 kcal/mol and a turnover rate of 7.9 × 10^{-5} s^{-1} for the CO poisoning study. Both arrays have a 6 order of magnitude drop in the turnover rate upon CO poisoning whereas the Pt(111) shows a drop of seven orders of magnitude. The difference in wire diameter of the two arrays did not make a difference in their reactivities in comparison to each other. Both arrays have almost identical turnover rates and activation energies. Next, these reactions were studied on a sample of 22-nm diameter Pt nanowires on an alumina support. This sample was considered comparable in wire size to the 25-nm Pt nanowire sample on silica. The 22-nm Pt nanowires on alumina show an unpoisoned activation energy of 13.6 ± 0.2 kcal/mol with a turnover rate of 14 s^{-1}. CO poisoning of the catalyst gives a measured activation energy of 21.3 ± 0.2 kcal/mol with a turnover rate of 5.0 × 10^{-5} s^{-1}. The apparent activation energies of the 22-nm and 25-nm samples are almost identical for both the unpoisoned and CO-poisoned reactions. The unpoisoned turnover rate on the alumina-supported nanowires, however, is higher than any of the other catalyst samples. The poisoned turnover rate on the alumina-supported nanowires drops 6 orders of magnitude as the silica-supported samples did, which again, gives a turnover rate that is about an order of magnitude higher than that of the Pt(111) after CO poisoning. The Arrhenius plots for the reaction studies conducted on these three nanowire samples is shown in Figures 4.3a-c.

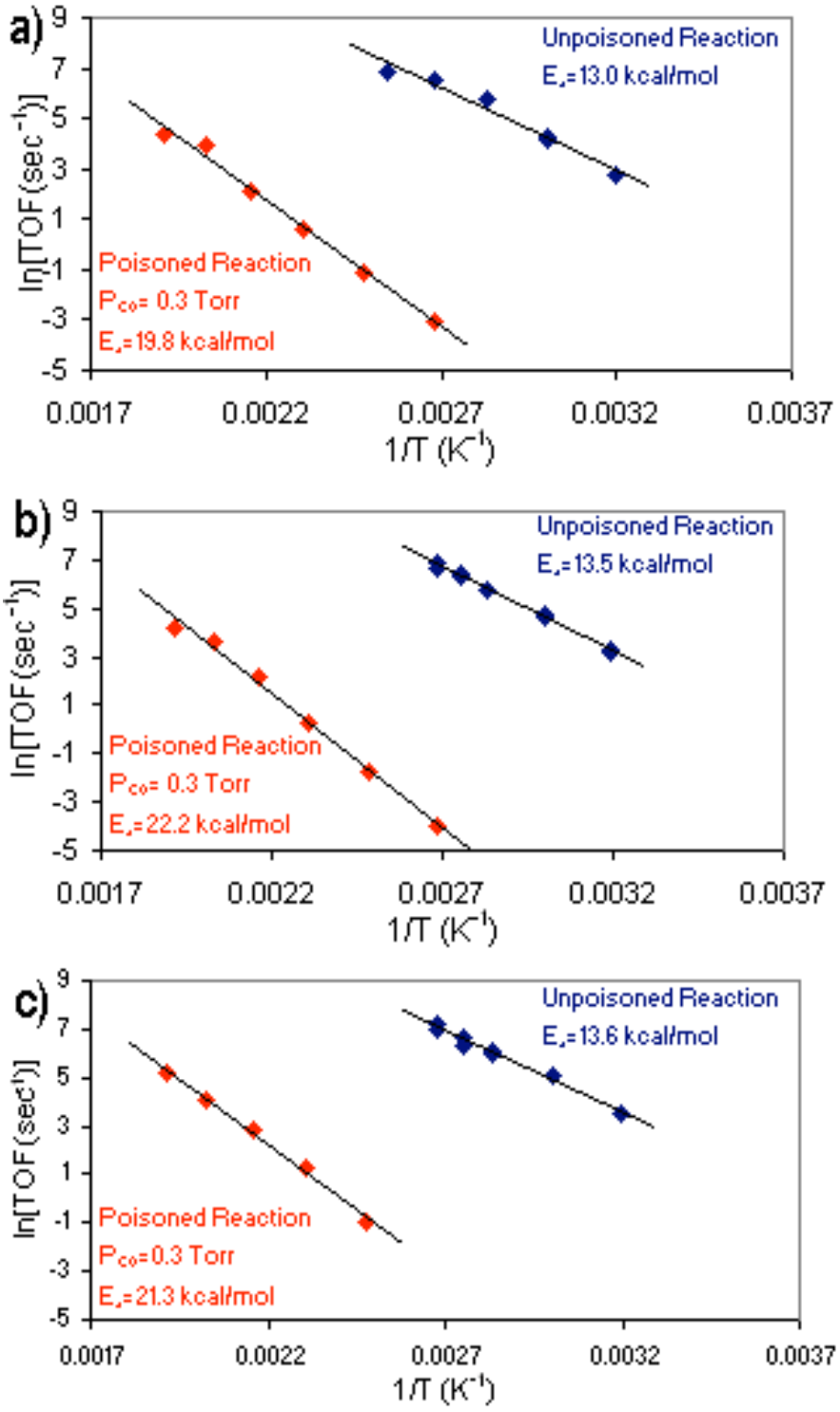

Figure 4.62: Arrhenius plots for ethylene hydrogenation reactions on Pt nanowires arrays. a) 64-nm diameter Pt nanowires on silica support. b) 25-nm diameter Pt nanowires on silica support. c) 22-nm diameter Pt nanowires on alumina support.

4.5 Discussion

Table 4.1 above summarizes the turnover rates and activation energies for ethylene hydrogenation on the platinum nanowires deposited on silica or alumina with and without CO poisoning. These results are also compared with similar data obtained on the (111) crystal face of platinum, which may be used as a reference state of a platinum catalyst without the presence of an oxide support. In order to calculate the turnover rates for each of the fabricated catalyst arrays, the metal surface area was calculated using geometrical considerations. The nanowire wall geometry was considered to be that of a rectangle standing on an oxide support with a height of 15 nm, and the top of each wire was also considered to be rectangular. As well, the half circles on either end of the wires were considered and measured as cylindrical arcs standing on an oxide support. The platinum and oxide surface areas that result from these calculations are shown below in Table 4.2. Without the presence of oxide, the clean Pt(111) surface has a turnover rate of about 10 s^{-1} at 300 K and an activation energy of about 11 kcal/mol. The oxide-supported platinum nanowires have very similar turnover rates with the exception of the alumina-supported nanowires, which have a 40% higher value. Also, the activation energies for the ethylene hydrogenation are about 2 kcal/mol higher (~13 kcal/mol) for the platinum nanowire systems than the activation energy for the platinum single crystal. The reasons for these differences are yet to be determined and await vibrational spectroscopy studies using sum frequency generation, which may reveal adsorbed surface species on these catalysts in addition to that of ethylidyne.

Table 4.5: Comparison of catalyst metal and oxide surface areas.

Catalyst Sample	Total Pt Surface Area (cm^2)	Oxide Surface Area (cm^2)	Ratio of Oxide to Metal Surface Area
22-nm Pt nanowires on alumina support	0.066 ± 0.003	1.2 ± 0.1	18 ± 2
25-nm Pt nanowires on silica support	0.060 ± 0.003	1.0 ± 0.1	17 ± 2
64-nm Pt nanowires on silica support	0.10 ± 0.01	1.0 ± 0.1	9.8 ± 1

When poisoning the reaction with CO, the nanowire arrays behave very similar to the platinum single crystal. CO binds strongly to platinum and thus adsorbs preferentially to other gases in the reaction mixture like ethylene. Before a reaction can occur, a CO molecule must desorb from the metal surface. CO also restricts the mobility of the adsorbed reactant molecules, therefore lowering the probability of a reaction occurring. For Pt(111), CO poisoning of the reaction increases the activation energy to 20 kcal/mol, and decreases the turnover rate at 300 K by seven orders of magnitude, to approximately 10^{-6} s^{-1}. Similar results are obtained for the platinum nanowires. The activation energy for the reaction on the poisoned Pt-wire surface is around 20 – 22 kcal/mol. However, turnover rates are about an order of magnitude higher, ~10^{-5} s^{-1} as compared to Pt(111). The CO-poisoned turnover frequencies for the nanowire arrays and Pt(111) are extremely low values and are extrapolated from actual data. Therefore, it is difficult to state clearly if the nanowires samples are displaying the same behavior as the Pt(111) or if there is some resistance to CO-poisoning.

These investigations of the catalytic behavior of platinum nanowires indicate that this type of system is viable for model catalytic studies. Ethylene hydrogenation is a surface insensitive reaction. So, the fact that the nanowire arrays show similar kinetics to

other platinum catalysts opens the door for more studies of various reactions. As well, it verifies the fact that not only is there platinum available on the surface for reaction, but that the geometrical considerations used to calculate the metal surface area are accurate. This type of system allows for facile changing of the materials and the system variables, which is key to modeling something as complex as heterogeneous catalysis. Further studies can now be focused on changing one of the variables in the system. Chapters 5 and 6 will detail the fabrication of Pt nanowire arrays on different oxide supports, and the results of CO oxidation reaction studies on those samples, respectively.

4.6 Conclusion

SRL, and NIL techniques can be used successfully to create model catalysts in the sub-100 nm size regime. These fabricated catalysts have proven to be viable model catalysts by use of ethylene hydrogenation as a probe reaction. Further studies using platinum nanowires on different supports and with different reactions can perhaps help shed some light as to the importance of the oxide-metal interface on catalytic reactions.

References

1. M. Salmeron, G.A. Somorjai, J. Phys. Chem. 85 (1981) 3835.
2. M. Salmeron, G.A. Somorjai, J. Phys. Chem. 86, (1982) 341.
3. S.M. Davis, G.A. Somorjai, J. Phys. Chem. 87, (1983) 1545.
4. X. Su, P.S. Cremer, Y.R. Shen, G.A. Somorjai, J. Am. Chem. Soc. 119, (1997) 3994.
5. K.R. McCrea, J.S. Parker, G.A. Somorjai, J. Phys. Chem. B 106, (2002) 10854.

6. J. Horiuti, M. Polanyi, Trans. Faraday Soc. 30, (1934) 1164.
7. F. Zaera, G.A. Somorjai, J. Catal 84, (1983) 375.
8. F. Zaera, G.A. Somorjai, Langmuir 2 (1986) , 686.
9. F. Zaera, G.A. Somorjai, J. Phys. Chem. 89, (1985) 3211.
10. D. Godbey, F. Zaera, R. Yeates, G.A. Somorjai, Surf. Sci. 167, (1986) 150.
11. A.L. Backman, R.I. Masel, J. Vac. Sci. Technol. 6, 1137 (1988).
12. A.L. Backman, R.I. Masel, J. Vac. Sci. Technol. A 9, (1991) 3.
13. P. Cremer, C. Stanners, J.W. Niemantsverdriet, Y.R. Shen, G.A. Somorjai, Surf. Sci. 328, (1995) 111.
14. T. Ohtani, J. Kubota, J.N. Kondo, C. Hirose, K. Domen, J. Phys, Chem. B 103, (1999) 4562.
15. R. Deng, E. Herceg, M. Trenary, Surf. Sci. 560, (2004) L195.
16. D.C. Tang, K.S. Hwang, M. Salmeron, G.A. Somorjai, J. Phys. Chem. B 108, (2004) 13300.
17. A.S. Eppler, J. Zhu, E.A. Anderson, G.A. Somorjai, Top. Catal. 13 (2000) 33.
18. J. Zhu, G.A. Somorjai, Nano Lett. 1 (2001) 8.
19. C.H. Ting, K.L. Liauw, J. Vac. Sci. Technol. B 1 (1983) 1225.
20. S.A. Rishton, D.P. Kern, J. Vac. Sci. Technol. B 5 (1987) 135.
21. M.T. Bohr, App. Surf. Sci. 101 (1996) 534.
22. Y.K. Choi, J. Zhu, J. Grunes, J. Bokor, G.A. Somorjai, J. Phys. Chem. B 107 (2003) 3340.
23. Y.K. Choi, J.S. Lee, J. Zhu, G.A. Somorjai, J. Bokor, J. Vac. Sci. Tech. B 21 (2003) 2951.

24. S.Y. Chou, P.R. Krauss, P.J. Renstrom, Appl. Phys. Lett. 67 (1995) 3114.

25. S.Y. Chou, P.R. Krauss, P.J. Renstrom, Science 272, (1996) 85.

26. S.Y. Chou, P.R. Krauss, W. Zhang, L.J. Guo, L. Zhuang, J. Vac. Sci. Technol. B 15, (1997) 2897.

27. L.F. Johnson, K.A. Ingersoll, G.W. Kammlott, Appl. Phys. Lett. 34 (1979) 578.

28. C. Gourgon, J.H. Tortai, F. Lazzarino, C. Perret, G. Micouin, O. Joubert, S. Landis, J. Vac. Sci. Technol. B 22 (2004) 602.

29. E. Segal, R.J. Madon, M.J. Boudart, Catal. 52 (1978) 45.

30. J. Grunes, J. Zhu, E.A. Anderson, G.A. Somorjai, J. Phys. Chem. B 106 (2002) 11463.

31. F. Zaera, G.A. Somorjai, J. Am. Chem. Soc. 106 (1984) 2288.

32. K.S. Hwang, M. Yang, J. Zhu, J. Grunes, G.A. Somorjai, J. Mol. Cat. A 204-205 (2003) 499.

Chapter 5

Fabrication of 2-Dimensional Platinum Nanowire Arrays of Different Oxide Supports by DUV and Nanoimprint Lithography: CO Oxidation Reaction Studies and Annealing Studies

5.1 Abstract

High-density arrays of platinum nanowires with dimensions 20 nm × 5 nm × 12 μm (width × height × length) have been produced on planar oxide thin films of silica, alumina, zirconia, and ceria. These nanowire arrays have been used as two-dimensional platinum model catalysts to study the effects of support on catalytic activity during the catalytic oxidation of carbon monoxide. A strong oxide support dependence is seen for both reaction turnover frequency and apparent activation energy. The thermal stability of these nanowire arrays has been studied by annealing at 773 K and 973 K in a flow of helium. Silicon migration through the oxide support and nanowire instability is seen upon annealing.

5.2 Introduction

Transition metal catalysts usually consist of nanoparticles in the 1-100 nm size-range deposited on high surface-area supports. The particle size, surface structure and the oxide-metal interface all influence catalytic activity, selectivity, and resistance to deactivation. Model metal catalysts, usually in the form of single crystals, have been used with success to elucidate many of the atomic scale ingredients that influence catalytic performance. Single crystals, however, inherently lack the complexity of industrial catalysts, and therefore, cannot fully model the workings of these catalysts. Factors such as the oxide-metal interface and the metal particle size are known to affect catalytic activity greatly. The importance of the oxide-metal interface was shown in Chapter 3, where oxide-metal interface sites demonstrated the ability to stay catalytically active despite being poisoned by CO during the catalytic hydrogenation of ethylene. The nanowire arrays described in Chapter 4 offer a system that can be used to dissect the inner workings of industrial catalysts, in that, factors such as the wire width, height and different types of support can be systematically changed to see their effects on catalytic activity.

The removal of CO from the exhaust of automobiles by oxidation to CO_2 is very important industrially and to society as a whole. Thus, CO oxidation is a well studied reaction[1-4] and is very significant industrially[5,6]. It is a relatively simple reaction where oxygen and CO combine on the surface of platinum catalysts to form CO_2 and desorb. Much is still not understood, however, about the interaction of support and its effects upon the metal structure to aid or hinder reaction.

This chapter describes the fabrication of dense arrays of platinum nanowires deposited on oxide thin film surfaces of ZrO_2, SiO_2, Al_2O_3, and CeO_2. These samples have been fabricated by combining sub-lithographic nanofabrication[7] and nanoimprint technology[8,9]. The nanowire dimensions are uniform and are controllable with nanometer precision. The typical dimensions of a single nanowire are 20 nm × 5 nm × 12 μm (width × height × length). On a 5×5 cm^2 flat substrate, a total of 8×10^8 nanowires can be fabricated, which gives a total exposed metal surface area larger than 2 cm^2. The fabrication of these nanowire arrays and their use as two-dimensional model catalysts to study the effects of oxide support on the catalytic oxidation of CO is reported in this chapter. In addition, annealing studies have been performed and described to study the thermal stability of these arrays.

5.3 Experimental

5.3.1 Fabrication of Platinum Nanowires on Oxide Surfaces

5.3.1.1 Fabrication of a Single Crystalline Si Mold by Size Reduction Lithography and Characterization

A detailed description of size reduction lithography (SRL) can be found elsewhere[10,11]. The SRL process is shown schematically in Figure 5.1a. Briefly, a 50-nm hard mask oxide (SiO_2) is thermally grown on a Si(100) wafer. A 120-nm polysilicon film is deposited on the hard mask oxide by low-pressure chemical vapor deposition (LPCVD) of silane. The polysilicon serves as a sacrificial layer to support and hold the sidewall spacers. The polysilicon layer is then patterned by deep-UV lithography (DUV) and plasma reactive ion etching (RIE) to form 0.25-μm wide, 12-μm long polysilicon line pattern with 0.25-μm spacing between lines. A 10-nm thick high-

temperature silicon oxide (HTO) film is then conformally deposited onto the patterned polysilicon by the LPCVD of SiH_2Cl_2 and N_2O. This coats both the tops and sidewalls of the patterned polysilicon layer. After the HTO is etched back anisotropically by CF_4 plasma, the polysilicon is exposed and is selectively removed by HBr and Cl_2 plasma etching. The selective removal of the polysilicon leaves 10-nm sidewall oxide spacers, which serve as an etching mask to pattern the underlying single-crystalline silicon. These relatively tall HTO spacers are transferred to the hard mask thermal oxide by CF_4 plasma. Next, the pattern is transferred into the Si(001) wafer by anisotropically etching in HBr and Cl_2 plasma. The residual thermal oxide mask is removed by buffered HF wet etching. Further size reduction of the silicon wires can be achieved by thermal oxidation, but this technique was not used here[11,12]. The principle of the SRL is based on the fact that material deposited during low-pressure chemical vapor deposition covers the step edge as well as the top of the step, known as conformal deposition. In contrast, plasma etching is an anisotropic technique, removing materials preferentially in the direction perpendicular to the surface. Therefore, by depositing a material that has a different etching rate than the sacrificial layer and directionally etching the material on the top of the step, the sacrificial layer can be removed selectively, leaving only the material deposited on the sacrificial structure sidewall. Thus, the feature size generated is determined by the thickness of the deposited material not by the photolithography, but the pattern pitch is determined by the minimum feature size obtainable with photolithography. Because the thickness of the deposited film can be controlled to 10 nm or less with high precision, this method is capable of generating nanopatterns far smaller

than possible by optical lithography. In this way we have batch-fabricated sub-20 nm Si wires from 250-nm patterns generated DUV photolithography (Figure 5.1b and 5.1c).

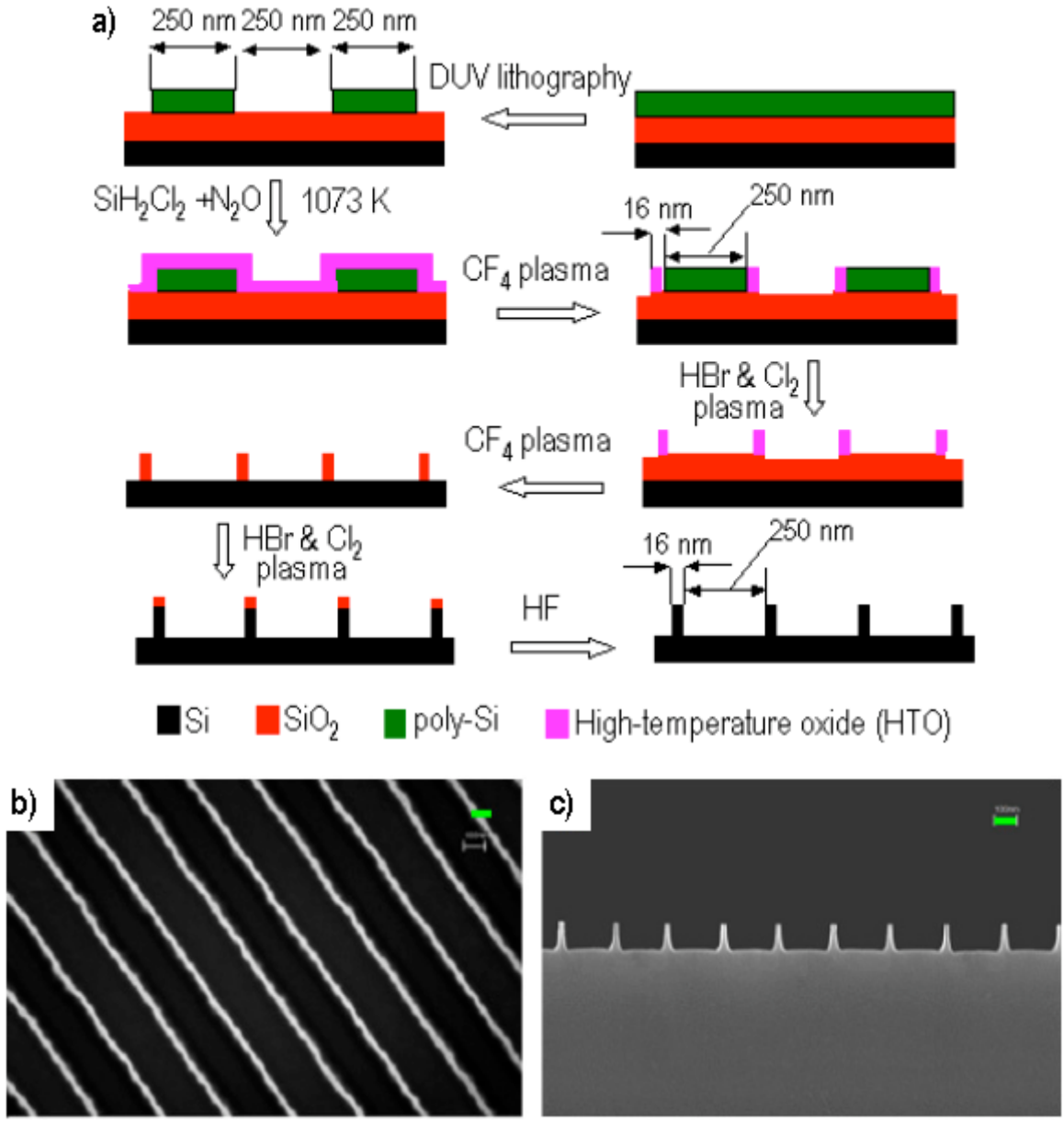

Figure 5.63: (a) Schematic of the spacer lithography process. (b) and (c) SEM top and cross-section views of the final nanostructures, which are used as an imprint mold. The mold of Si wires has features of 16 nm wide and 110 nm high with 250-nm pitch. The green bar is 100 nm.

5.3.1.2 Fabrication of Pt Nanowires by Nanoimprint Lithography (NIL) and Characterization

The single crystalline Si nanowire structures fabricated by SRL are used as a mold for producing high surface area Pt wires by nanoimprint lithography. The NIL process is shown schematically below in Figure 5.2. Si(100) wafers covered by 100-nm oxide thin films are used as imprinting substrates, and the oxide thin films become the eventual supports for the Pt wires. The silica substrate is prepared by wet-oxidation ($H_2O_{(g)}$) of Si(001) at 1173 K. Alumina, zirconia and ceria oxide films are deposited onto native oxide covered Si(001) surfaces by electron-beam evaporation at a rate of 0.2 nm/s. The e-beam evaporator has a base-pressure $1x10^{-6}$ Torr and a beam collimation of ~5mrad. After deposition, the oxides are annealed at 1173 K for 4 h under oxygen ambient. Stoichiometric Al and Zr oxides are formed after oxygen annealing, but Ce suboxide (CeO_x) is revealed by XPS (not shown). Then PMMA thin films are spin-cast on the desired oxide surfaces. PMMA (M_w = 15k) is dissolved in toluene at room temperature and kept in the solvent for 24 hours to ensure complete dissolution of the PMMA. Before use, the solution is filtered by a 0.2 □m PTFE filter to remove undissolved polymer particles. Then, the solution is ultra-sonicated for 3 hours to remove any dissolved gas. The film thickness is controlled by both the PMMA concentration and spin rate. A typical 160-nm thick film is obtained by spincasting an 8%, by mass, PMMA solution in toluene at 5600 rpm for approximately 30 s. Immediately after a film is spin-cast, it is baked at 423 K for 5 min. to evaporate all residual solvent from the polymer layer. It is then cut to the size of the Si mold.

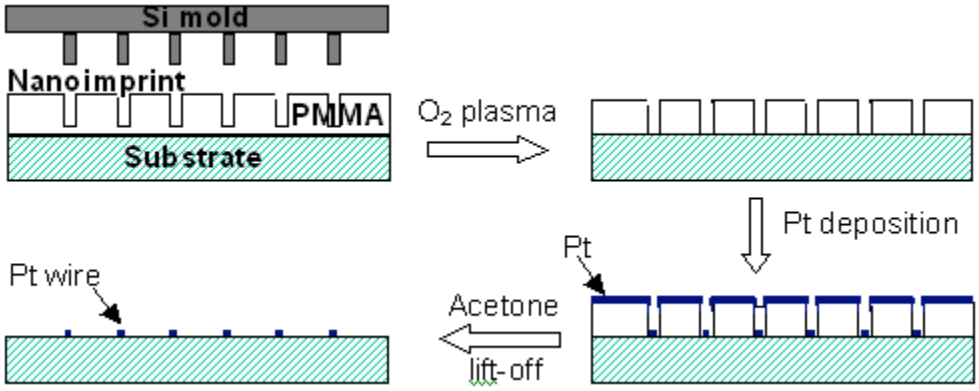

Figure 5.64: Schematic of nanoimprint lithography process

To facilitate the separation of the mold and PMMA-coated substrate after imprinting, the surface of the Si mold is functionalized by tridecafluoro-1,1,2,2-tetrahydrooctyl-1-trichlorosilane (FTS) to form a fluorine terminated self-assembled monolayer (SAM) before use. To form the SAM layer, the mold is first cleaned in piranha solution (98% H_2SO_4 + 30% H_2O_2) at 393 K to remove the organic contaminants, during which a thin layer of surface oxide and silanol groups form. Then the cleaned mold is transferred into an oven filled with 2 mTorr FTS at 363 K for 300 s. Water contact angle measurements show an angle larger than 105°, which verifies that the surface is functionalized. Functionalizing the surface lowers the surface energy and allows more facile separation of the mold from the PMMA-covered substrate.

Finally, the substrate and the mold, covered by PMMA and FTS respectively, are brought into close contact. Up to this step, all processes are performed in a class-100 clean room environment to avoid possible dust contamination, which may ruin the conformal contact between the substrate and the mold. The samples are imprinted under 4000 PSI at 393 K for 300 s using a home-made hydraulic press[12]. The imprint cell (= 64 mm) is heated resistively from room temperature to the imprinting temperature at

ramp rate 2 K/min. The cell is vacuum-pumped by a mechanical pump to evacuate the vapors that the sample outgases during heating and pressing. After the imprint, the sample is air-cooled to room temperature under pressure, and the substrate and mold are separated manually.

The top-view SEM image of an imprinted PMMA film is shown above in Figure 5.3a. The width of the trenches is about 2 nm larger than the dimension of the original Si wires. It is believed that the broadening is not the result of the imprinting process but the FTS SAM cover layer. Cross-sectional SEM (not shown) of the as-imprinted sample shows that there is still residual PMMA at the bottom of the imprinted trenches, which is eliminated by anisotropically etching the substrate in O_2 plasma. Due to an isotropic contribution to the PMMA etching, i.e., the etching is not perfectly perpendicular to the substrate, the trench width in the PMMA is increased by a few nanometers. The broadening caused by the isotropic etching can also be utilized to produce different width Pt wires, and even bimodal size distribution wires[13]. After the residual PMMA is removed, platinum is deposited at a rate of 0.1 nm/s by e-beam evaporation. The Pt that is in contact with only PMMA is lifted-off by acetone assisted with ultrasonication as shown in Figure 5.2, and the Pt deposited through the imprinted pattern and onto the silica forms nanowires (Figures 5.3b-d). The width of Pt wires is controlled by the initial silicon wire width in Figure 5.1b,c, and by the isotropic etching effect during O_2 plasma breakthrough of PMMA. The height of Pt is controlled by the thickness of deposited Pt, which is monitored *in situ* by a crystal oscillator and calibrated by atomic force microscopy. The upper limit is quarter of the depth of the imprinted PMMA trenches (~25 nm). A Pt film thicker than this will cause difficulties during the PMMA lift-off.

The lower limit of the wire height is determined by the sensitivity of the crystal oscillator (0.1 nm), which gives a sub-monolayer Pt film. Using the same techniques, 20-nm wide 5-nm high Pt wires are fabricated on alumina, zirconia and ceria surfaces (Figures 5.4a-c). XPS spectra were taken to verify the oxide support and that platinum was successfully deposited (Figure 5.5). Characteristic oxide and platinum peaks were assigned.

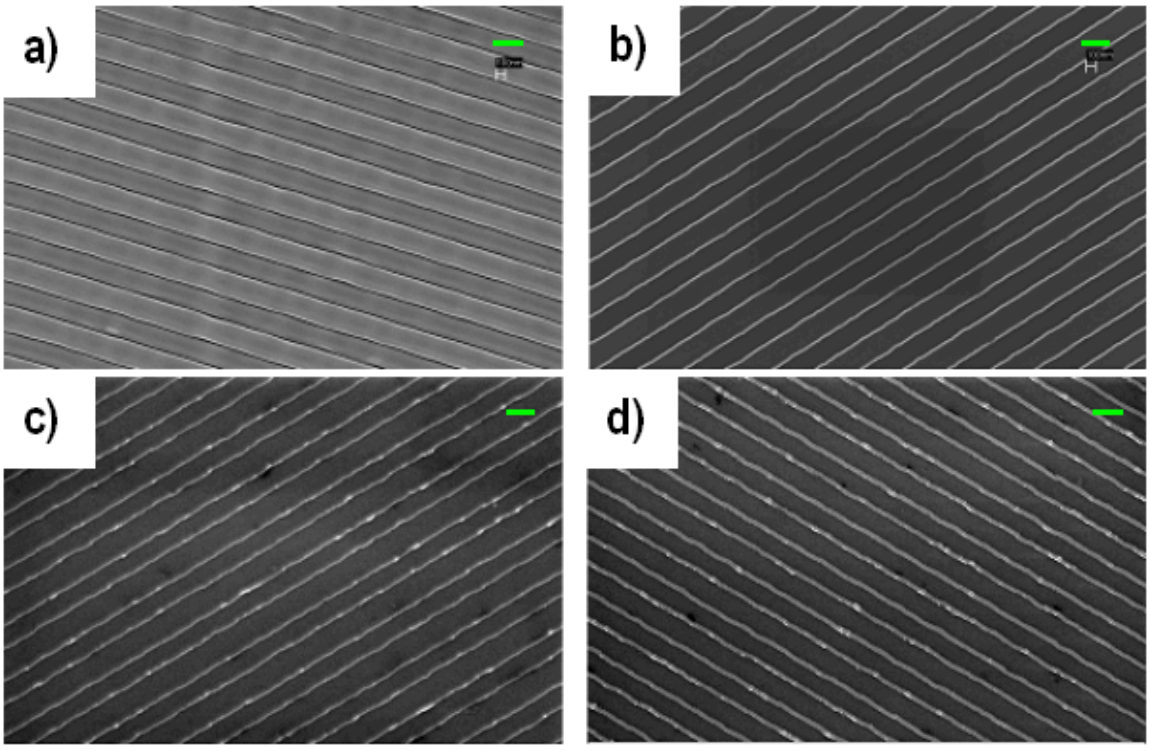

Figure 5.65:(a) SEM top-view of the negative nanostuctures in PMMA resist as-imprinted. The trench width (18 nm) is slightly larger than the wire width on the original (16 nm). (b) to (d) SEM top-view of the Pt nanowires with widths of 20, 26 and 40 nm, respectively. All nanowires are supported on a thin film (100 nm) of silica. The wire height can be easily controlled by deposited Pt thickness. The green bars are 300 nm.

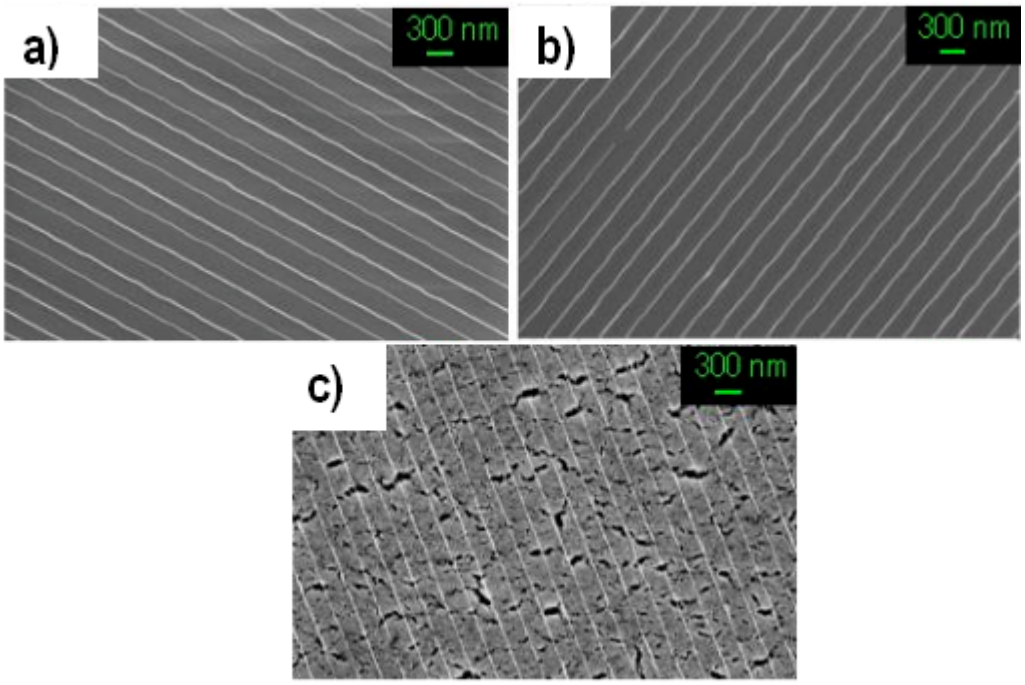

Figure 5.66: SEM images of 20-nm wide Pt nanowires on different oxide supports. All wires have 5-nm height. (a) alumina support; (b) zirconia-support; (c) ceria-support.

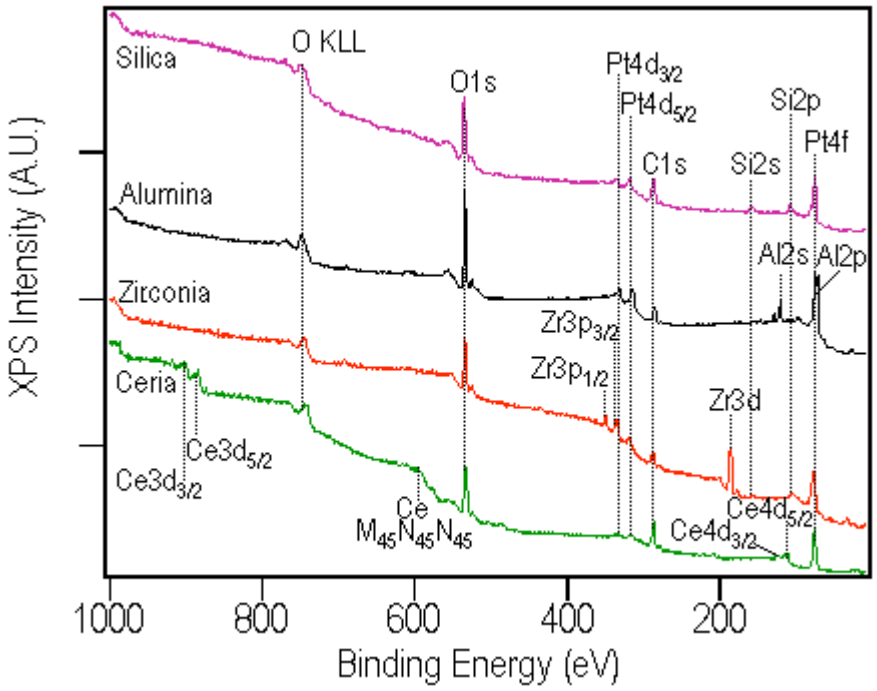

Figure 5.67: X-ray photoelectron spectra (XPS) of 20-nm Pt wires as-fabricated on various oxide supports. From top to bottom, the supports are silica, alumina, zirconia and ceria.

5.3.2 Characterization

Pt nanoarrays were characterized by scanning electron microscopy (SEM), atomic force microscopy (AFM), and x-ray photoelectron spectroscopy (XPS). SEM images are taken with a JEOL JSM-6340F equipped with a cold field emission source operating between 3 kV and 10 kV with a probe current of 12 □A. All SEM images are acquired using an E-T combined backscatter and secondary electron detector at a working distance of 6 mm. Typical SEM images of the samples used for reaction and annealing studies are shown above in Figures 5.3b and 5.4a-c. AFM is used to determine the height of the platinum features and to verify the periodicity of the arrays. AFM images (not shown) of the nanowire arrays are taken on a Park Scientific Instruments, M5 AFM. The AFM uses a feedback loop between a scan piezo and a position-sensitive photodiode array at a constant force to monitor the reflected laser light from the backside of the cantilever. XPS spectra are taken to analyze the chemical composition of the surface after fabrication and after annealing studies. Spectra are taken on a 15-kV, 40-Watt PHI 5400 ESCA/XPS system equipped with an Al anode x-ray source. Samples are cleaned of any foreign particulates before being analyzed with a stream of nitrogen gas. The spectra are inspected for the Pt $4f_{7/2}$ and $4f_{5/2}$ peaks to verify that platinum had been deposited. As well, the spectra verify the presence of the characteristic Zr, Ce, Si and Al peaks for each of the oxide substrates (Figure 5.5). For the annealing study, the XPS peaks were fit using XPS PEAK 4.1, which employs a least-squares fitting method. A Shirley background subtraction was used and Gauss-Lorentz peak fitting. Known powder references were used for comparison. As there was silicon migration seen through the oxide support from the silicon wafer, in some cases, and further support oxidation in

other cases, Pt peak signals were compared to the signal of peaks from all elements in support (oxide support and Si signals). The difference of the ratios between the peaks was taken after different treatments (annealing or reaction) for comparison.

5.3.3 Reaction Apparatus

The reaction studies are carried out in an ultrahigh vacuum (UHV) equipped with a high-pressure cell. The general design of this type of chamber has been described in Chapters 2 and 3. The outer chamber achieves a bakeout pressure of 1×10^{-10} torr and a working pressure of 1×10^{-9} torr between reactions. The chamber was evacuated by use of a turbomolecular pump (Balzers TPU 330), and an ion pump (Varian). The sample is mounted on a boronitride heater (Advanced ceramics, HT-01) with aluminum clips and gold-plated stainless steel screws to minimize background reaction. The sample temperature is measured with a 0.010 in. K-type thermocouple clamped to the sample with an aluminum clip and an alumina spacer. The alumina spacer is used to avoid electrical contact between the heater and the thermocouple. The sample is initially cleaned by two cycles of 1×10^{-6} Torr NO_2 at 573 K for 30 min, to oxygenate carbonaceous contaminants from the platinum surfaces, and annealed under vacuum at 1023 K for 5 min. The silica-supported sample was not stable upon annealing to this temperature, and a new sample was run without annealing. For this reason, the alumina sample was not annealed either, but further annealing studies showed alumina-supported to be stable at 773 K. The annealing at 773 K cleaned the sample as well, so this method of cleaning was employed for the alumina-supported sample. Between reaction runs, the surface is cleaned by dosing 1×10^{-6} Torr NO_2 at 573 K for 20 min. This NO_2 treatment leaves atomic oxygen on the surface, and thus is equivalent to a pre-adsorption of oxygen

onto the platinum surface. The sample cleanliness is verified by AES. All Auger spectra are taken using a Physical Electronics Industries, Inc. Auger system. As the Auger process itself can deposit carbon impurities on the surface of the sample, the sample is always cleaned after any Auger spectra are taken.

5.3.4 CO Oxidation Reaction Studies

Every sample is cleaned as described above before introducing reaction gases. Catalytic studies are carried out on all catalyst samples using 40 torr CO, 100 torr O_2, and 620 Torr He gas. Gases are premixed in the gas manifold approximately 20 minutes before introduction to the catalyst and the reaction line (during NO_2 cleaning). Upon completion of the NO_2 dosing, the reaction gases are introduced into the reaction loop. In the reaction loop, the gas mixture consists of 100 Torr O_2, 40 Torr CO, and 620 Torr He. The purities of O_2, CO, and He gases used in reaction studies are 99.997, 99.99, and 99.9999%, respectively. All gases are used as received from Airgas without further purification. The gases are circulated through the reaction line by used of a Metal Bellows recirculation pump at a rate of 2 L/min. The volume of the reaction loop is 0.225 L. A HP Series II gas chromatograph (GC) equipped with a TCD detector and a 15’ □ 1/8” SS 60/80 Carboxen-1000 (Supelco) is used to separate the products for analysis. The GC is part of the reaction loop and samples the circulating reaction gases every 5 minutes by use of a 6-port automatic sampling valve. The measured reaction rates are reported as turnover frequencies (TOF) and are measured in units of product molecules of CO_2 produced per platinum surface site per second of reaction time. The number of platinum sites is calculated by geometrical considerations. The nanowires walls are considered to be rectangular and standing upright on a planar support. By using SEM

measurements to calculate the surface area of a wire and dividing by the surface density of platinum, the number of surface platinum sites available for reaction is calculated.

5.3.5 Annealing Studies of the Pt Nanowire Arrays

Separate samples of the nanowire arrays are cut from the Pt arrays before any reaction has taken place and are used for annealing studies. A sample of Pt nanowires on each oxide is annealed at 773 K and 973 K separately, which is to say that there are two samples to anneal of each oxide. Each sample is either heated to 773 K or 973 K, but this is not done sequentially. The samples are heated in a quartz tube furnace under a 100 sccm flow of He gas. The total He pressure in the tube furnace is 760 torr, while flowing gas. SEM images are taken of each oxide-supported array after the two thermal treatments and compared to the SEM images before treatment. Additionally, XPS spectra are taken of these samples before and after thermal treatment to qualitatively monitor the change in the Pt 4f peak in comparison to the peaks from the oxide support.

5.4 Results

5.4.1 CO Oxidation Reaction Studies

Catalytic oxidation of CO to CO_2 over the various catalyst arrays was carried out in the 513-613 K temperature range, which is above the ignition temperature. Above the ignition temperature, CO oxidation is a surface insensitive reaction meaning that it will display similar kinetics under similar reaction conditions. In this regime, the reaction rate is mass-transport limited. For this reason, the measured activation energies will be compared to the literature rather than the measured turnover frequencies (TOF) of reaction, because different flow rates and reactor volumes can change the turnover rate measured for a given system. However, the reaction turnover for all arrays are discussed

in general and compared to gauge the reactivity of all supported arrays in comparison to one another. A summary of the measured activation energies is shown in Table 5.1 for all of the supported catalysts. These values are shown in comparison to Pt(111)[14,15] and a 15-nm Pt thin film deposited onto a Si(100) wafer with native oxide. A typical CO_2 accumulation curve is shown in Figure 5.6. The accumulation curves yield the rate of reaction at different temperatures and using this information, Arrhenius plots are constructed to obtain the apparent activation energy of reaction. The Arrhenius plots for reaction on the zirconia and ceria-supported samples is shown in Figure 5.7 and the Arrhenius plots for the alumina and both silica-supported samples (annealed and unannealed previous to reaction) are shown in Figure 5.8. The Arrhenius plots for reaction on the 15-nm Pt film on silicon is shown in Figure 5.9.

Table 5.6: Summary of measured activation energies for CO Oxidation

Catalyst	E_a (kcal/mol)
Pt (111)	14 (A.I) & 42 (B.I)
15-nm Pt thin film on Si(100) wafer	13.7 ± 0.4 (A.I) 26.9 ± 0.1 (B.I)
Nanowires on SiO_2 No Annealing	15.9 ± 0.6
Nanowires on SiO_2 Annealing at 1023 K	12.6 ± 0.2
Nanowires on CeO_2	18.8 ± 0.2
Nanowires on Al_2O_3	17.1 ± 0.4
Nanowires on ZrO_2	14.6 ± 0.2

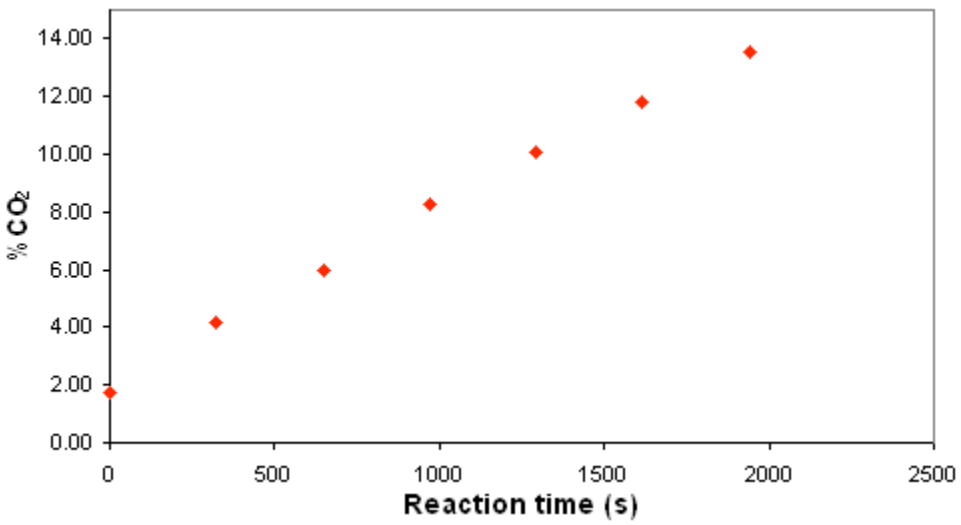

Figure 5.68: CO_2 accumulation curve measured on a zirconia-supported platinum nanowire array at 553 K.

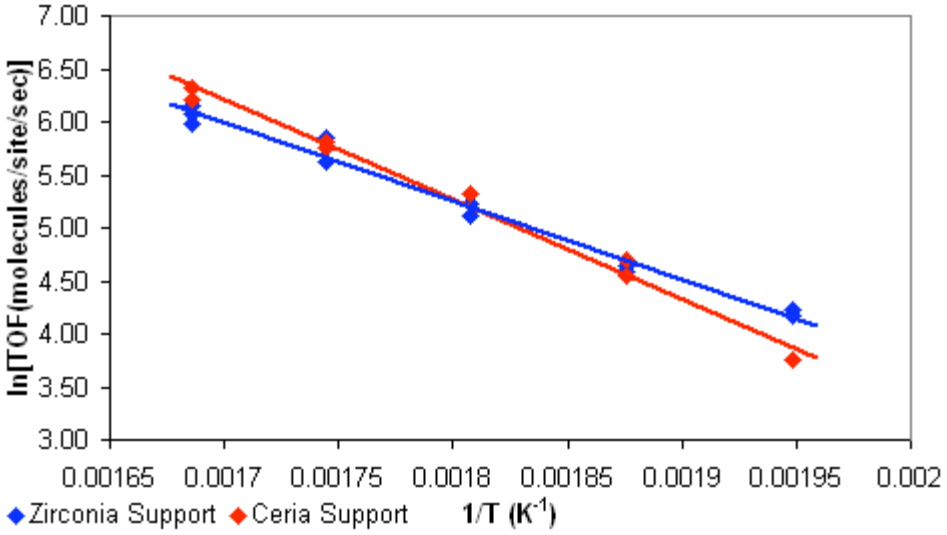

Figure 5.69: Arrhenius plots measured for CO oxidation reactions on zirconia and ceria-supported Pt nanowire arrays

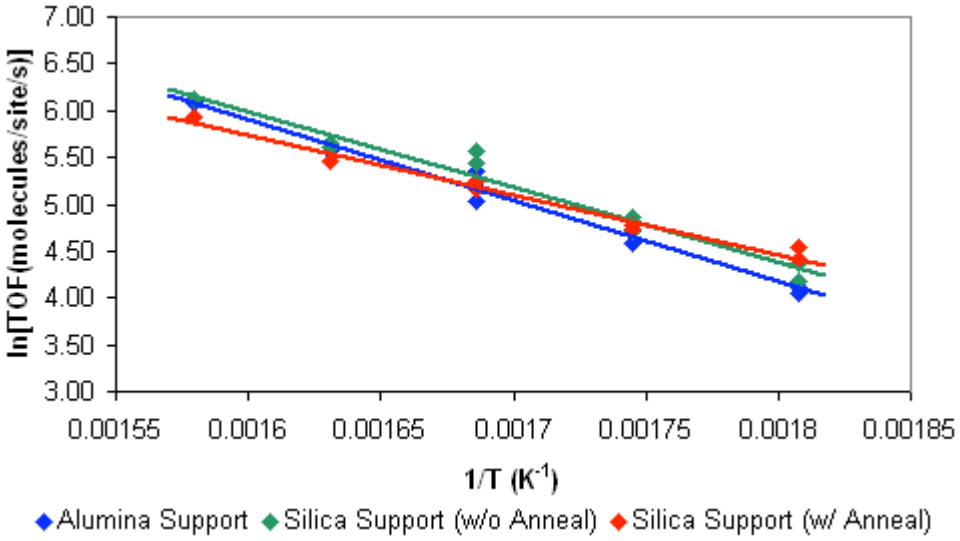

Figure 5.70: Arrhenius plots measured for CO oxidation reactions on alumina and silica-supported Pt nanowire arrays

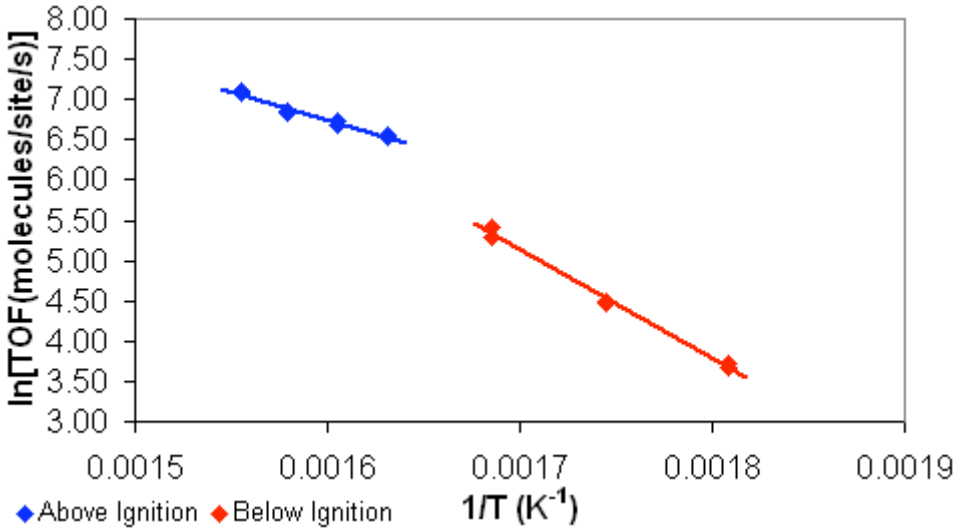

Figure 5.71: Arrhenius plots measured for CO oxidation reactions on a 15-nm platinum film supported on a Si(100) wafer

The apparent activation energy for the Pt(111) single crystal and the 15-nm Pt film on silicon, which were used as reference states of platinum, are 14 kcal/mol [14,15] and 13.7 ± 0.4 kcal/mol, respectively. The Pt thin film is also used to measure the activation energy below ignition, which was measured to be 26.9 ± 0.1 kcal/mol. Apparent activation energies for the zirconia and ceria-supported wire arrays are 14.6 ± 0.2 kcal/mol and 18.8 ± 0.2 kcal/mol, respectively. The nanowires on silica, which were

annealed at 1023 K previous to reaction, have an activation energy of 12.6 ± 0.2 kcal/mol, and the unannealed silica-supported samples have an activation energy of 15.9 ± 0.6 kcal/mol. The apparent activation energy measured on the alumina-supported sample is 17.1 ± 0.4 kcal/mol.

After CO oxidation, SEM images are taken *ex situ*, to monitor any change of the nanowire morphology (left side of Figures 5.10a-e). The zirconia and ceria-supported wires are both stable under for the cleaning and reaction studies (Figures 5.10c,e, respectively). The silica sample, which was annealed at 1023 K before reaction, is no longer a nanowire but sinters into particles of various sizes (Figure 5.10b). The alumina-supported sample while it did form particles stays in a wire form as shown in Figure 5.10d.

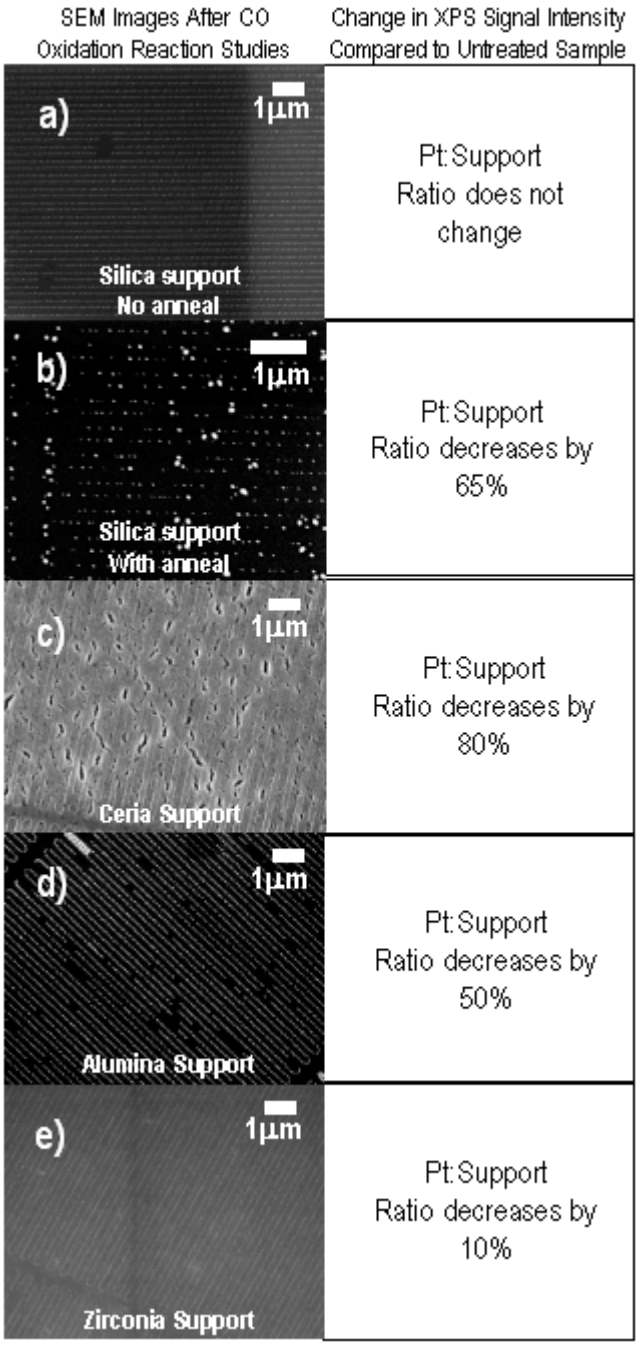

Figure 5.72: Post-reaction analysis of Pt nanowire samples (Right) SEM images (Left) Changes measured in Pt by XPS (a) Silica-supported array not annealed previous to reaction (b) Silica-supported array annealed at 1023 K previous to reaction (c) ceria-supported array annealed at 1023 K previous to reaction (d) alumina-supported array annealed at 1023 K previous to reaction (e) zirconia-supported array annealed at 1023 K previous to reaction.

As well, post-reaction XPS spectra are taken *ex situ* to observe any differences in the Pt:support signal ratio. These results are also summarized in Figures 5.10a-e (right side). The silica sample that was not annealed before reaction (Figure 5.10a), shows no change in the percentage of Pt on the surface post-reaction. On the silica-supported sample that was annealed previous to reaction at 1023 K, a decrease of 65% in the Pt:support signal ratio is measured (Figure 5.10b). The ceria-supported nanowire array shows an 80% decrease in the Pt:support ratio after reaction (Figure 5.10c). The alumina-supported wires also show a large decrease with a decrease of 50% of the Pt:support signal ratio. There is a 10% decrease is the Pt 4f signal measured for the zirconia-supported Pt wires (Figure 5.10e).

5.4.2 Annealing Studies

A piece of each nanowire array is placed in a tube furnace and annealed to 773 K in a flow of He, and separate pieces of these arrays are placed in a tube furnace and annealed to 973 K in a flow of He. These studies are done to get a qualitative picture of the thermal stability of the nanowires under different thermal conditions. SEM images for the annealing studies at 773 K and 973 K are shown in Figures 5.11 and 5.12, respectively. XPS spectra of the sample were taken before and after the annealing studies as well for comparison of the change in the ratio of signal measured from Pt and that of the support. A summary of the XPS results for the annealing at 773 K and 973 K are also shown in Figures 5.11 and 5.12, respectively.

The silica-supported wires show a 65% decrease in the Pt:support signal ratio upon annealing to both 773 K and 973 K (Figures 5.11a, 5.12a, respectively). Thus, there is a difference in comparison to the unannealed array, but both thermal environments

cause the same 65% decrease. When annealed at 773 K, there is no apparent morphology change in the wire structure. However, when annealed at 973 K, there are noticeable breaks and roughening in the wires. The Pt wires, thus, do not sinter into particles on the surface, but do show some instability.

A 25% decrease in the Pt:support signal ratio is measured for the ceria-supported wires upon annealing at 773 K and a 45% decrease is measured after annealing at 973K (Figures 5.11b, 5.12b, respectively). There are no apparent morphology changes seen in the SEM images of the wires upon annealing in either of the two temperatures.

The alumina-supported wire array also shows a difference between the two thermal treatments. Upon annealing to 773 K, no change is measured in the Pt:support signal ratio. However, a change is seen in the SEM images for annealing at this temperature. Some roughening of the wire structure is seen, and some small breaks in the wire are apparent (Figure 5.11c). When the sample is annealed at 973 K, a 70% decrease in the Pt:support signal ratio is seen. There are dark spots seen over the wires and some apparent breaks seen in the SEM images (Figure 5.12c). There is no change, however, in the measured wire diameter by SEM.

The zirconia-supported wires, show a 80% decrease in the Pt:support signal ratio when annealed at 773 K and 973 K (Figures 5.11d and 5.12d, respectively). There is no difference in the two thermal environments seen. In the SEM images, there is some roughening of the wire structure and some breaks in the wire.

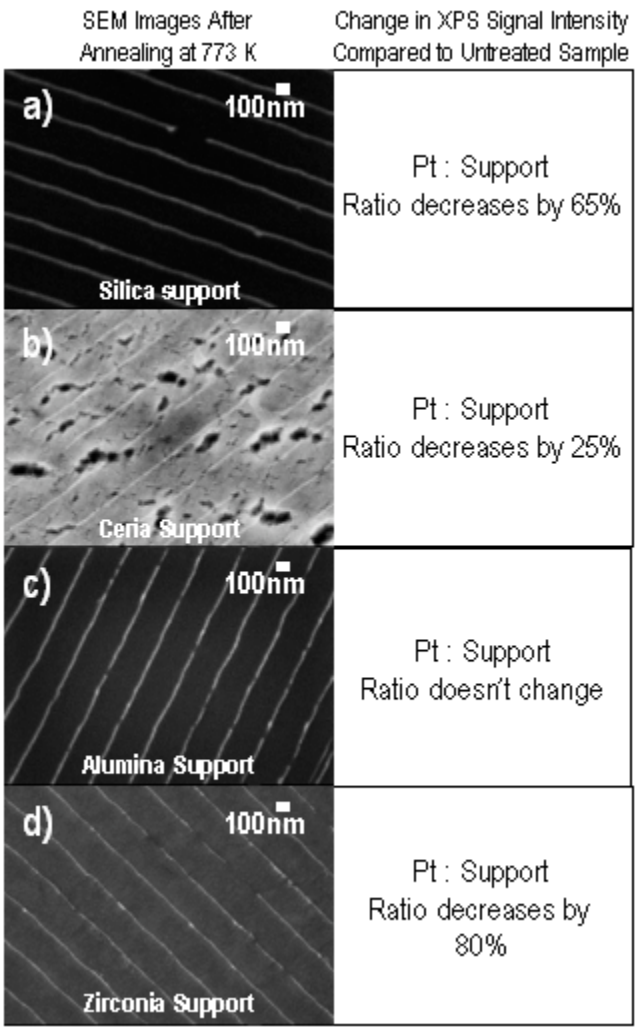

Figure 5.73: Post-annealing analysis of Pt nanowire samples (Right) SEM images (Left) Changes measured in Pt by XPS. All samples have been annealed at 773 K for two hours in He. (a) silica-supported array (b) ceria-supported array (c) alumina-supported array (d) zirconia-supported array.

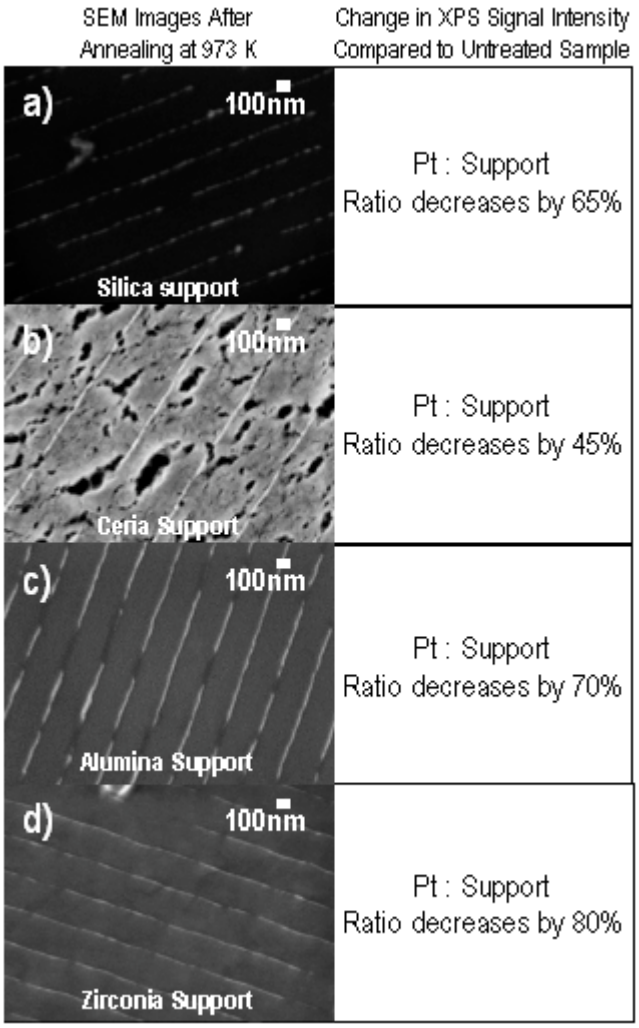

Figure 5.74: Post-annealing analysis of Pt nanowire samples (Right) SEM images (Left) Changes measured in Pt by XPS. All samples have been annealed at 973 K for two hours in He. (a) silica-supported array (b) ceria-supported array (c) alumina-supported array (d) zirconia-supported array.

5.5 Discussion

5.5.1 CO Oxidation Reaction Studies

The apparent activation energy above ignition on the Pt thin film compares well with that of the Pt(111) single crystal. Measurement of CO oxidation over the Pt thin film shows two different reaction regimes. Above ignition, the apparent activation energy is measured at about 14 kcal/mol, which is essentially the same as that measured

for the Pt(111) single crystal. Below ignition, the apparent activation energy measured for the Pt thin film is about 27 kcal/mol, with ignition occurring between 593 K and 613 K. The nanowire arrays are as well Pt thin films deposited in the same manner (electron beam evaporation), except that they are formed into structures on the planar oxide surface. This provides the nanowires with an oxide-metal interface, which adds an additional ingredient to affect reactivity.

Two separate silica-supported nanowire arrays have been used to measure CO oxidation. The first array was annealed in vacuum to 1023 K like the other arrays before reaction for five minutes. The apparent activation energy measured for this array was about 13 kcal/mol, which compares well to the 14 kcal/mol measured for the thin film and single crystal. SEM images after reaction show that the platinum wires have broken and balled up on the oxide surface (Figure 5.10b), and XPS shows a decrease of the Pt 4f signal of 65%. This can be due to several factors such as the platinum breaking up and minimizing its surface area, or the migration of platinum into the support. Figure 5.10b clearly shows that the platinum balls up and loses its wire structure on the support. As well, platinum is known to wet the silica surface and migrate into the support as shown by Yu *et.al.*[16]. In an oxygen environment, the diffusion coefficient for oxygen through silica is orders of magnitude greater than the diffusion coefficient of silicon through silica[17]. Thus, the 65% loss in the Pt signal is due to a combination of the platinum reducing its surface area by balling up on the silica and migrating into the support. The second array of silica-supported nanowires used to measure CO oxidation was not annealed in vacuum previous to reaction. The apparent activation energy measured without annealing previous to reaction was about 16 kcal/mol, which is higher than the Pt

single crystal and the thin film. In addition, it is 3 kcal/mol higher than the annealed array. It is thought that the annealing previous to reaction helps to break up any residual PMMA left after the imprint process used to fabricate the nanowires. Once the polymer backbone dehydrogenates and breaks up, it is more easily oxidized by the cleaning procedure. If some of the polymer is still on the platinum, then it may be more difficult for the reactants to adsorb or the products to desorb from the platinum surface, which would make the apparent activation energy higher for the reaction. The post-reaction SEM images of this sample (Figure 5.10a) show that the platinum wire structures are stable under reaction conditions and no decrease in the Pt 4f signal is seen by XPS. Therefore, the annealing procedure previous to reaction is the cause of the nanowire structure breaking and not the reaction conditions in oxygen ambient.

The apparent activation energy for the ceria-supported nanowire arrays is about 19 kcal/mol, which is higher than both the platinum thin film and single crystal. This is however comparable to other ceria-supported arrays[18,19], which show apparent activation energies anywhere from 8 –21 kcal/mol. This sample was annealed to 1023 K before reaction, and the wire structures remained stable despite the annealing and reaction conditions (Figure 5.10c). XPS, however indicates an 80% decrease in Pt signal after reaction in comparison to before. Despite this drop in signal, though, the ceria-supported Pt wires have over double the turnover frequency of the silica and alumina-supported wires. Hardacre *et.al.* have seen that depositing ceria on Pt(111) with different coverages can change the turnover frequency of reaction for CO oxidation and the activation energy[18]. In fact, ceria-covered Pt can turnover just as much and sometimes more than the metal on its own[18]. Since there is a drop in the platinum signal seen by

XPS after annealing and reaction, the platinum wires are most likely decorated by the ceria and continuing to turnover reaction by some Pt/Ce species or Pt/CeO_x species. While still active as reaction sites, this type of compound may make it more difficult for reactants to reach metal sites for dissociation and desorb as products. The reaction rate, however, seems to be enhanced, which can be attributed to the ability of ceria to accept and donate oxygen atoms during reaction perhaps facilitating oxidation of CO once it adsorbs on a Pt site[20-23]. Figure 5.13 shows the XPS spectra of the ceria-supported samples before and after reaction. Figure 5.13a, which shows the Pt 4f peaks before and after reaction, is typical of the samples that lose platinum after reaction. Figure 5.13b shows two peaks fitted to the spectrum in the O1s binding energy area. The lower binding energy peak is assigned to the ceria support oxygen. This does shift after reaction, which is indicative of less oxygen content in the oxide[24]. The higher binding energy peak is assigned to the O^{2-} peak associated with carbonate groups from the binding of CO and CO_2 to the ceria surface from atmosphere and during reaction[18,25].

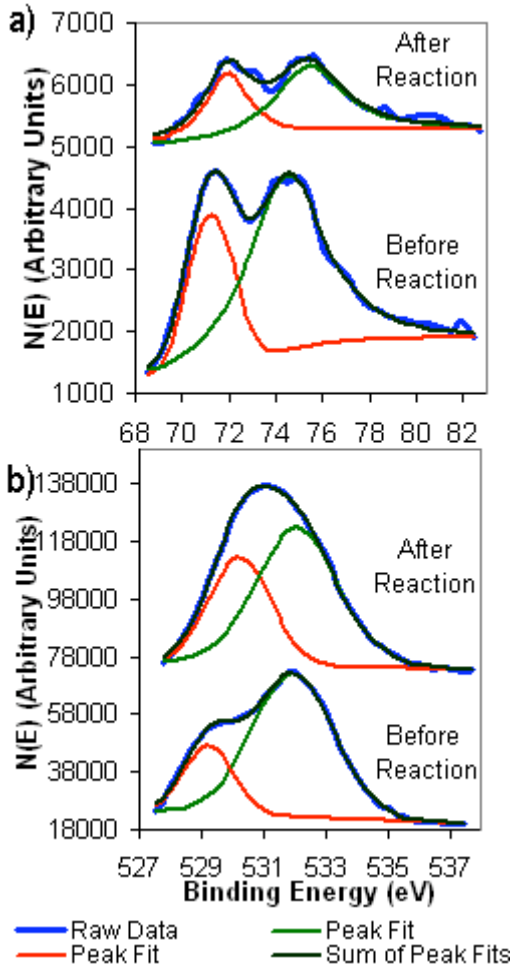

Figure 5.75: XPS characterization of the ceria-supported Pt nanowire array (a) Pt 4f peaks before and after reaction showing loss of surface platinum (b) O1s peaks before and after CO oxidation reaction showing the O^- of the carbonate groups from CO and CO_2 groups binding to the ceria surface.

The apparent activation measured on the alumina-supported array was 17.1 kcal/mol. This is 3 kcal/mol higher than for the Pt(111) single crystal and thin film. However, it is considerably lower than other values seen for Pt/Al_2O_3 ranging from 26 to 41 kcal/mol[19,26]. It is seen that the apparent activation energy is sensitive to the structure of the alumina onto which the Pt is deposited[26]. This sample was annealed at 773 K before reaction in vacuum, and it appears that the reaction conditions cause the Pt wires to break and create Pt particles (Figure 5.10d). Post-reaction XPS measurements

show a 50% decrease in the Pt 4f signal. This decrease in the Pt surface area is similar to that of the silica-supported case in that the decrease is most likely caused by the balling up of the Pt and the migration of the Pt into the support[27]. As well, there is a 90% increase in the Si to Al peak ratio after reaction, which means that there is significant Si migration through the alumina support. Thus, there could also be platinum silicides forming, which are not catalytically active and would reduce the number of active metallic sites available for reaction.

CO oxidation measured on the zirconia-supported nanowire array gives an apparent activation energy of about 14.6 kcal/mol, which is very close to the values measured on the Pt single crystal and thin film. The nanowire structures seem to be stable after annealing at 1023 K in vacuum and the reaction studies (Figure 5.10e). Post-reaction XPS measurements show the Pt signal decrease by 10% and the Si to Zr peak ratio increase by 50%. The fact that the Pt signal does not decrease significantly is the most likely reason that this array has as high of a turnover frequency as the ceria support. A comparison of reaction turnover rates is shown below in Table 5.2. In Table 5.2a, the turnover is calculated using the number of platinum sites calculated from SEM measurements on the samples before reaction. In Table 5.2b, the turnover is calculated using SEM measurements and taking into account the amount of surface platinum lost according to post-reaction XPS measurements. Since the measured turnover frequencies are reproducible, it is thought that any platinum lost is mostly due to the pre-reaction annealing at 1023 K in vacuum, but the TOF is calculated in both manners because XPS measurements were taken *ex situ* after reaction. However, the measured TOF's show the same trend regardless of how they are calculated. The ceria and zirconia-supported

arrays have the highest turnover rates of the four arrays, and of these two arrays ceria turns over about 40% more if the platinum lost during reaction is taken into account. It is believed that the reason the zirconia-supported array has such a high TOF is due to the stability of platinum throughout the reaction studies. The ceria-supported array shows a similar TOF to the zirconia-supported array, but has an 80% decrease in the amount of surface platinum. Thus, the TOF is likely due to the strong metal-support interaction of the ceria-decorated platinum surface. Both the alumina and silica-supported arrays had lower turnover and showed significant decrease in the platinum signal. In both arrays, there is the possibility of platinum migrating into the support, which is the likely cause of the lower turnover.

Table 5.7: a) Turnover frequency calculated from SEM measurements on as-prepared samples. b) Turnover frequency calculated with the number of Pt sites adjusted to reflect the percentage of platinum sites lost as measured post-reaction by XPS.

Catalyst	a) TOF at 573 K (molecule/site/s)	b) TOF at 573 K (molecules/site/s) XPS-Considerations
Nanowires on SiO_2 No Annealing	120	120
Nanowires on SiO_2 Annealing 1023 K	116	191
Nanowires on CeO_2	325	585
Nanowires on Al_2O_3	111	167
Nanowires on ZrO_2	311	342

5.5.2 Annealing Studies

The silica-supported samples annealed at 773 K and 973 K in He both show a decrease in Pt signal of 65%. This is the same decrease measured after annealing in vacuum at 1023 K and using the array in reaction studies. There is, however,

significantly more breaks in the wires after annealing at 973 K in comparison to annealing at 773 K (Figures 5.11a and 5.12a, respectively). Neither of these thermal environments causes the platinum to ball up to the extent seen after the reaction studies (Figure 5.10b). Thus, there is additional platinum mobility seen in oxidative environments, but the platinum loss seems to be from the thermal treatment, which is indicative of platinum diffusing into the oxide support as mentioned above.

The ceria-supported nanowire arrays show a 25% decrease in Pt by XPS upon annealing at 773 K in He and a 45% decrease in Pt upon annealing at 973 K in He. In both of these thermal environments (773 K and 973 K annealing), the platinum nanowire structures are stable (Figures 5.11b and 5.12b, respectively). The platinum decrease in these thermal environments is significantly less than the 80% decrease seen upon annealing at 1023 K in vacuum and using the array for reaction studies. The oxygen ambient used in reaction studies may enhance the ability of the oxide to decorate the platinum surface, which would lower the amount of platinum on the surface more than annealing in He.

Upon annealing the alumina-supported wire samples at 773 K, there is no change seen by XPS in the platinum signal, but there are some small breaks seen in the Pt wires by SEM (Figure 5.11c). Before reaction studies, this sample was annealed at 773 K in vacuum, because annealing in He didn't show any significant changes in the array. However, post-reaction measurements by SEM and XPS show balling up of the platinum in the wires and a 50% decrease in the amount of platinum (Figure 5.10d). Thus, just as in the case of the silica-supported arrays, there is additional platinum mobility on the oxide support in the oxidative environment of the reaction studies. Annealing at 973 K

causes a 70% decrease in the platinum signal by XPS measurements, and SEM images show dark spots in the wires, which could be caused by platinum migration into the support. After reaction, there is a 90% increase in the amount of Si in the support surface (in comparison to Al), and after annealing in He at 773 K and 973 K, there is an increase in Si of 10% and 50%, respectively. Since, there is no balling up of the platinum in the annealing studies, the mobility of platinum during reaction studies may be due to the additional Si migrating to the surface.

The zirconia-supported nanowire arrays show an 80% decrease in the Pt 4f signal after annealing to both 773 K and 973 K. SEM images show no major differences in the two thermal treatments, however (Figures 5.11d and 5.12d, respectively), with only small breaks in the wires seen. The fact that there was only a 10% decrease seen in XPS measurements, after annealing at 1023 K in vacuum and using the array for reaction studies, suggests that the oxygen ambient present in the reaction studies stabilize the array and allow for the platinum to be available for reaction. This can perhaps be better understood by looking at the increase in the silicon content of the surface upon annealing. Both annealing at 773 K and 973 K gives an increase of Si in the surface of 80%, but post-reaction measurements only show an increase of 50%. The oxidative atmosphere available during reaction can result in oxygen diffusion through the support and oxidize the silicon before it reaches the surface, which would allow less platinum to be lost by formation of silicides. Zirconium has shown the capability of transferring oxygen to other elements such as cerium in supports[28] and in this case may be transferring oxygen to Si as it diffuses through the zirconia support.

The oxidative atmosphere is not the only difference between the thermal treatments in He and annealing in vacuum followed by reaction studies. It must also be considered that while the samples used for reaction studies were heated at a lower temperature during reactions, it was for a longer overall time period. This could also contribute to the differences seen.

The use of lithography for fabrication of two-dimensional nanoarrays as model catalysts offers the opportunity to change different aspects about the catalyst while holding all other features the same. These investigations into the reaction kinetics of CO oxidation and platinum nanowire array thermal stability indicate that reaction rates, activation energies, and thermal stability have a large dependence on support. Future work with such well-defined systems can be furthered by controlling diffusion through the oxide supports and using single-crystalline oxide surfaces to help unravel even further the importance of the specific support with the metal structure.

5.6 Summary

DUV has been coupled with NIL to produce sub-20 nm platinum nanowire arrays on oxide supports of silica, alumina, ceria and zirconia. These two-dimensional model catalyst arrays have been used to study the support dependence of CO oxidation reaction kinetics and indicate that the most important factor affecting turnover frequency is the interaction of the platinum and the support, while the activation energy is most heavily affected by clean platinum being on the surface of the oxide. Further studies with oxide supports of controlled surface structure can help to balance these two factors and truly tune the catalyst to the reaction.

References

1. N.W. Cant, P.C. Hicks, B.S. Lennon, *J. Catal.*, 54, **1978**, 372.
2. N.W. Cant, D.E. Angove, *J. Catal.*, 97, **1986**, 36.
3. J.T. Kiss, R.D. Gonzalez, *J. Phys. Chem.*, 88, **1984**, 892.
4. J.T. Kiss, R.D. Gonzalez, *J. Phys. Chem.*, 88, **1984**, 898.
5. J.T. Kummer, *J. Phys. Chem.*, 90, **1986**, 4747.
6. C.H.F. Peden, D.W. Goodman, D.S. Blair, P.J. Berlowitz, G.B. Fisher, S.H. Oh, *J. Phys. Chem.*, 92, **1988**, 1563.
7. B.D. Gates, Q. Xu, J.C. Love, D.B. Wolfe, G.M. Whitesides, *Annu. Rev. Mater. Res.* **2004**, *34*, 339.
8. S.Y. Chou, P.R. Krauss, P.J. Renstrom, *Science* **1996**, *272*, 85.
9. L.J. Guo, *J. Phys. D: Appl. Phys.*, **2004**, *37*, R123-R141.
10. Y.K. Choi, J.S. Lee, J. Zhu, G.A. Somorjai, L.P. Lee, J. Bokor, *J. Vac. Sci. Tech. B* **2003**, *21*, 2951-55;
11. Y.K. Choi, J. Zhu, J. Grunes, J. Bokor, G.A. Somorjai, *J. Phys. Chem. B* **2003**, *107*, 3340;
12. J. Zhu, Ph.D. Dissertation, Chapter 5, University of California at Berkeley, 2003.
13. X.-M. Yan, S. Kwon, A.M. Contreras, J. Bokor, G.A. Somorjai, *Nano Lett.* **2005**, *5*, 745.
14. X. Su, P.S. Cremer, Y.R. Shen, G.A. Somorjai, *J. Am. Chem. Soc.*, **1997**, *119*, 3994-4000.
15. K.R. McCrea, J.S. Parker, G.A. Somorjai, *J. Phys. Chem. B.*, **2002**, *106*, 10854-10863.

16. R. Yu, H. Song, X.-F. Zhang, P. Yang, *J. Phys. Chem. B*, **2005**, *109*, 6940-6943.

17. M.J. Madou, *Fundamentals of Microfabrication: The Science of Miniaturization, Second Edition*, CRC Press, New York, 2002.

18. C. Hardacre, R.M. Ormerod, R.M. Lambert, *J. Phys. Chem*, **1994**, *98*, 10901-10905.

19. U. Oran, D. Uner, *Appl. Cat. B*, **2004**, *54*, 183-191.

20. Y.-F. Yao, *J. Catal*, **1984**, *87*, 152-162.

21. J.Z. Shyu, K. Otto, W.L.H. Watkins, G.W. Graham, R.K. Belitz, H.S. Gandhi, *J. Catal.*, **1988**, *114*, 23-33.

22. Shyu, J.Z.; Otto, K. *J. Catal.*, **1989**, *115*, 16-23.

23. R.F. Hicks, C. Rigano, B. Pang, *Catal. Lett.* **1990**, *6*, 271-280.

24. G. Praline, B.E. Koel, R.L. Hance, H.-I. Lee, J.M. White, *J. Elect. Spect. and Rel. Phen.*, **1980**, *21*, 17-30.

25. L. Osterlund, S. Kielbassa, C. Werdinius, B. Kasemo, *J. Catal.*, **2003**, *215*, 94-107.

26. G.S. Zafiris, R.J. Gorte, *J. Catal.*, **1993**, *140*, 418-423.

27. J. Libuda, M. Baumer, H.-J. Freund, *J. Vac. Technol. A*, **1994**, *12*, 2259-2264.

28. F. Dong, A. Suda, T. Tanabe, Y. Nagai, H. Sobukawa, H. Shinjoh, M. Sugiura, C. Descorme, D. Duprez, *Catal. Today*, **2004**, *93-95*, 827-832.

Chapter 6

Creation of a Parallel Fabrication Process to Fabricate Nanoparticles with Tunable Size and Spacing for Future Surface Science and Catalysis Studies

6.1 Abstract

Using low-pressure chemical vapor deposition of silicon dioxide, we have reduced the size of 56-nm features in a silicon nitride membrane, called a stencil, down to 36 nm. Sub-50 nm, uniformly-sized nanoparticles are fabricated by electron beam deposition of Pt through the stencil mask. The particle pattern replicates that of the stencil. Repositioning of the stencil mask in between two consecutive Pt deposition cycles led to double the density of the original pattern. More complicated patterns can be generated by multiple depositions. A self-assembled monolayer (SAM) of tridecafluoro-1,1,2,2-tetrahydrooctyl-1-trichlorosilane was used to prevent Pt clogging of the nano size holes during deposition, as well as to protect the stencil during the post-deposition Pt

removal. X-ray photoelectron spectroscopy shows that the SAM protects the stencil efficiently during this post-deposition removal of Pt.

6.2 Introduction

Nanofabricaton of ever-smaller structures is the cornerstone of the pursuit of nanoscience and technology. Sub-50 nm features are commonly fabricated by electron beam lithography[1] (EBL) and focused ion beam lithography[2] (FIB). However, these techniques are expensive and have low throughput due to their sequential nature. Thus, there is great motivation to develop alternative lithographic methods, which have batch fabrication capability. Deep and extreme ultraviolet lithographies (DUV λ=248 nm and 193 nm and EUV λ=13.5 nm) are built upon conventional optical lithography and benefit largely from decades of its technological development[3]. 70-nm features have been successfully printed using DUV lithography[4]. However, there are still tremendous difficulties, especially in developing proper optical elements, masks and photoresists, before sub-50 nm resolution can be achieved. These difficulties have fueled the search for high-throughput patterning methods other than optical lithographies. One method is the direct deposition of materials through a pre-patterned mask. This mask can be fabricated by utilizing EBL or DUV and reactive ion etching techniques to pattern a thin silicon nitride membrane. This patterned membrane, often called a stencil, can then be supported above the desired substrate for direct deposition of materials through the stencil and onto the underlying substrate.

The most common method of silicon nitride mask fabrication is EBL due to its high resolution (sub-10 nm), but this method is unattractive due to its sequential nature.

However, batch fabrication can be realized by DUV coupled with a method to reduce the printed feature size (70-nm) on these silicon nitride membranes. In this letter, the reduction of the feature size in a silicon nitride stencil from 56 nm to 36 nm by silicon dioxide low-pressure chemical vapor deposition (LPCVD) is demonstrated. Using the stencil as a mask, platinum nanoparticles were deposited onto a native oxide surface by electron-beam evaporation[5]. The patterned metal nanoparticles can serve as model catalysts to study reaction rates and chemical selectivity[6,7]. Translation of the stencil with respect to the surface between two deposition cycles is demonstrated as a manner in which to double the density of the original pattern. To generate more complicated patterns, an iterative step-deposition can be performed[8-10]. The deposited Pt patterns can also serve as a hard mask for plasma etching to transfer the pattern into substrates[11]. Cleaning of the silicon nitride stencil after Pt deposition, which enables its use for sequential depositions, is also detailed further in this Chapter.

6.3 Fabrication and surface modification of silicon nitride stencil

6.3.1 Fabrication of SiN stencils

Low-stress (i.e. non-stoichiometric) SiN membranes (50-nm thick) with various hole-sizes were fabricated using standard wet-etching techniques. Low-stress SiN is used to preclude rupture of the stencil during the hole formation process. The membranes were coated by sputter deposition with an approximately 10-nm thick film of Si that acts as a charge dissipation layer during the electron beam lithography (EBL) and subsequent scanning electron microscopy (SEM) imaging steps. A Leica VB6 electron beam lithography tool is used to produce approximately 50-nm holes in a positive-tone, base-developable, chemically amplified resist (KRS-XE) at a dose of 30 $\mu C/cm^2$. The resist is

approximately 50-nm thick and serves as the etch mask in a subsequent reactive-ion etch process. A $CHF_3/CF_4/Ar$ plasma is used to etch the electron-beam generated pattern into the SiN membrane. The resist is removed after the SiN etch using an O_2 plasma. An SEM image of a SiN stencil directly after fabrication is shown in Figure 6.1b. The patterned holes in this particular stencil have a diameter of 56 ± 2 nm.

6.3.2 Stencil hole size reduction

In order to reduce the hole diameter to less than 50 nm, a thin layer of silicon dioxide is conformally deposited onto the stencils by low-pressure chemical vapor deposition (LPCVD). This process is shown schematically in Figure 6.1a. Before the stencils are loaded into the LPCVD furnace, they are cleaned successively by 300 W O_2 plasma (650 mTorr, 50 sccm), 120 ^oC piranha (98% H_2SO_4 + 30% H_2O_2) and finally rinsed in 18 $M\Omega \cdot cm^{-1}$ water. High temperature silicon dioxide is deposited by the reaction of N_2O (25 sccm) and SiH_2Cl_2 (75 sccm) in a 40 dm^3 quartz tube at 800 ^oC. The deposition rate is 0.45 nm/min and the step-coverage is 0.95. As shown below in Figure 6.1c, the inner sidewalls of the holes are covered uniformly by a thin layer of SiO_2 (the gray edge area in the high resolution SEM image in Figure 6.1c) and the hole diameter is evenly reduced to 36 nm from the original 56 nm. XPS (see Figure 6.3 spectrum I) detects no nitrogen signal, showing the top surface is fully covered by oxides as well.

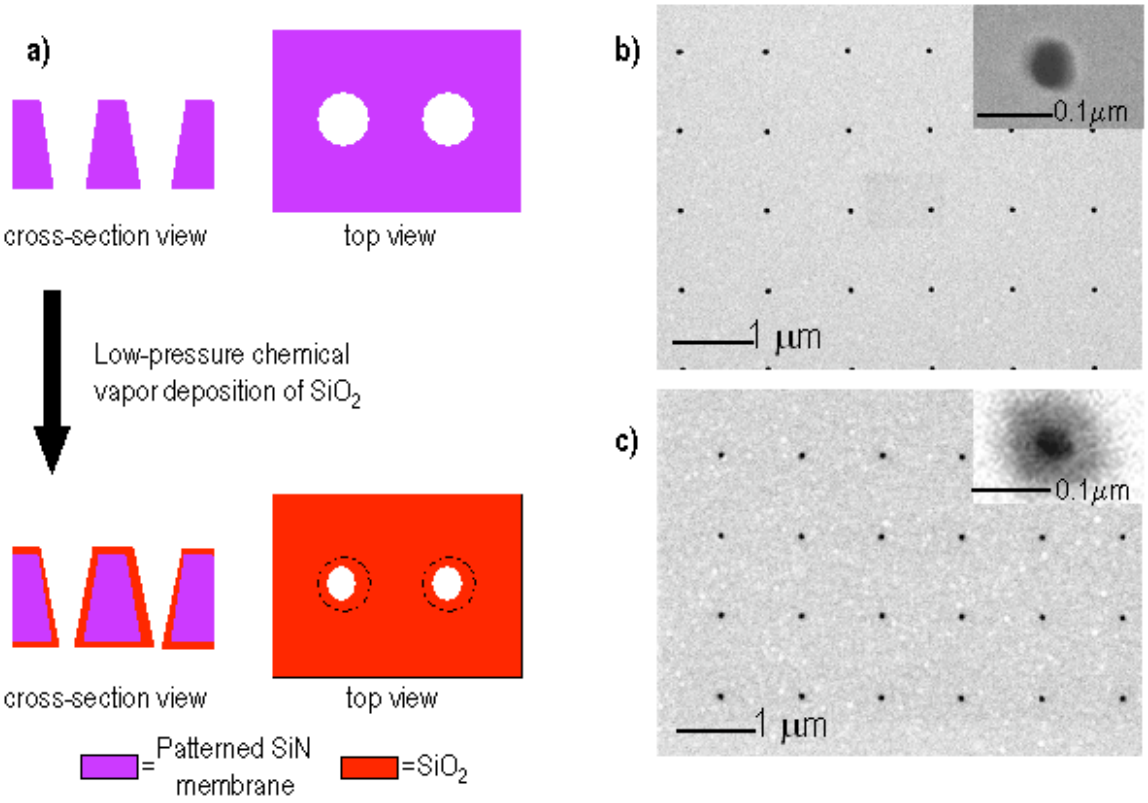

Figure 6.76: a) Schematic of stencil hole reduction. A LPCVD of SiO_2 is carried out coating the patterned holes in the SiN nanostencil, and reducing the hole diameter. b) SEM image of the SiN nanostencil with 56-nm hole diameter before LPCVD. c) SEM image of the SiN nanostencil with 36-nm hole diameter after LPCVD.

6.3.3 Surface functionalization of the stencil by a self-assembled monolayer

To avoid clogging while the stencils are being used[12], the surface of the reduced stencils is functionalized by tridecafluoro-1,1,2,2-tetrahydrooctyl-1-trichlorosilane (FTS) prior to use to form a fluorine terminated self-assembled monolayer (SAM). Note that the Si-O-H terminated surface enables the trichlorosilane group to react and form a covalently bound monolayer. The low surface energy FTS SAM helps to avoid the incident Pt metal from sticking to the stencil. This is shown schematically below in Figure 6.2. It also serves as a protective layer during stencil cleaning after the stencil has been used for a few Pt depositions. To form the SAM layer, the LPCVD-reduced stencil is placed into an oven filled with 2 mTorr FTS at 90 ^{o}C. A functionalized

surface is produced within 300 s. Finally the stencils were rinsed in acetone and n-hexane to remove any residual FTS. Water contact angles of the FTS covered stencil were larger than 105^{o}.

XPS data (Figure 6.3) shows that the FTS SAM protects the SiO_2-reduced SiN stencil effectively. The spectra from the top to the bottom are (I) LPCVD-reduced stencil, (II) FTS SAM functionalized stencil, (III) the stencil after three 16-nm Pt depositions, and (IV)the stencil from (III) cleaned by a Pt etchant (2:1:1 $HCl+H_2SO_4+H_3PO_4$ at 80 ^{o}C). Protection of the stencil with FTS clearly reveals the existence of F (spectrum II). Simultaneously one observes decreasing of the O and Si intensities due to the absence of O and Si on the surface after surface functionalization. The absence of Cl 2p signal around 200 eV indicates that the FTS on the surface exists primarily as a monolayer. The carbon has two peaks at 285 and 291 eV, corresponding to elemental and F-bonded carbon, respectively. A detailed XPS study of FTS SAM on Si has given elsewhere[13]. Following three depositions of 16-nm Pt each through the stencil, a Pt signal with minimal carbon is detected. The lack of O and Si signals is not surprising because some Pt is deposited on the inner sidewall of the holes also (see Figure 6.5h). Given that the inner sidewalls contribute only ~0.1% to the total surface area, no significant difference in the XPS spectra would be expected even if the inner sidewalls are exposed. Following cleaning of the Pt-covered stencil with a Pt etchant solution at 80 ^{o}C for 600 s, a small Pt peak is barely detected (< 0.02 monolayer) at 76 eV in Spectrum IV, suggesting the Pt has been removed effectively by the Pt etchant. Spectra II and IV are almost identical, showing that the FTS-SAM remains intact during the Pt removal.

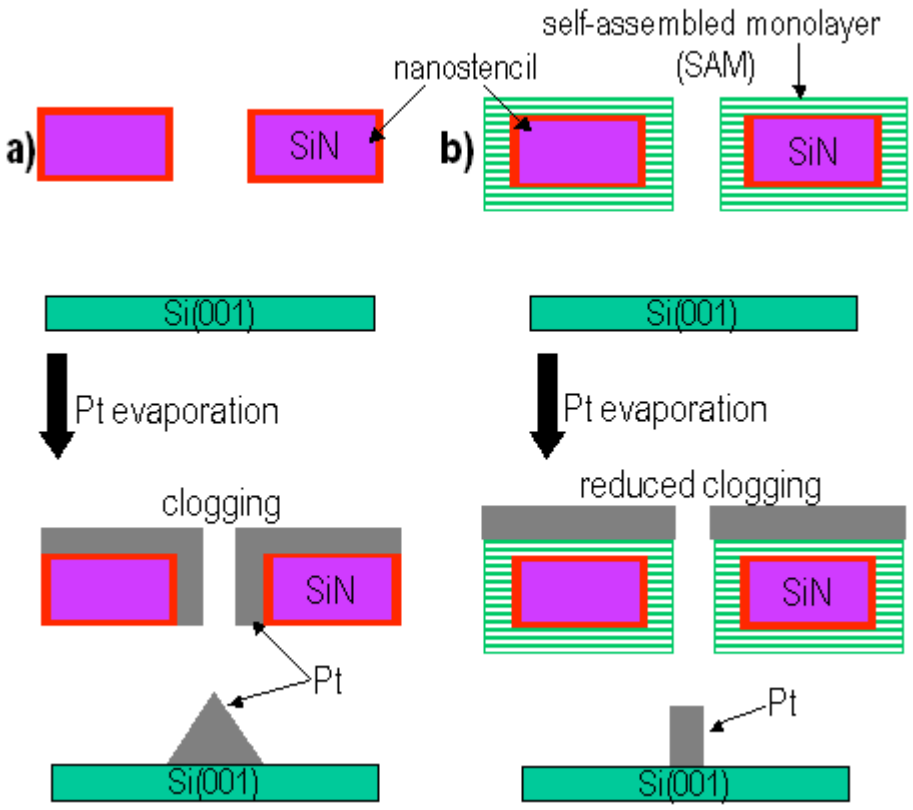

Figure 6.77: a) Gradual clogging of pattern in SiN nanostencil as Pt is deposited. b) When SAM of FTS is coated onto SiO2 surface, the surface energy is lowered, and there is reduced clogging of the nanostencil features by platinum.

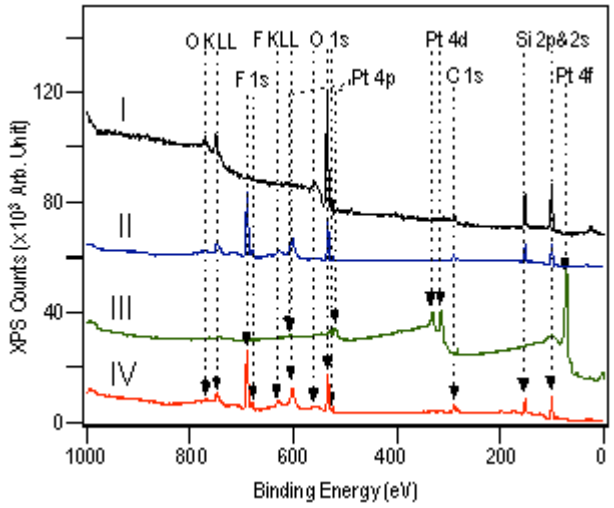

Figure 6.78: Stencil shrinking and cleaning characterized by X-ray photoelectron spectra (XPS). (I) After a thin layer of silicon dioxide is deposited onto the original silicon nitride stencil to reduce the stencil hole diameter (refer to Figure 6.1a and 6.1b). (II) The SiO_2-coated stencil is functionalized by a SAM of FTS. (III) After 48-nm Pt is deposited through the stencil in II. (IV) After the Pt is removed by the Pt etchant. The similarity between spectra II and IV shows clearly that the FTS SAM is inert to the Pt etchant.

6.4 Pt nanoparticle fabrication by e-beam deposition through patterned stencil

Pt is deposited on a native oxide covered Si(001) surface in an electron-beam evaporator. The evaporator has a base-pressure 1 x 10^{-6} Torr and a beam collimation of approximate 5 mrad. A quartz crystal oscillator monitors the thickness of the deposited films. All deposition rates are 0.1 nm/s. The sample holder is mounted on a water-cooled copper block. During deposition, the maximum substrate temperature is below 50 ^{o}C. E-beam deposition through the stencil onto the substrate gives rise to some problems. The stencil must be kept close to the substrate to avoid broadening but should be kept far enough away so as to avoid damaging the stencil upon removal. The separation between the stencil and the substrate is controlled to 0.1 μm by opening a 3-mm wide 0.1-μm deep trench in the substrate and placing the stencil into close contact with the substrate on the top of the trench (Figure 6.4). Under these conditions, the discrepancy between the stencil hole size and the deposited particle size should be smaller than 0.5 nm if there is no surface diffusion of the incident Pt atoms[14]. The 0.1-μm trench was created by first placing a 3-mm wide Si(001) strip on the substrate Si(001) surface with polished sides facing each other. Then, 0.1 μm of non-stoichiometric silicon oxide is deposited onto the substrate using e-beam evaporation, and finally the strip is removed leaving an area of the substrate not covered with the silicon oxide, thus creating a trench. The stencil was then mounted over the trench and 16 nm of Pt was deposited using the e-beam evaporator. The mounting of the stencil onto the substrate and the removal of the stencil after Pt deposition are carried out in a class-100 clean room in order to avoid dust particles compromising the gap between the stencil and substrate. After Pt deposition, both the

stencil and the resultant particles were characterized by SEM. SEM images are shown in Figures 6.5a-i.

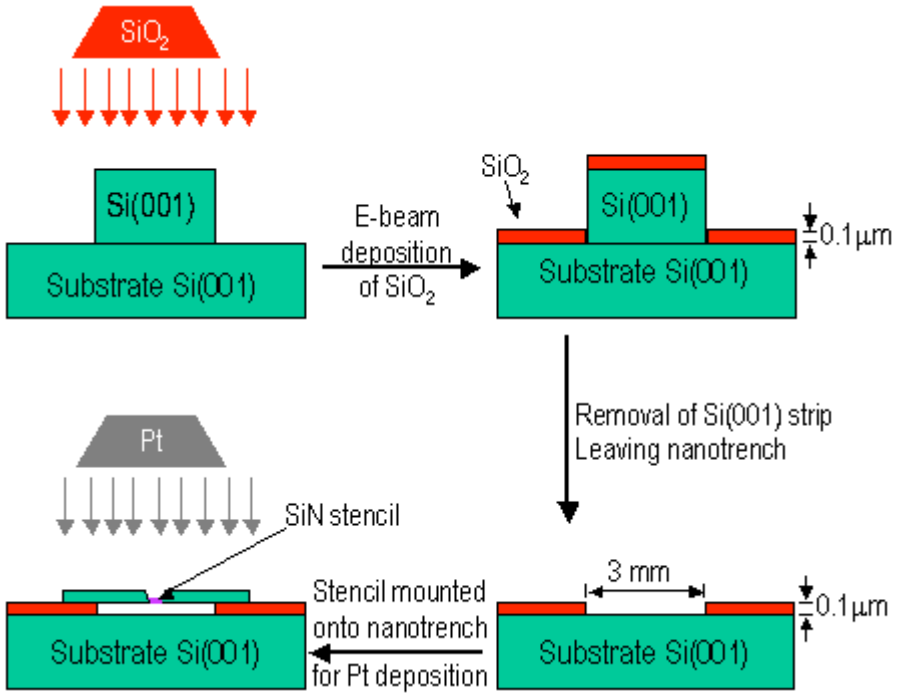

Figure 6.79: Schematic of trench formation for Pt deposition through SiN stencil.

6.4.1 Pt deposition through the original 56-nm stencil

Using the method described above, 16-nm thick Pt was deposited on a native oxide covered Si(001) surface through the original SiN stencil with 56-nm holes, leading to the formation of Pt nanoparticles on the substrate (Figure 6.5c). As expected, their pattern replicates that of the stencil. The particles have a diameter of 52 nm, which is 4-nm smaller than the original 56-nm diameter holes on the stencil. This may be due to additional collimation through the stencil holes. After 16 nm of Pt was deposited through the stencil, the average diameter of the holes on of the stencil is 46-nm—the holes are clogged significantly (Figure 6.5b). Close inspection of the area between the holes

reveals some textured features on the surface. They are the 3D Pt islands on the membrane.

6.4.2 Pt deposition through the LPCVD-reduced 36-nm stencil

16-nm Pt was deposited onto a native-oxide covered Si(001) wafer, through the stencil whose holes are reduced by SiO_2 LPCVD to a diameter of 36 nm (Figure 6.5d). The resultant Pt particles have a uniform size of 34 nm, and their pattern is identical to that of the original stencil (Figure 6.5f). After the deposition of 16-nm Pt, the hole diameter of this stencil is reduced to 33 nm (Figure 6.5e). The reduction (3 nm) is less than that on an original non-stoichiometric SiN stencil (10 nm) because of the weaker affinity between silicon dioxide and Pt comparing to Pt/SiN. In fact Pt thin film has been used as a glue layer between Au and Si_3N_4 to improve their adhesion[15]. Previous studies in our group have shown that Pt nanoparticles deposited at room temperature can be relocated by atomic force microscope (AFM) tip at a loading of 30 nN only on a fully oxidized surface[16].

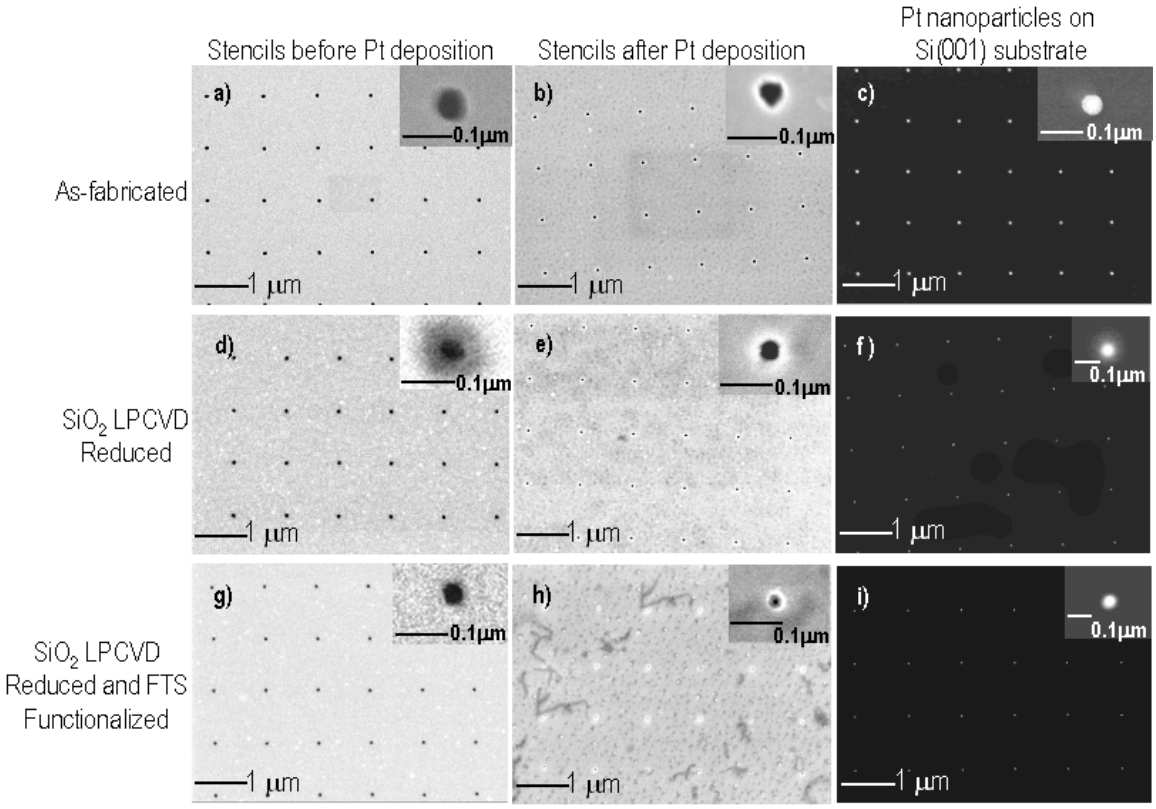

Figure 6.80: Scanning Electron Microscopy (SEM) images of SiN stencils and Pt nanoparticles on Si(001) with native oxide. (a) The original silicon nitride stencil as-fabricated by EBL. The hole size is 56 nm and the nearest center-center spacing is 1 μm. (b) After 16-nm Pt is deposited through the stencil in a. Clearly Pt (bright circle) is stuck on the sidewall of the stencil holes, and the holes are partially clogged, resulting in holes 46-nm in diameter. (c) Pt nanoparticles on Si(100) with native oxide. Particles deposited through stencil shown in a. Pt particles have diameter of 52 nm. (d) A thin layer of silicon dioxide is deposited on the original stencil conformally by LPCVD. The hole size is reduced to 36 nm and the nearest center-center spacing is 1 μm. (e) After 16-nm Pt is deposited through the treated stencil in d. The hole diameter is 33-nm after a single deposition. (f) Pt nanoparticles on Si(100) with native oxide. Particles deposited through stencil shown in d.

6.4.3 Multiple Pt depositions through the FTS-functionalized and LPCVD-reduced stencil

To demonstrate the potential for producing more complex structures, the substrate is moved laterally with respect to the stencil in between two consecutive depositions (Figure 6.6a). 16-nm of Pt is deposited by e-beam evaporation, in both of the depositions. The SEM images of the resultant Pt particles from single and double deposition are shown in Figures 6.5i (above) and 6.6b (below), respectively. The

particles from the first deposition have a uniform diameter of 35 nm (Figure 6.5i). It is very close to the measured stencil size, showing there is not much Pt sticking on the inner sidewall of the stencil, at least for the first 16-nm Pt deposition. The particles produced by the second deposition step during a double deposition have the same pattern as the first one, with the only difference that their lattice is offset by 318 and 85 nm in the X and Y directions, respectively, without noticeable rotation.

The stencil after three depositions of 16-nm Pt (total 48-nm) is shown in Figure 6.5h. Two noticeable changes have happened. One is that the stencil holes are clogged and their size is reduced to 10 nm, and the other is that there are many worm-like features spreading on the surface randomly. Comparing the high magnification SEM of the particles resulting from the first and second depositions (Figures 6.5i and 6.6b, respectively), the sizes of the particles are 35 ± 2 nm and 34 ± 3 nm, respectively. Evidently the clogging is just 1-2 nm at the most after the first 16-nm Pt is deposited, and the second and third depositions make the dominant contribution to hole clogging from 35 to 10 nm. The reason for this is most likely that after two depositions of platinum, there is a thin layer of platinum on top of the SiN membrane (Figure 6.2b). This thin film still has the patterned holes in it, but Pt deposits subsequent to this thin film formation will no longer be encountering the functionalized surface of the stencil, but a Pt thin film. So, the sticking probability will increase and will close the holes more quickly. Thus, the stencil has to be cleaned after a few depositions. We believe that the worm-like features result from the early stages of the stencil cracking. The cracking may be caused either by the high mass pressure of Pt, or mechanical vibration during both sample assembly/dissassembly and sample holder mounting/dismounting. Nevertheless, to

produce more complicated patterns using stencil deposition it is necessary to search for membranes with higher mechanical stability.

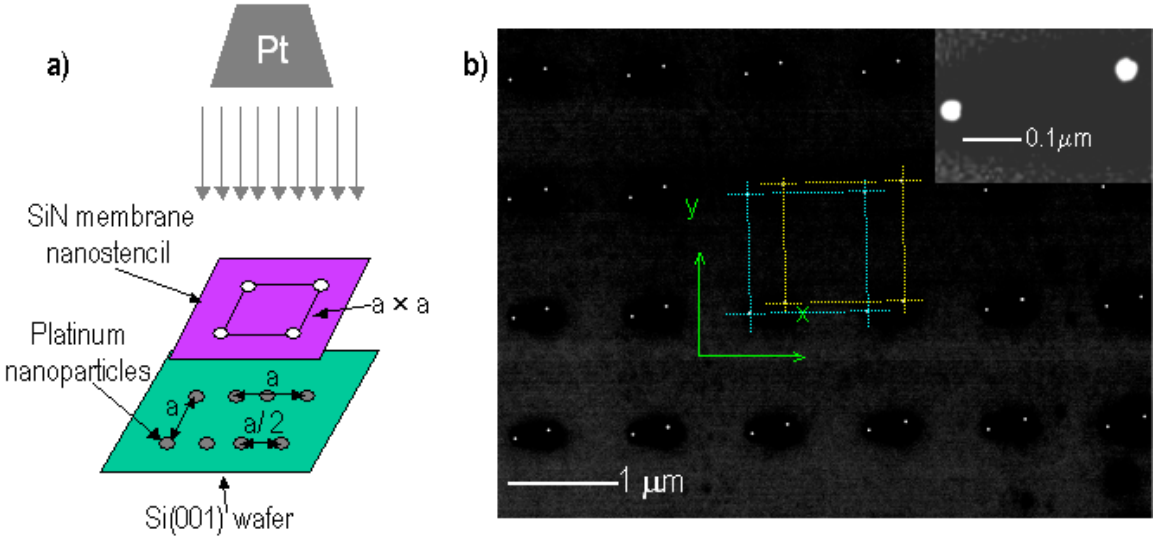

Figure 6.81: a) Schematic of stencil translation. In this picture, two Pt depositions are carried out. The first recreates the stencils features with spacing of a. Then the stencil is translated along the x axis by a/2 and another Pt deposition is carried out, which doubles the pattern density. b) SEM image of Pt nanoparticles after two sequential depositions through the LPCVD-reduced and FTS-functionalized stencil shown in Figure 6.5g. The first deposition gave Pt particles of 35-nm diameter. The stencil was then translated laterally 315 nm along the x-axis and 85 nm along the y-axis, and another Pt deposition was carried out. The second deposition gave particles of 34-nm diameter. The two sets of patterns are, highlighted by the golden (first deposition) and blue (second deposition) squares.

6.5 Summary

Using the conformal deposition of silicon dioxide, we have reduced the size of features in a silicon nitride stencil from 56 nm to 36 nm. Uniform sub-50 nm nanoparticles are fabricated by electron-beam evaporation of Pt through the patterned stencil. The particle pattern replicates that of the stencil. More complicated patterns can be generated by multiple depositions. A self-assembled monolayer of tridecafluoro-1,1,2,2-tetrahydrooctyl-1-trichlorosilane protects the stencil effectively during deposition and cleaning of Pt as monitored by XPS.

References

1. Saitou, N. *Int. J. Jpn. Soc. Prec. Eng*. **1996**, *30*, 107-111.
2. Matsui, S.; Ochiai, Y. *Nanotechnology* **1996**, *7*, 247-258.
3. Fay, B. *Microelectron. Eng.* **2002**, *11*, 61-62.
4. Itani, T.; Wakamiya, W.; Cashmore, J.; Gower, M. *Microelectron. Eng.* **2003,** *67-68*, 39-46.
5. van den Boogaart, M.A.F.; Kim, GM; Pellens, R; van den Heuvel, J.-P.; Brugger, J. *J. Vac. Sci. Technol. B*. **2004,** *22*, 3174-3177.
6. Grunes, J.; Zhu, J.; Yang, M.C.; Somorjai, G.A. *Catal. Lett.* **2003,** *86*, 157-161.
7. Contreras, A.M.; Grunes, J.; Yan, X.-M.; Liddle, A.; Somorjai, G.A. *Catal. Lett.* **2005,** *100*, 115-124.
8. Melngailis, J.; Mondelli, A.A.; Berry III, I.L.; Mohondro, R. *J. Vac. Sci. Technol. B*, **1998,** *16*, 927-957.
9. Ruchhoeft, P.; Wolfe, J.C.; Bass, R. *J. Vac. Sci. Technol. B* **2002,** *20*, 87-89.
10. Egger, S.; Ilie, A.; Fu, Y.T.; Chongsathien, J.; Kang, D.-J.; Welland, M.E. *Nano Lett.* **2005,** *5*, 15-20.
11. Lee, S.; Shim, Y.S.; Cho, H.Y.; Kang, T.W.; Kim, D.Y.; Lee, Y.H.; Wang, K.L. *Thin Solid Films* **2004,** *451-2*, 379-383.
12. Kolbel, M.; Tjerkstra, R.W.; Kim, G.; Brugger, J.; van Rijn, C.J.M.; Nijdam, W.; Huskens, J.; Reinhoudt, D.N. *Adv. Funct. Mat.* **2003,** *13*, 219-224.
13. Lagutchev, A.S.; Song, K.J.; Huang, J.Y.; Yang, P.K.; Chuang, T.J. *Chem. Phys.* **1998,** *226*, 337-349.
14. Ruchhoeft, P.; Wolfe, J.C.; Bass, R.; *J. Vac. Sci. Technol.* B **2001,** *19*, 2529-2532.

15. Aristov, V.V.; Kazmiruk, V.V.; Kudryashov, V.A.; Levashov, V.I.; Red'kin, S.I.; Hagen, C.W.; Kruit, P. *Surf. Sci.* **1998,** *404*, 337-340.

16. Tsirlin, T.; Zhu, J; Grunes, J.; Somorjai, G.A. *Top. Catal.* **2002,** 19, 165-170.

Chapter 7

Conclusions and Future Work in Two-Dimensional Model Catalysis

The two-dimensional lithographically fabricated catalysts described in this dissertation offer a unique laboratory method of studying different catalytic reactions. With the precise control over several different system parameters (structure height, spacing and width) afforded by these fabrication techniques, the catalyst can be changed systematically to see how this change affects reaction rates and selectivity. As well, this control allows for further analysis of results, such as the oxide-metal interface argument made in Chapter 3. Eppler *et. al.* have already demonstrated the enhanced selectivity that this type of system can have on multi-path reactions such as cyclohexene hydrogenation/dehydrogenation[1]. The improved knowledge of the catalyst surface, that nanofabrication methods continue to bring, is the key to improving catalyst efficiency and selectivity in the future.

Recent advancements in solution synthesis of platinum and rhodium nanoparticles bring promise to this area[2,3]. Coupled with Langmuir-Shaeffer (L-S) techniques, high density arrays of two-dimensional noble metal nanoparticles can be deposited on planar oxide single crystals or oxide-coated silicon wafers. With the tighter size and shape distributions made possible by the advent of nanoscience and the tight spatial distributions possible using L-S techniques, it has now become possible to fabricate two-dimensional model catalysts with virtually single-crystalline particles in a regularly spaced pattern on a well-ordered oxide thin film or single-crystalline oxide support[2]. With the increased surface area, lower turnover reactions can be studied, and the system parameters are still tunable on the nanometer scale.

Use of the nanostencil idea put forth in Chapter 6 offers another method of gaining this increased system control. With control over the surface structure of the oxide support used for a substrate, the metal film deposited will be more controlled as well. The spacing between the metal particles can be controlled by translation of the stencil on the nanometer scale with a piezoelectric actuator[4]. The size-reduction of the nanostencil features coupled with this precise translation capability allows this system to be used for extremely precise measurements of the spacing effects of nanoarrays on catalysis. However, since these SiN membranes are patterned originally by use of EBL, the production of these particles on a large enough scale to study low turnover catalytic reactions is still a problem.

Nanoimprint lithography with the Si nanowire molds discussed in Chapters 4 and 5 can also be used to make nanoparticles, but on a larger scale than by either EBL (chapter 3) or deposition through a SiN membrane (Chapter 6). A novel mold-to-mold

cross imprint method has been developed that is capable of creating a second mold of silicon nanopillars[5]. If NIL is used with this secondary mold, nanoparticle arrays can be made on planar supports on a scale large enough to enable facile measurements of both high and low turnover reactions.

Lithographically fabricated model catalysts offer many opportunities for surface science and catalysis studies, and further advances in nanotechnology are already opening the door to future work in this area.

References

1. H. Song, F. Kim, S. Connor, G.A. Somorjai, P. Yang, *J. Phys. Chem. B*, 109, **2005**, 188.
2. J.D. Hoefelmeyer, K. Niesz, G.A. Somorjai, T.D. Tilley, *Nano Lett.*, 5, **2005**, 435.
3. A.S. Eppler, J. Zhu, E.A. Anderson, G.A. Somorjai, *Top. Catal.,* 13, **2000**, 33.
4. S. Egger, A. Llie, Y. Fu, J. Chongsathien, D.-J. Kang, M.E. Welland, *Nano Lett.*, 5, **2005**, 15.
5. S. Kwon, X.-M. Yan, A.M. Contreras, J.A. Liddle, G.A. Somorjai, J. Bokor, *Nano Lett.*, 5, **2005**, 2557.